

M.Sc. Xiao Li
Wuppertal

**Investigation of
Cohesive Zone Models
for Three-Dimensional
Fatigue Crack
Propagation in
Engineering Metals**



Cuvillier Verlag Göttingen
Internationaler wissenschaftlicher Fachverlag



Investigation of Cohesive Zone Models for Three-Dimensional Fatigue Crack Propagation in Engineering Metals





Investigation of Cohesive Zone Models for Three-Dimensional Fatigue Crack Propagation in Engineering Metals

Von der Abteilung Maschinenbau der Bergischen Universität Wuppertal
zur Erlangung der Würde eines Doktors der
Ingenieurwissenschaften (Dr.-Ing.) genehmigte Abhandlung

Vorgelegt von
M.Sc. Xiao Li



Hauptberichter:	Univ.-Prof. Dr.-Ing. Huang Yuan
Mitberichter:	Univ.-Prof. Dr.-Ing. Karl-Heinz Schwalbe
Mitberichter:	Univ.-Prof. Dr.-Ing. Peter Gust
Tag der Einreichung:	24. Oktober 2016
Tag der mündlichen Prüfung:	21. Dezember 2016

BERGISCHE UNIVERSITÄT WUPPERTAL

2016.



Bibliografische Information der Deutschen Nationalbibliothek

Die Deutsche Nationalbibliothek verzeichnet diese Publikation in der Deutschen Nationalbibliografie; detaillierte bibliografische Daten sind im Internet über

<http://dnb.d-nb.de> abrufbar.

1. Aufl. - Göttingen: Cuvillier, 2017

Zugl.: Wuppertal, Univ., Diss., 2016

© CUVILLIER VERLAG, Göttingen 2017

Nonnenstieg 8, 37075 Göttingen

Telefon: 0551-54724-0

Telefax: 0551-54724-21

www.cuvillier.de

Alle Rechte vorbehalten. Ohne ausdrückliche Genehmigung des Verlages ist es nicht gestattet, das Buch oder Teile daraus auf fotomechanischem Weg (Fotokopie, Mikrokopie) zu vervielfältigen.

1. Auflage, 2017

Gedruckt auf umweltfreundlichem, säurefreiem Papier aus nachhaltiger Forstwirtschaft

ISBN 978-3-7369-9619-9

eISBN 978-3-7369-8619-0



To my parents and my wife for their love and support.





Preface

The present work was accomplished during my work at Bergische Universität Wuppertal as the scientific assistant at Chair of Technical Mechanics from 2010 to 2015. At the accomplishment of the thesis, I would like to express my sincere gratitude to all people who have given me help and supported me during the composition of my thesis.

I deeply acknowledge my academic advisor, Prof. Dr.-Ing. Huang Yuan. This work would have been impossible without his guidance, valuable support and warm encouragement. His consistent and illuminating suggestions constitute an indispensable part of this work. I am so lucky to be one of his students. When I got problems in my research and in writing, the door of Prof. Yuan's office would be always open. Moreover, I deeply appreciate that Prof. Yuan guided me not only so much professional knowledge but also the wisdom of life. That is/will be the wealth for my further work.

My special thanks go to Prof. Dr.-Ing. Karl-Heinz Schwalbe and Prof. Dr.-Ing. Peter Gust for serving as the thesis reviewer and giving kind advice and fruitful help to my work.

I would like to thank Prof. Dr.-Ing. Uwe Janoske for his efforts in organizing the examination committee and being the chairman. I am also thankful to Prof. Dr.-Ing. Hans-Bernhard Woyand for serving on my examination committee.

The present thesis was financial supported by the German Science Foundation (DFG). I am grateful to the DFG for the support.

I also wish to thank to Prof. Dr.-Ing. Kai-Dietrich Wolf, Prof. Dr.-Ing. Udo Siegfried Pietzsch, Prof. Dr.-Ing. Reinhard Harte, Dr.-Ing. Cagna Michele, Dr. Holger Arndt, Dipl.-Ing. Henry Pusch, Mrs. Angelika Dülligen, Mrs. Sabine Kranz and Late Mrs. Magdalene Blucha for their help during my study at Bergische Universität Wuppertal.

For the pleasant atmosphere and their help, I wish to express my acknowledgement to the members of Chair of Technical Mechanics at Bergische Universität Wuppertal, specially Heiko Krull, Dr. Xiaofei Pan, Dr.-Ing. Yangjian Xu, Dr.-Ing. Jingxiang Liu, Dr.-Ing. Markus Schneider, Dr.-Ing. Songyun Ma, Dr.-Ing. Huan Li, Dr.-Ing. Jie Fang, Ravindra Ambati, Zhongzhuan Yao, and Jingyu Sun. Thanks a lot for friendship and helpful suggestions.

Finally, I would like to thank my parents and my wife for their boundless love and whole-hearted support during these years. Words fail to express my appreciation.

Wuppertal, in Oktober 2016

Xiao Li





Contents

Abstract	III
Zusammenfassung	IV
Nomenclature	VI
1 Introduction	1
1.1 Background	1
1.2 Cohesive zone model	4
1.3 Cyclic cohesive zone model	9
1.4 Outline of the dissertation	10
2 Effects of the cohesive law for ductile crack simulation	12
2.1 Introduction	12
2.2 Formulation of the cohesive element with a threshold traction	14
2.3 Effects of the cohesive stiffness	17
2.4 Energy balance in crack propagation with a cohesive zone	21
2.5 Summary	25
3 Experimental investigation on fatigue cracks	26
3.1 Introduction	26
3.2 Material and C(T) loading tests	27
3.3 Surface fatigue crack tests under cyclic axial loading	31
3.4 Fatigue crack propagation of C(T) specimens with different thicknesses	40
3.5 Cohesive law identification based on special CTS specimens	46
3.6 Summary	52
4 Stress-triaxiality-dependent cohesive zone model	54
4.1 Introduction	54
4.2 Stress-triaxiality-dependent cohesive zone model	56
4.3 Identification of the cohesive parameters	57
4.4 Computations and Discussions	63
4.5 Summary	69
5 A uniform CZM for both fatigue and fracture crack simulation	70
5.1 Introduction	70
5.2 A new cyclic cohesive zone model	73
5.3 Validation of the cyclic cohesive zone model	77
5.4 Verification based on fatigue experiments	84
5.5 Summary	87



6	Stress-triaxiality-dependent cyclic cohesive zone model	88
6.1	Introduction	88
6.2	Stress-triaxiality-dependent cyclic cohesive zone model	89
6.3	Model verification	92
6.4	Summary	106
7	Conclusions and outlook	108
7.1	Conclusions	108
7.2	Outlook	109
	Bibliography	110

Abstract

Modeling and prediction of the mechanical part failure under cyclic loading conditions are of great importance. With the development of technology, damage tolerance design becomes compulsory and fatigue crack propagation life is a necessary design case, e.g. in aerospace industry. For elastic-plastic fatigue crack propagation the failure process is generally ductile, material failure is accompanied with a large amount of elastic unloading and plastic reloading, which cannot be described by the known Paris' law. In the ductile metallic material, this problem becomes especially significant for fatigue crack propagation in low cycle fatigue (LCF) assessment.

In past decades, the cohesive zone model (CZM) has been popular in computational fracture mechanics community. Material behavior in the cohesive zone is described by a cohesive law. Parameter studies on the effects of the cohesive law on ductile crack simulation show that to obtain realistic crack propagation, one has to further increase the stiffness of the cohesive zone. The fracture energy release rate in crack simulation using CZM differs from the cohesive energy.

The investigation of constraint effects has confirmed that cracking depends on the applied load intensity and the load configuration. Computational modeling of three-dimensional ductile crack propagation under significant constraint effects is still a challenge in computational fracture mechanics. In the present work, a new stress-triaxiality-dependent cohesive zone model (TCZM) is proposed to describe the elastic-plastic fracture process. Both cohesive energy and cohesive strength are assumed to be dependent on the stress triaxiality and the correlations are identified according to the experiments. Three-dimensional computational predictions show good agreement with experimental results. The model gives a realistic elastic-plastic fracture process.

In fatigue crack growth simulation, cyclic cohesive zone models (CCZM) are investigated extensively, which accounts for the damage evolution under cyclic loading and, thus, can predict fatigue crack growth. Numerous proposed CCZMs can only describe the Paris' law like behavior. To achieve a more realistic damage evolution, a new damage variable is proposed which can be decomposed into monotonic damage and cyclic damage. The parameters in the cohesive zone model are identified from the fatigue tests of the cracked specimens. Computations confirm that the present model may provide a uniform description for the whole fatigue crack growth regimes.

By considering the influence of the stress-state effect on the proposed CCZM, a new stress-triaxiality-dependent cyclic cohesive zone model (TCCZM) is developed. The stress triaxiality affects both the cohesive law and the damage evolution equation. Three-dimensional fatigue crack predictions are performed in the C(T) specimen and the cracked rod bar. Numerical results indicate that TCCZM can predict the three-dimensional fatigue crack appropriately. However, the limitations of present models are due to the only consideration of the normal failure, the predictions show deviation in the area of the dominance of mode III failure. Present study confirms the applicability of the stress-triaxiality-dependent cohesive zone model to fatigue crack prediction as a general extended model.

Zusammenfassung

Die Modellierung und Vorhersage des Bauteilversagens unter zyklischen Lastbedingungen ist von großer Bedeutung. Bei der Entwicklung von Technologien ist die Bewertung der Beschädigungstoleranz (Damage tolerance assessment) obligatorisch. Ebenso ist die Einschätzung der Lebensdauer im Hinblick auf eine Rissausbreitung durch Ermüdung ein notwendiger Aspekt der Konstruktion, z. B. in der Luftfahrtbranche. Für die elastisch-plastische Ermüdungsrissausbreitung ist der Schädigungsprozess im Allgemeinen duktil. Das Materialversagen wird von einer großen Menge an elastischer Entlastung und plastischer Belastung begleitet, was durch das Pariser Gesetz nicht beschrieben werden kann. Besonders bei duktilem metallischem Material stellt die Ermüdungsrissausbreitung bei der elastisch-plastischen Ermüdungsanalyse (LCF) eine besondere Herausforderung dar.

In den vergangenen Jahrzehnten war das Kohäsivzonenmodell (CZM) in der numerischen Bruchmechanik populär. Das Materialverhalten in der kohäsiven Zone wird durch ein Kohäsivgesetz beschrieben. Parameterstudien über die Auswirkungen des Kohäsivgesetzes auf die duktile Rissimulation zeigen, dass um eine reale Rissausbreitung zu erhalten die Steifigkeit der Kohäsionszone weiter erhöht werden muss. Die Bruchenergie, die bei der Rissimulation mithilfe von CZM ermittelt wurde, unterscheidet sich von der Kohäsionsenergie.

Die Untersuchung von Einschränkungseffekten hat bestätigt, dass das Rissbild von der angewandten Lastintensität und der Lastkonfiguration abhängt. Die rechnerische Modellierung der dreidimensionalen duktilen Rissausbreitung unter signifikanten Einschränkungseffekten stellt in der numerischen Bruchmechanik nach wie vor eine Herausforderung dar. In der vorliegenden Arbeit wird ein neues spannungsdreiachsigen Kohäsivzonenmodell (TCZM) vorgeschlagen, um den elastisch-plastischen Bruchprozess zu beschreiben. Sowohl die Kohäsivenergie als auch die Kohäsivkraft werden von der Spannungsdreiachsigen abhängig gemacht und die Korrelationen werden anhand der Experimente identifiziert. Dreidimensionale Berechnungsvorhersagen zeigen eine gute Übereinstimmung mit experimentellen Ergebnissen des elastisch-plastischen Bruchprozesses.

In der Ausbreitungssimulation von Ermüdungsrissen werden zyklische Kohäsivzonenmodelle (CCZM) intensiv untersucht, was die Schadensentwicklung unter zyklischer Belastung berücksichtigt und somit das Ermüdungsrissausbreitung vorhersagen kann. Zahlreiche vorgeschlagene CCZMs können nur das Verhalten nach dem Pariser Gesetz beschreiben. Um eine realistischere Schadensentwicklung zu erreichen, wird eine neue Schadensvariable vorgeschlagen, die in monotone Schäden und zyklische Schäden unterteilt wird. Die Parameter im Kohäsivzonenmodell werden aus den Ermüdungstests der angerissenen Proben identifiziert. Berechnungen bestätigen, dass das vorliegende Modell eine einheitliche Beschreibung für das gesamte Ermüdungsrisswachstumsregime liefern kann.

Unter Berücksichtigung des Einflusses des Spannungszustandes auf das vorgeschlagene CCZM wird ein neues spannungsdreiachsigen zyklisches Kohäsivzonenmodell (TCCZM) entwickelt. Die Spannungsdreiachsigen beeinflusst sowohl das Kohäsivgesetz



als auch die Schadensentwicklungsgleichung. Dreidimensionale Ermüdungsrissvorhersagen werden in der C(T)-Probe und dem gerissenen Stab durchgeführt. Numerische Ergebnisse zeigen, dass das TCCZM den dreidimensionalen Ermüdungsriss in geeigneter Weise vorher-sagen kann. Allerdings ist das entwickelte Modell nur für das Normalversagen begrenzt. Die Vorhersagen zeigen eine Abweichung im Bereich mit der Modus-III-Dominanz. Die vorliegende Studie bestätigt die Anwendbarkeit des spannungsdreiachsigen Kohäsivmodells zur Ermüdungsrissvorhersage als ein allgemeines erweitertes Modell.

Nomenclature

Symbols of CZM

T	traction tensor
δ	separation tensor
T_0	cohesive strength
δ_0	critical separation (the separation when the traction reaches the maximum)
δ_u	ultimate separation (the separation when the traction vanishes)
Γ_0	cohesive energy
$T_{\max}(\eta)$	stress-triaxiality-dependent cohesive strength
$\Gamma(\eta)$	stress-triaxiality-dependent cohesive energy
$\delta_u(\eta)$	stress-triaxiality-dependent ultimate separation
D	Damage variable
D_m	monotonic damage
D_c	cyclic damage
$D_m(\eta)$	stress-triaxiality-dependent monotonic damage
$D_c(\eta)$	stress-triaxiality-dependent cyclic damage
T_{0_cyc}	the current cohesive strength, $T_{0_cyc} = T_0(1 - D)$
d_Σ	accumulative length
n	damage controlling parameter

δ_{acc}	separation accumulation
k	un/reloading stiffness
$k(\eta)$	stress-triaxiality-dependent un/reloading stiffness
ζ	characteristic length of the cohesive zone

Symbols of Mechanics

σ	stress tensor
ε	strain tensor
E	Young's modulus of the bulk material
ν	Poisson's ratio
σ_y	initial yield stress
σ_u	ultimate stress
ε_f	elongation
n	strain hardening exponent
r_p	plastic zone size
G	energy release rate
K	stress intensity factor
K_c	fracture toughness
K_{th}	threshold stress intensity
R	loading ratio
ΔK	stress intensity range
ΔF	cyclic loading range
σ_a	stress amplitude
σ_m	mean stress



C	constant parameter in Paris' law
m	constant parameter in Paris' law
σ_{22}	tensile stress
Ψ	material stiffness
J	J-integral
J_i	J-integral at crack initiation
J_m	average J-integral
η	stress triaxiality
η_m	average stress triaxiality
a	crack length at the middle plane
Δa	crack extension at the middle plane
s	crack length at the free surface
Δs	crack extension at the free surface
v_{LL}	load line displacement
δ_5	CTOD defined by Schwalbe
N	loading cycles
\mathbf{u}	displacement tensor
B	specimen thickness
B_N	specimen net thickness
W	specimen width
D	specimen diameter
da/dN	fatigue crack growth rate
l_e	finite element length

Abbreviations

LEFM	linear elastic fracture mechanics
EPFM	elastoplastic fracture mechanics
LCF	low cycle fatigue
CZM	cohesive zone model
CCZM	cyclic cohesive zone model
TCZM	stress-triaxiality-dependent cohesive zone model
TCCZM	stress-triaxiality-dependent cyclic cohesive zone model
GTN	Gurson-Tvergaard-Needlman model
C(T)	compact tension specimen
CTS	compact tension shear specimen
CTOD	crack tip opening displacement
UEL	user subroutine to define an element in ABAQUS
UMAT	user subroutine to define a material behavior in ABAQUS



1 Introduction

1.1 Background

Fracture accidents are serious problems that human society has faced for a long time. Generally speaking, all components contain certain kinds of defects and micro-cracks, regardless of manufacturing and machining processes. A stress engineer confronts with an important question which kinds of defects, which size of defects, which loads and which environmental influence will affect the life of the designed components. Fracture mechanics is used to evaluate the strength of a structure or component in the presence of a crack or flaw. Development of fracture mechanics is helpful to eliminate some of the potential dangers due to increasing components complexity.

1.1.1 Fundamental of fracture mechanics

The typical process of solving fracture mechanics problem is to evaluate characteristic parameters of crack based on fracture criteria. The critical values of the characteristic parameters will be experimentally determined as a function of the crack length, specimen geometry and loading configurations.

The first successful analysis of a fracture problem was laid in 1920 by Griffith [1], who considered the propagation of brittle cracks in glass. He showed that the product of the far field stress, the square root of the crack length, and material properties governed crack extension. This product was shown to be related to the energy release rate, G , which represents the elastic energy per unit crack surface area required for crack extension.

Irwin [2, 3] later made significant advances by showing that the energy approach is equivalent to the stress intensity factor K . The fracture occurs when a critical stress distribution ahead of the crack tip is reached. The material property governing fracture may therefore be stated as a critical stress intensity, K_c , or in terms of energy as a critical value G_c . Demonstration of the equivalence of G and K provided the basis for development of the discipline of linear elastic fracture mechanics (LEFM).

Since no material could carry the infinite stresses derived by the elasticity assumption, a plastification extending from the crack tip must take place. The plastic deformations will cause stress redistribution and the elastic solution will be no longer valid for the whole inelastic zone. The concept of elastoplastic fracture mechanics (EPFM) is developed.

Under assumption of an elastic-perfectly plastic material, Irwin [4] presented a simplified model for determination of the plastic zone attending the crack tip under small-scale yielding (SSY). He argued that the plasticity at the crack tip causes the crack to behave as if it were longer than its true physical size. It means that the plastification reduce the structure carrying capacity. A cracked specimen with a plastic zone size r_p corresponds to a specimen with crack length $a_{\text{eff}} = a + r_p$. Correspondingly, the effective stress intensity factor K_{eff} is evaluated.

Wells [5] proposed a fracture criteria related to the displacement between crack surfaces which separate associated with plastic deformation. The separation distance led to the development of a new parameter which is known as crack tip opening displacement (CTOD). A standardized method firstly developed by Schwalbe [6] measures the CTOD on the specimen surface at the fatigue precrack tip over an original gauge length of 5 mm (δ_5).

In 1968, Rice [7] introduced an elastic-plastic fracture parameter to characterize nonlinear material behavior of crack tip, J -integral. It is the generalization of the energy release rate for nonlinear elastic materials. For stationary crack problems, if the remote applied load is only assumed monotonic, the J -integral is path-independent. It was firstly proposed as a fracture parameter by Begley and Landes [8].

Hutchinson [9], Rosengren and Rice [10] used J as a single parameter to characterize crack tip stress fields under SSY condition in nonlinear materials (HRR solution). Shih [11] demonstrated a correlation between J -integral and CTOD, implying that both parameters are equally valid for characterizing fracture.

The J -integral and the HRR solution provide the basis to consider the crack-tip field of the nonlinear fracture problems, however, the limitation arises due to high constraint crack geometries.

1.1.2 Constraint effect in ductile fracture

It has been known that the resistance against initiation of ductile crack growth and crack propagation depends on the geometry and the load configuration of the respective specimen of structural component [12–20]. The geometry dependence of the crack growth resistance in ductile materials arises due to the competition between two dissipations, i.e. the plastic deformation around the crack tip and the energy spent in the actual creation of new surface due to microseparation processes [13, 21]. The J -integral is insufficient to characterize a crack, even in a two-dimensional specimen.

In order to account for different triaxial stress-states in influencing crack tip fields, O’Dowd and Shih [22, 23] proposed the two-parameter J - Q theory. In this case, Q represents the constraint at the crack tip.

Yuan and Brocks [18] considered the plastic zone size in three-dimensional cracked specimens. The computations confirm that the out-of-plane constraint is not directly related with the in-plane constraint, which is mainly a manifest of the loading configuration to the crack tip field. This knowledge implies that the computational crack model has to include more details about the crack field besides the stress intensity, such as K and J et al. The constraint around the crack tip has to be represented in a more suitable way.

In characterization of three-dimensional cracks Brocks and Künecke [24] found the stress triaxiaity is a meaningful crack parameter besides the J -integral, defined as the ratio of hydrostatic stress over the effective stress, $\eta = \sigma_h/\sigma_e$. In fact η is directly related to crack field, while Q evaluate the difference between the real crack stresses and the plane strain reference crack field.

The constraint effects make the crack assessment methodology based on the conventional crack parameters too complex to apply for engineering. The transferability problem, which means transferring the crack growth resistance data as measured on laboratory specimens to assessing the defects in components, is a real practical concern.

1.1.3 Fatigue crack growth

The strength of a component or structure can be significantly reduced by the presence of a crack or discontinuity. However, in most engineering cases, the initial crack or discontinuity size is not critical to cause catastrophic failure. More commonly, subcritical crack growth occurs from the existing crack or discontinuity until a critical crack size is reached, causing fracture. Then, the major question would be how fast the crack grows from an initial length to the critical crack size.

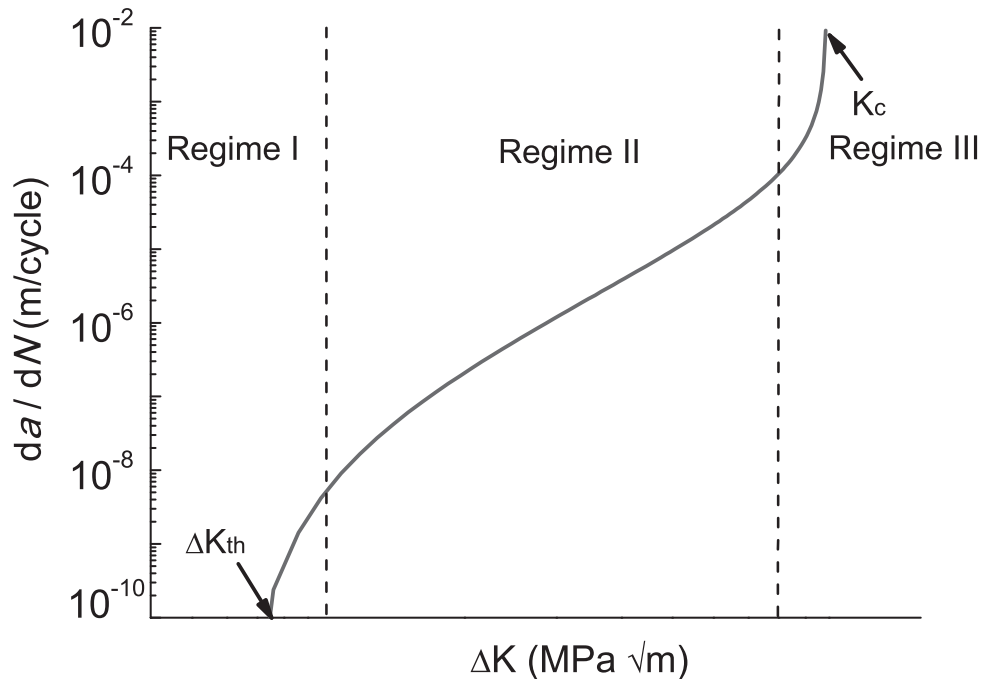


Figure 1.1: Schematic demonstration of fatigue crack growth rate versus ΔK .

Applying the concepts LEFM or EPFM under SSY condition, the stress intensity factor K can characterize the stress field around the crack tip involving the applied stress, crack size and the material geometry. Paris and Erdogan [25] firstly suggested that for a cyclic variation of the imposed stress field, the rate of fatigue crack growth (da/dN) should be based on the stress intensity factor range (ΔK). The well-known Paris equation can be denoted as

$$\frac{da}{dN} = C(\Delta K)^m, \quad (1.1)$$

where C and m are material specific parameters. Many fatigue crack growth data can be obtained under constant load amplitude test condition using sharp cracked specimens. The typical log-log plot of da/dN vs. ΔK shown schematically in Fig. 1.1 has a sigmoidal shape that can be divided into three major regions. Region I is the near threshold (ΔK_{th}) region which indicates the early development of a fatigue crack and the crack growth rate. The threshold value is on the order $10^{-10} \sim 10^{-9}$ m/cycle. Fatigue crack should not propagate below the threshold value. Region II represents a stable crack propagation zone under small-scale yielding condition. The data follows a linear relation between $\log(da/dN)$ and

$\log(\Delta K)$ which corresponds to Paris equation. Region III shows a very high crack growth rate which is near the final failure. Unstable crack growth would occur when approaches the fracture toughness K_c , which in turn depends on the microstructure, the mean stress and the environment.

Forman et al. [26] improved Paris' law by suggesting a new model which is capable of describing Regime III of the fatigue crack growth curve and including the stress ratio effect. Further modifications of the Forman's expression by Erdogan and Ratwani [27] to represent region I, II and III have been accomplished by including the threshold stress intensity parameter ΔK_{th} .

Based on the experimental observations, a fatigue crack can close at a remotely applied tensile stress due to a zone of compressive residual stresses left in the crack tip. Therefore, many closure models were proposed based on the effective stress intensity factor range ΔK_{eff} . Elber [28, 29] introduced the crack closure concept to analyze crack propagation under variable amplitude loading. Newman [30, 31] used a crack closure approach for predicting the fatigue crack growth life. The crack opening stress, σ_{op} , as a function of crack length and load history was calculated by an iterative solution procedure for a cycle-by-cycle closure calculation using detailed FE programs. Although the estimation of plastic zone size suggested by Irwin is very elementary, the engineering application confirms a high accuracy of this method.

Despite the use of K -based models have been an enormously successful engineering theory, it is important to recall that most engineering estimates of fatigue crack growth rely on K under the assumption that the plastic behavior of the material around the crack tip will not affect the crack growth process. However, for low cycle fatigue problems, the material is locally plastic, especially around cracks. Due to a large amount of plastic zone, fatigue crack propagation is very complex and conventional K -based models cannot describe the crack propagation behavior appropriately. Predicting elastoplastic fatigue crack growth life remains one of the most challenging problems in fracture mechanics.

1.2 Cohesive zone model

1.2.1 Numerical damage models

The advent of numerical damage models is providing an approach to structural assessment in that these models deal with the damage events in the near-crack tip process zone which are embedded in the global FE model of the component. This way the global FE model prescribes the loading conditions and the component is under onto the damage zone [32].

Analytical and macroscopic approaches used in fracture mechanics have some limitations with respect to the amount of plasticity allowed at the crack tip, constraint and geometry dependency. As Siegmund and Brocks [33] pointed out, to the present, "local approach" is the only really successful methods for prediction of crack growth resistance. In this kind of approach, one can simulate ductile fracture either by employing a micromechanical model of damage, which represents the micromechanism of void initiation, growth and coalescence, or by using a phenomenological model for material separation and coupling it to the surrounding undamaged elastoplastic material [34].

In a micromechanical model, a representative volume element (RVE) or "unit cell" is considered to study the respective mechanism. Such a micromechanical porous plastic-

ity model was originally proposed by Gurson [35] and later extended by Tvergaard and Needleman [36] which is so called GTN model.

In a phenomenological model, ductile crack growth in metals can be modeled by introducing a process zone ahead of the crack tip where material degradation and separation occur. This zone is embedded in an elastoplastic surrounding. Within the concept of the energy release rate, a "cohesive zone model" is introduced.

1.2.2 Cohesive zone model formulation

The cohesive zone model (CZM) removes the crack tip singularity and represents physics of the fracture process at the atomic scale. It regards fracture as a gradual phenomenon in which material separation takes place across an extended crack tip (cohesive zone) and is resisted by cohesive forces. A cohesive law (traction vs. separation) governs the constitutive behavior of crack opening in addition to the bulk stress-strain relation of surrounding material. No additional criterion is needed for fracture to occur. New crack surfaces are created as a natural result of constitutive evolution, thus maintaining continuity conditions mathematically despite the physical separation [37].

Generally, in crack propagation simulation, cohesive zone can be treated as the prescribed crack extension path, as shown in Fig. 1.2. The locations where material damage may occur have to be provided either from experimental observations, experienced data or numerical analyses. Within the framework of extended finite element methods (XFEM), the potential of CZM for arbitrary crack propagation has been exploited [38–42]. However, by applying XFEM in elastic-plastic problems, numerical difficulties arise significantly which leads to inevitable limitation.

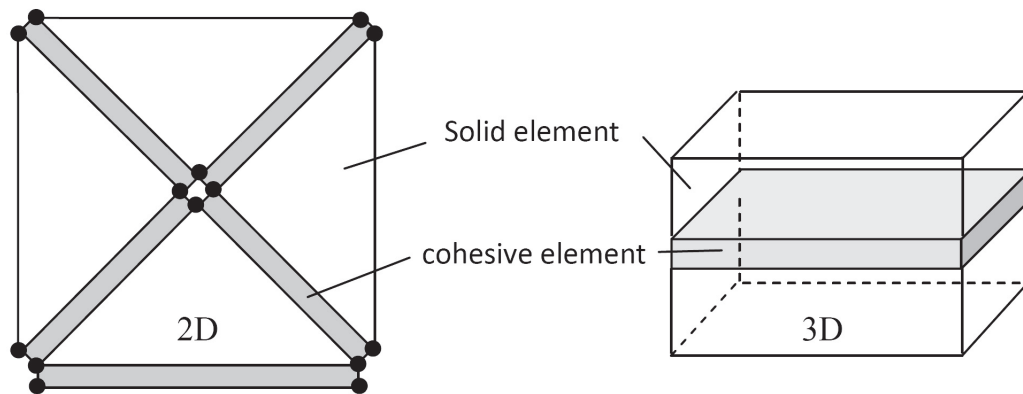


Figure 1.2: Schematic representation of the concept of cohesive/volumetric finite elements model [37].

Stress components within the cohesive zone no longer follow the constitutive law of the bulk material. Considering the contribution of the cohesive traction, the mechanical equilibrium statement of the cohesive zone in the form of the principle of virtual work can be written as

$$\int_V (\boldsymbol{\sigma} : d\boldsymbol{\varepsilon}) dV + \int_{S_{\text{int}}} (\mathbf{T} \cdot d\boldsymbol{\delta}) dS = \int_{S_{\text{ext}}} (\mathbf{t} \cdot d\mathbf{u}) dS, \quad (1.2)$$

where $\boldsymbol{\sigma}$ and $\boldsymbol{\varepsilon}$ are the Cauchy stress and strain tensor. V and S_{ext} represent the specimen volume and the external surface. \mathbf{t} means the traction vector at the external boundary and \mathbf{u} is the displacement vector. The integral term, $\int_{S_{\text{int}}} (\mathbf{T} \cdot d\boldsymbol{\delta}) dS$, over the crack surface and its prolongation in the process zone, S_{int} , represents the cohesive surface contribution of the cohesive zone ahead of the crack tip. \mathbf{T} denotes the cohesive traction components and $\boldsymbol{\delta}$ is the separation of the two adjacent cohesive surfaces.

Comparing with the conventional stress-strain relations of bulk material, the evolution of local traction vs. separation behavior within the cohesive zone can be defined as a constitutive law for the special field between the virtual crack surfaces.

1.2.3 Cohesive laws

The cohesive law is responsible for material degradation under different loading configuration. In general cases, both traction and separation are vectors, so that the cohesive law is defined in a vector equation. For a mode I crack, only normal traction vs. normal separation play a role in material failure, that is, the cohesive law expression reduces to a scalar traction-separation function, $T(\delta)$.

Within the cohesive zone, the damage increases when the traction is reduced. Complete failure is assumed when the separation is greater than an ultimate value. Common to all cohesive law shapes, the cohesive strength T_0 and the ultimate separation δ_u where the final failure occurs, are sufficient for modeling the separation process.

Fracture mechanics is built on energy balance around the crack tip and during crack propagation. The energy release rate should calibrate crack initiation and propagation in fracture mechanics methodology. In cohesive zone modeling, the crack should initiate and propagate based on the energy dissipation to separate the cohesive zone, which is defined as the cohesive energy Γ_0 , as

$$\Gamma_0 = \int_0^{\delta_u} T(\delta) d\delta. \quad (1.3)$$

1.2.4 Overview of the application of CZM

The early pioneering work on CZM can be traced back to 1960s. Dugdale [43] assumed an elastic-perfect plastic material behavior to avoid the unrealistic stress singularity around the crack tip. A narrow strip plastic zone ahead of the crack tip can be considered as cohesive zone. Barenblatt [44] later assumed cohesive force distribution in a sufficient large process zone along the crack ligament and the plastic strength is replaced by a cohesive law. The strip yield models of Dugdale and Barenblatt form the fundamental idea for CZM.

The first application of CZM to simulate the fracture behavior of a material was performed by Hillerborg et al. [45], as early as in 1976. The authors indicated that the cohesive stress at the crack tip has a linear descending relationship with the crack opening to describe the damage behavior of concrete. Needleman [46, 47] firstly induced CZM to investigate non-linear failure. The inclusion debonding in micro and macro scales were simulated by applying an exponential cohesive law.

In 1990, Yuan and Cornec [48] firstly employed CZM to investigate the crack extension in ductile materials. The ductile crack growth in an aluminium alloy was simulated by

using a constant cohesive law. Tvergaard and Hutchinson [13] computed the crack growth and subsequent resistance for an elastic-plastic solid through introducing a multilinear form cohesive law. Later, Scheider and Brocks [49] probed with most different function forms and studied influences on fracture process simulation. Goyal et al. [50] formulated an exponential form cohesive law by including a "brittleness" parameter, so that the flexibility of the cohesive law was enhanced.

In order to find more hints about the CZM, Krull and Yuan [51] investigated the atomistic separation with help of molecular dynamics and concluded the similarity between the exponential cohesive law of the normal failure process in the nano-scale.

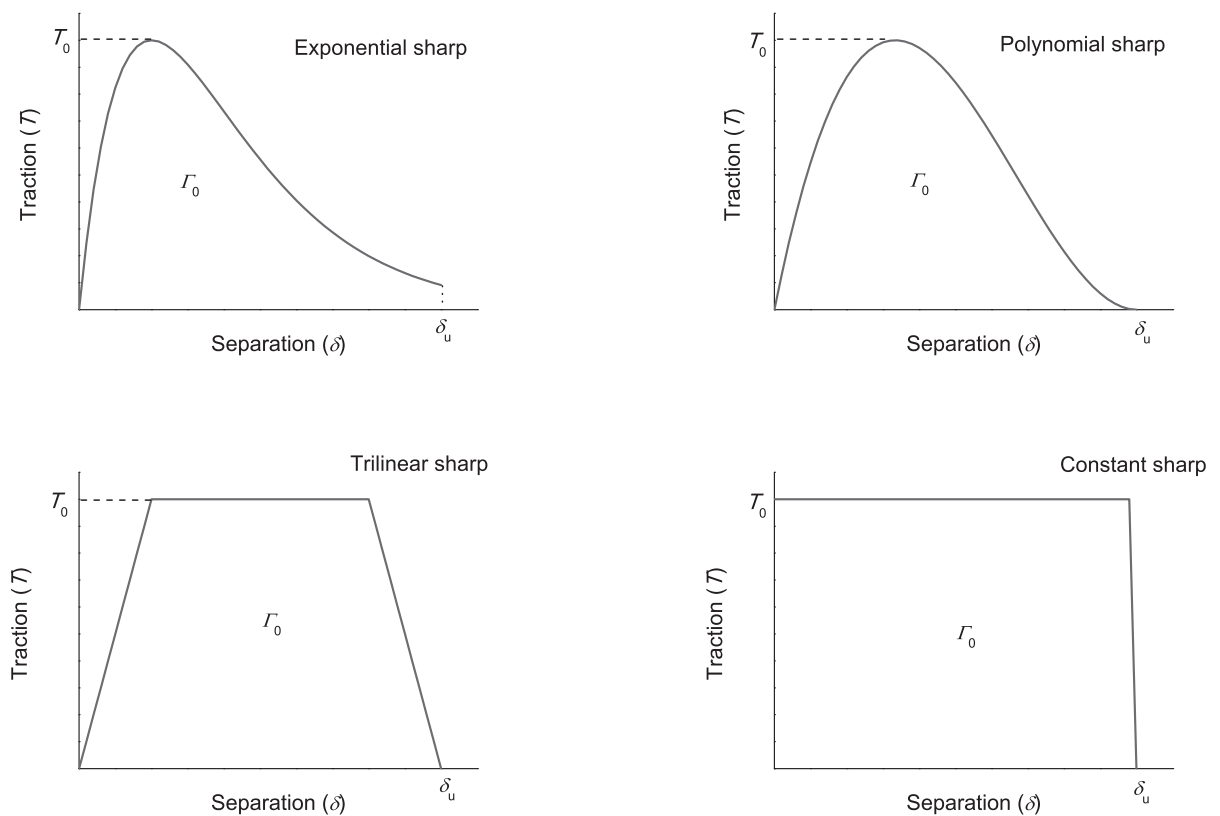


Figure 1.3: Schematic demonstration of different sharp cohesive law.

Various sharps of cohesive laws are shown in Fig. 1.3. Scheider and Brocks [52] showed that the shape of cohesive law has a significant influence on the results of crack extension of ductile materials. Different cohesive law sharps can make the same results in one specimen with different cohesive parameters. But the results might be significant different in another fracture specimen. Vossen et al. [53] denoted that cohesive zone elements generally do not satisfy rotational equilibrium for arbitrary cohesive laws. The error in the nodal forces can be neglected if the ratio of the ultimate separation to the length of the process zone is small. Yuan and Li [54] revealed that the initial stiffness of the cohesive law can induce significant errors into simulation if it is assumed improperly. Furthermore, the cohesive energy is generally smaller than the J -integral from FEM computation, caused by elastic

unloading around the crack tip. Based on such observations determining parameters of the CZM needs detailed special experiments. More detailed classification of different kinds of cohesive laws can refer to the literatures [55–60].

1.2.5 Constraint dependence of the cohesive parameters

Investigation has confirmed that the stress-state plays a crucial role in the damage growth till failure. Only a model which can account for the variations in stress-state in prediction of initiation and propagation of macroscopic crack would facilitate the transfer of fracture model parameters from a simple laboratory test to real complex structures [61].

However, up to now almost all studies using CZM to describe ductile crack growth assume the cohesive parameters to be material constants. Therefore, the effect of stress-state on the cohesive law has not been accounted for.

An early evidence for constraint dependence of the cohesive parameters can be found in the work of Yuan et al. [62]. The crack extension of thin-walled fracture specimens failing in a slanted manner was controlled by adjusting the cohesive energy in each element by experimental $v_{LL} - \Delta a$ curves. By reproducing the experimental data it turned out that the crack initiates with a Γ_0 value, which is equal to the crack initiation J_i for normal fracture, and then reduces to significantly lower values during the transition to the slanted fracture mode. After reaching the fully slanted region, the values remain almost constant again [32]. The result is shown in Fig. 1.4.

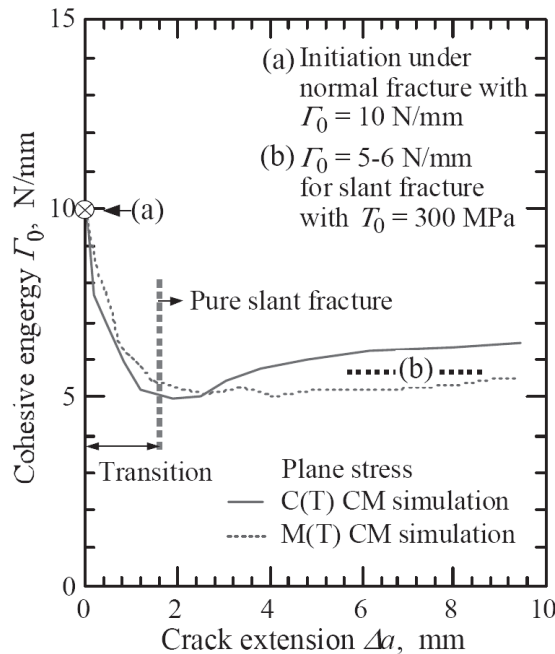


Figure 1.4: Development of the cohesive energy in the transition region from flat to slant fracture [62].

Ivankovic [63] measured a cohesive law in polyethylene using novel experimental method by notched tensile specimens. These results showed that both fracture energy and cohesive strength must be functions of the loading intensity and specimen geometry. It implies different cohesive laws for plane strain and plane stress.

For aforementioned reasons, recently, several papers on relationships between constraint effects and CZM were published. Unfortunately, most published works were mainly on in-plane constraint effects. Detailed discussions on existing models and formulation of a stress-triaxiality-dependent cohesive zone model (TCZM) will be presented systematically in Chapter 4.

1.3 Cyclic cohesive zone model

Cohesive zone modeling provides an alternative way to predict crack growth in ductile materials under elastoplastic loading conditions. Application of the cohesive zone model for fatigue crack propagation has to consider damage accumulation which is significant different from monotonic fracture. In order to simulate crack growth under cyclic loading, two aspects have to be taken into account additionally: the cyclic loading path and the damage evolution.

Within the cohesive zone, the constitutive behavior is exactly specified by correlation of the relative opening displacement and the corresponding traction. For the monotonic loading, the cohesive law is uniquely defined and is independent of the loading history, without un/reloading behaviors being considered. Under cyclic loading, in order to account for the irreversibility of the damage process, one has to introduce the un/reloading behaviors. Thus, the damage accumulation in fatigue is determined by the loading path and the material responding in the cohesive zone behaves loading history dependent. The correlation of traction and separation has to be reformulated to entail amount of the damage accumulation.

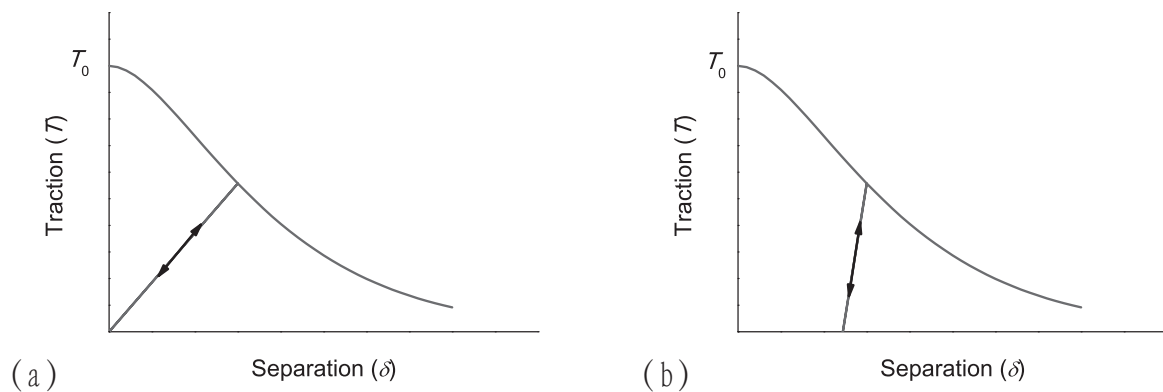


Figure 1.5: Cohesive law with un/reloading path for (a) elastic damage. (b) elastic-plastic damage.

Two types of unloading behaviors have been presumed for brittle and ductile failure respectively, as shown in Fig. 1.5. For an elastic damaged solid, Camacho and Ortiz [64] employed a linear unloading behavior towards the origin. For an elastic-plastic material under the consideration of damage, Chaboche et al. [65] suggested that unloading occurs with the initial stiffness at the origin, and after a completed loading cycle there exists the

possibility for the presence of a residual displacement. In this case, the irreversibility of the inelastic deformation could be taken into account.

Various approaches have been proposed regarding the application of cyclic cohesive zone model (CCZM). The state of art of proposed models will be reviewed in Chapter 5. To the knowledge of the author, most proposed CCZMs can only describe the Paris' law like behavior. The capabilities of CCZM to predict low cycle fatigue crack growth with severe plastification need further development.

1.4 Outline of the dissertation

Present work concerns the stress-state effect on the cohesive zone model and the application of the cohesive zone model for three-dimensional low cycle fatigue crack growth predictions. The contents of present thesis are performed by the following chapters:

1. In chapter 2, a special cohesive element is developed to study effects of the cohesive law. The influence of the initial stiffness of the cohesive law and the energy balance in crack simulation are investigated by using cohesive zone models. Interdependence among the threshold value of the cohesive laws, the cohesive stiffness, the cohesive strength and the fracture energy of the cohesive zone is considered systematically.
2. In chapter 3, to validate the efficiency and the predictability of the cohesive zone model in three-dimensional computations, the LCF crack growth behavior of S460 specimens is investigated experimentally under mode I loading condition. Fatigue tests are carried out on the cracked rod bars to examine the surface crack evolution. Furthermore, to quantify the geometry effect on fatigue cracks, the fatigue tests are performed on C(T) specimens with different thicknesses. The failure mechanisms are analysed by comparing the local crack profiles and the fatigue crack growth rates.
3. In chapter 4, a new stress-triaxiality-dependent cohesive zone model (TCZM) is proposed to allow to transfer the cohesive parameters between specimen geometries. The stress-state effect is significant on ductile crack growth, which must influence the cohesive parameters as well. The correlations of the stress triaxiality and the cohesive parameters are obtained based on the experiments, which are performed for quantifying the in-plane and the out-of-plane constraint in three-dimensional cracks. Furthermore, the proposed TCZM is applied for three-dimensional crack propagation simulation.
4. In chapter 5, a new cyclic cohesive zone model (CCZM) is constructed which can characterize the fatigue damage with severe plastic deformation and can predict the fatigue crack growth in Regime III. The experimental fatigue crack growth data of the ductile materials are used for calibrating the new model.
5. In chapter 6, the proposed CCZM is extended to consider the stress-state effect, which can be named as the stress-triaxiality-dependent cyclic cohesive zone model (TCCZM). The influence of the stress-state effect are considered on the cohesive law as well as on the damage evolution equation. The predictions are performed in different specimens for three-dimensional low cycle fatigue crack growth. Numerical



results, i.e. the crack growth rate and the local crack profiles, are verified with the experimental three-dimensional cracks.

6. Finally, in chapter 7, the main results are summarized and some suggestions are recommended for the possible future work.

2 Effects of the cohesive law for ductile crack simulation

2.1 Introduction

Material failure is often accompanied by elastic unloading and plastic reloading round the crack tip. This problem becomes especially significant for elastic-plastic crack propagation under low cycle fatigue conditions, where the Paris' law cannot be applied due to large scale of non-proportional inelastic deformations. Recently, the cohesive zone model is popular in computational fracture mechanics' community. One of key advantages of the cohesive zone model is in separating the material deformation from material failure in computations [55]. That is, material deformation in a cracked specimen is described by the continuum plasticity, whereas material damage is predicted by the cohesive zone model. The fracture process zone is simplified into a strip ahead of the crack tip. Obviously, the accuracy of the cohesive zone modeling is influenced by constitutive description of the cohesive zone. Quantification of effects of different cohesive zone models is still an open issue.

2.1.1 Rigid cohesive zone

At very low loading level of a cracked specimen, the fracture process zone is vanishingly small, the material around the crack is not damaged and the cohesive zone should not exist. It follows that the cohesive zone initiates only if the traction ahead of the crack tip exceeds a critical value, i.e. the threshold value of the traction. In this case, the initial stiffness of the cohesive zone is infinite, a *rigid cohesive zone* [39–42]. An illustration of *rigid cohesive zone* is shown in Fig. 2.1. This cohesive zone model formulation leads to a discontinuous cohesive law $T(\delta)$ and is numerically difficult to handle. The conventional FEM element cannot take such discontinuous traction-separation law into account. Therefore, most published cohesive laws prefer to assume a continuous traction-separation relation starting from zero traction. That means, the cohesive zone exists even without loading, a *soft cohesive zone*. The size of the soft cohesive zone is affected by the cohesive stiffness. The question here is how the cohesive stiffness would influence the computational results.

The soft cohesive zone model is physically contradictory to continuum mechanics, but numerically necessary if one uses the conventional finite element method. On the other hand, the rigid cohesive zone model needs special numerical algorithm and encountered major problems with the convergence in simulation of fatigue crack, as XFEM. Elices et al. [56, 66] studied effects of the cohesive law to crack simulation and discussed initial shapes of the cohesive law, however, did not quantify effects of the cohesive stiffness. Quantification of the initial cohesive stiffness to the crack simulation is of importance for further development of the cohesive zone models.

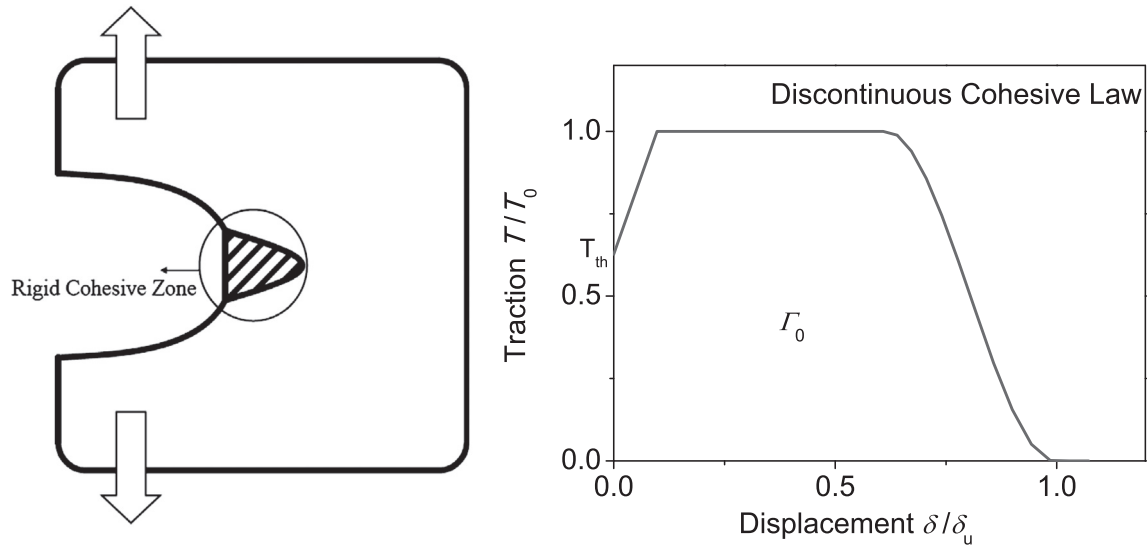


Figure 2.1: The cohesive zone ahead of the crack tip described by a cohesive law with threshold, T_{th} . The cohesive energy Γ_0 denotes the area under the cohesive curve.

2.1.2 Motivation

Fracture mechanics is built on energy balance around the crack tip and during crack propagation. The energy release rate should calibrate crack initiation and propagation in fracture mechanics methodology. In cohesive zone modeling, the crack should initiate and propagate based on the energy dissipation in the cohesive zone, which is defined in Eq. (1.3). Commonly, the cohesive energy Γ_0 , is assumed to equal the energy release rate in fracture mechanics [13, 47–49, 67, 68]. Yuan et al. [62] studied variations of the cohesive energy in crack initiation and subsequent crack propagation. It was found that the cohesive energy for crack initiation is significantly larger than Γ_0 for steady-state crack propagation. Computational results [69] show the cohesive energy seems smaller than the far-field J -integral, almost by factor 2. Schwalbe et al. [59] reported differences between fracture energy and cohesive energy. Both cohesive law and cohesive energy can affect the computational prediction. Based on these observations, it is interesting to re-examine the correlation between the cohesive energy and the energy release rate of fracture.

In this section, a special cohesive element is developed to study effects of the cohesive law, so that both rigid and soft cohesive zones can be considered accurately. The influence of the initial stiffness of the cohesive law and the energy balance in crack simulation are investigated by using cohesive zone models. Interdependence among the threshold value of the cohesive laws, the cohesive stiffness, the cohesive strength and the fracture energy of the cohesive zone is considered systematically.

2.2 Formulation of the cohesive element with a threshold traction

The rigid cohesive zone model requires creating a new surface into the computational model, which cannot be realized by the conventional finite element and continuum formulation. For this reason, a new element is necessary to create new cracks. For general mixed mode cracks, one has to use the XFEM. Under mode I loading conditions, the crack tip field is symmetric to the crack plane and only a half of the specimen has to be discretized [70]. The cohesive zone initiates and propagates along the symmetric plane. If the cohesive law contains a threshold value, the cohesive zone initiates only if the traction ahead of the crack tip exceeds the threshold value. In the present work, only mode I cracks will be considered, so that a crack lies in the symmetric plane of the specimen. One may use the node release technique to simulate crack propagation combined with the cohesive law [62].

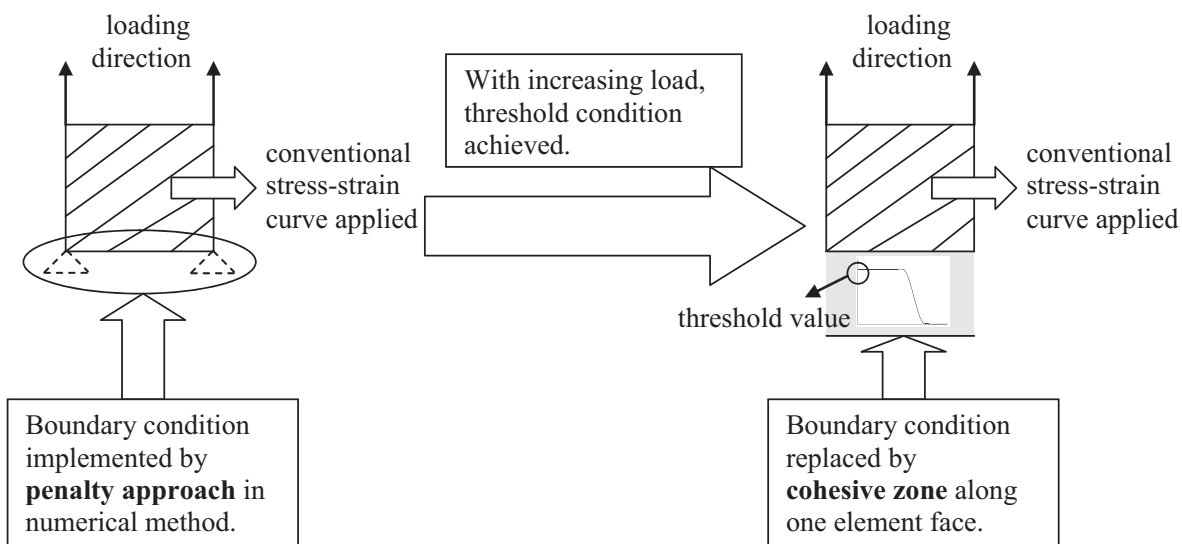


Figure 2.2: The schematic representation of the cohesive element and its algorithm in ABAQUS [71].

The representation of the cohesive element with threshold traction is illustrated in Fig. 2.2. Fig. 2.3 shows the flow chat of the computational algorithm. The solid element takes the conventional FEM formulation if the traction is less than the threshold value. The potential cohesive zone is located at the edge of the element with zero separation. The traction is determined from the equilibrium equation. If the element stress does not exceed the threshold of cohesive law, the element works like a conventional continuum element. The element boundary is fixed due to symmetry and enforced to close using the penalty method [72]. However, as soon as the stress in the element exceeds the threshold value, the node will be loaded by a nodal force and the fixed element boundary will be replaced by the cohesive zone. An increment of the cohesive zone is formed. Variations of the traction at the element edge follow the cohesive law as a function of the separation. In the following steps the nodal force of the element surface will be released gradually, in accordance with the cohesive law. If the ultimate separation is reached, the node is totally free and a crack

increment is generated. To improve accuracy of the computations, the stress in the element ahead of the crack tip will be averaged following the algorithm in [42].

The present element can also be applied for the soft cohesive zone modeling by setting $T_{th} = 0$. In this case, the cohesive zone exists in the whole uncracked ligament. The traction varies with the separation.

The three-dimensional finite element formulation above has been implemented into the general purpose commercial FEM code, ABAQUS, via the user-defined element (UEL) [71]. Extensive verifications have been performed for the programming.

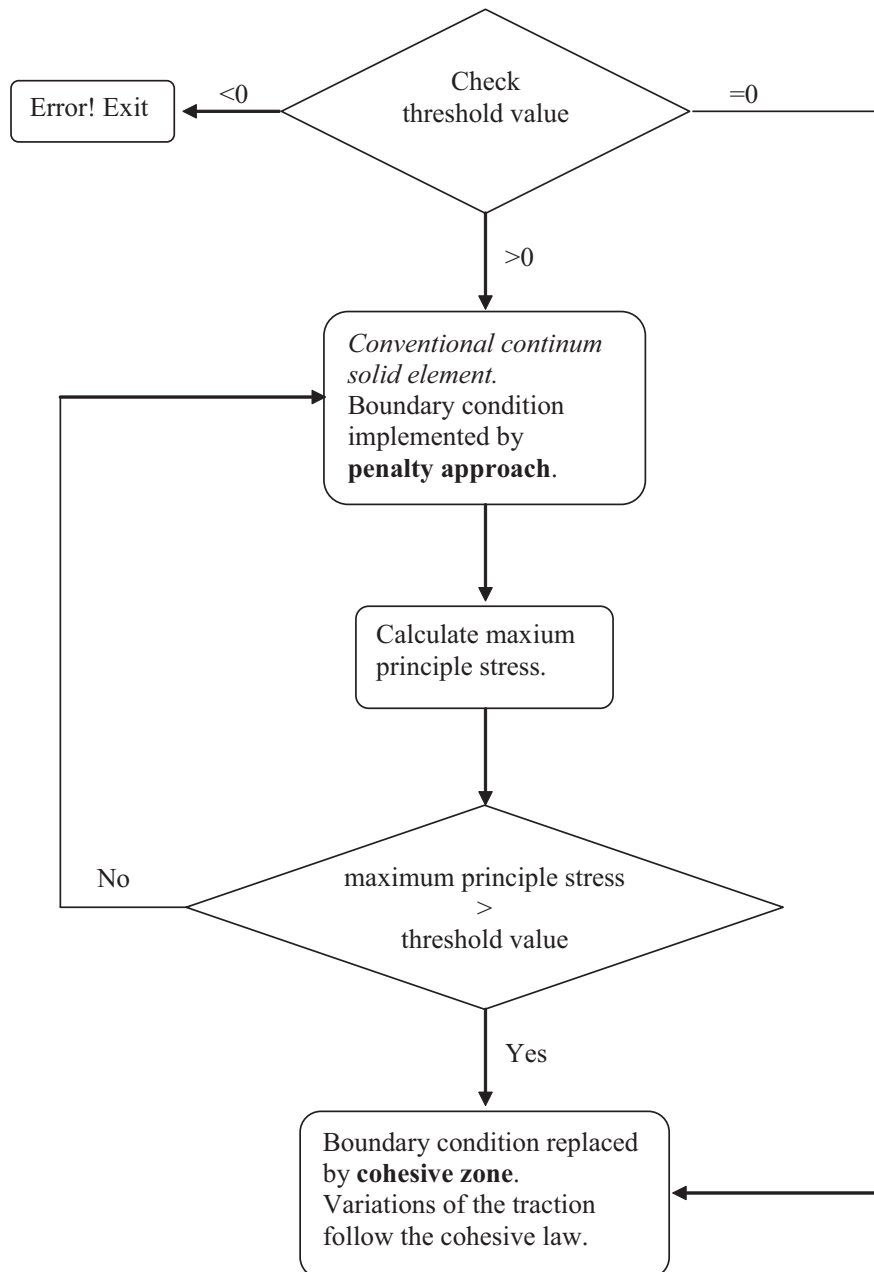


Figure 2.3: The flow chat of the cohesive element algorithm.

In the past, various cohesive laws have been suggested in different forms. Basically, the cohesive strength and the cohesive stiffness can significantly affect computational results.

To study effects of the cohesive stiffness in crack simulation, the cohesive law with constant cohesive strength, T_0 , is used in the current section, as shown in Fig. 2.4. The function is to jot as [49, 59]

$$T = T_0 \begin{cases} \left(\frac{\delta}{\delta_1}\right) & \delta \leq \delta_1 \\ 1 & \delta_1 < \delta \leq \delta_2 . \\ 2\left(\frac{\delta - \delta_2}{\delta_u - \delta_2}\right)^3 - 3\left(\frac{\delta - \delta_2}{\delta_u - \delta_2}\right)^2 + 1 & \delta_2 < \delta \leq \delta_u \end{cases} \quad (2.1)$$

In the cohesive law above there are four parameters, the cohesive strength, T_0 ; the separation for the initial linear hardening stage, δ_1 ; the separation to end the constant cohesive strength, δ_2 , and the ultimate separation for failure, δ_u . δ_1 is introduced to vary the cohesive stiffness of the cohesive zone. The specific stiffness of the cohesive zone can be quantified by

$$\Psi = \frac{T_0}{\delta_1} \zeta. \quad (2.2)$$

Above ζ denotes the characteristic length of the cohesive zone and is introduced to simplify representation of the cohesive zone model in continuum mechanics. In the present work $\zeta = 1$ mm is set for all computations.

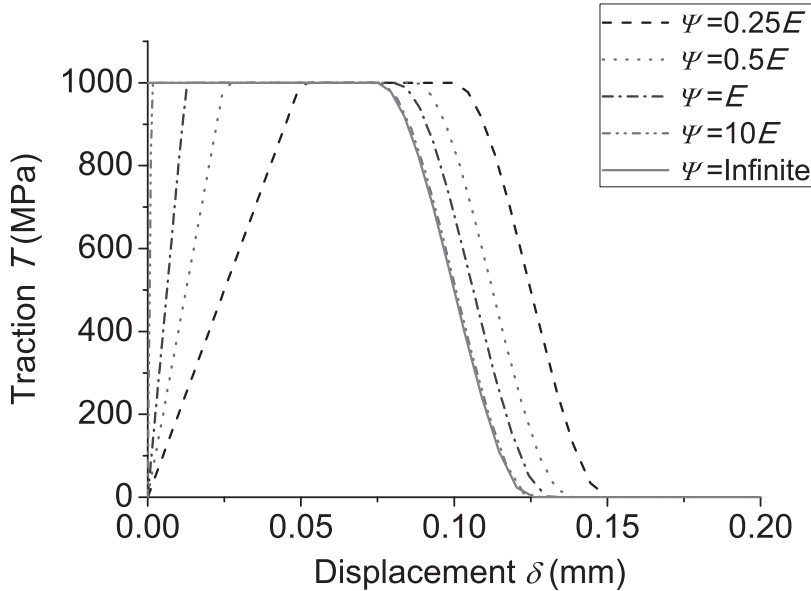


Figure 2.4: Cohesive laws in Eq. (2.1) to study effects of the cohesive zone stiffness. All curves contain the same cohesive energy Γ_0 .

Systematic changes of δ_1 by keeping constant T_0 lead to various cohesive stiffnesses of the cohesive zone. Should δ_1 be zero, i.e. the cohesive stiffness Ψ becomes infinite, the cohesive zone is rigid before T_0 is reached, and the cohesive law is discontinuous. The rigid

cohesive zone model was used to investigate the applicability of the cohesive zone model concept for ductile crack propagation. The cohesive energy defined in Eq. (1.3) can be re-written as

$$\Gamma_0 = \frac{1}{2}T_0\delta_1 + T_0(\delta_2 - \delta_1) + \frac{1}{2}T_0(\delta_u - \delta_2). \quad (2.3)$$

The total cohesive energy consists of elastic cohesive energy, Γ_{el} , the cohesive dissipation energy, Γ_{pl} , and the cohesive damaging energy, Γ_{sf} , defined as

$$\Gamma_{el} = \frac{1}{2}T_0\delta_1, \quad \Gamma_{pl} = T_0(\delta_2 - \delta_1), \quad \Gamma_{sf} = \frac{1}{2}T_0(\delta_u - \delta_2), \quad (2.4)$$

respectively. The elastic cohesive energy is reversible and vanishes if load is removed. The plastic cohesive energy can dissipate even if unloading occurs [42], e.g. in simulation of fatigue crack growth. The damaging energy describes ductility during material degradation.

For the current investigation, we assume a constant cohesive strength, $T_0 = 4\sigma_y$, and the cohesive energy, $\Gamma_0 = 100 \text{ N/mm}$. To ensure the same softening behavior for all cases, the cohesive damaging energy is assumed as $\Gamma_{sf} = \frac{1}{2}T_0(\delta_u - \delta_2) = 25\%\Gamma_0$. The cohesive stiffness Ψ varies from infinite (the rigid cohesive zone) to very soft cohesive zone with $\Psi = E/4$.

The J_2 plasticity with the Ramberg-Osgood hardening law is applied for the elastic-plastic material,

$$E\varepsilon = \sigma + \alpha\sigma_y\left(\frac{\sigma}{\sigma_y}\right)^{\frac{1}{n}}. \quad (2.5)$$

The material parameters are set in accordance with aluminum alloy with Young's modulus $E = 80 \text{ GPa}$, Poisson's ratio $\nu = 0.3$, initial yield stress $\sigma_y = 250 \text{ MPa}$, $\alpha = 1$ and $n = 0.1$.

2.3 Effects of the cohesive stiffness

To illustrate effects of the cohesive stiffness, a standard compact tension (C(T)) specimen with initial crack length of 25 mm is computationally investigated under plane strain conditions with a constant cohesive energy Γ_0 , as shown in Fig. 2.4. Fig. 2.5 shows the force vs. load line displacement curves from computations with various cohesive stiffnesses. Ψ varies from $E/4$ to infinite (the rigid cohesive zone). Generally speaking, the stiffness of the cohesive law raises the specimen resistance and causes higher loading capacity. The results confirm, however, that the global reaction of the specimen is not sensitive to the cohesive stiffness. For $\Psi > E$, the load-load line displacement curve is numerically independent of the cohesive stiffness. The maximum deviation is less than 3%. Variations of the cohesive stiffness influence local deformations around the crack tip, but the overall behavior is hardly affected by the local deformations. The load vs. load line displacement curve is mainly determined by the fracture energy and the cohesive strength.

One would expect the crack tip opening displacement (CTOD) should be more sensitive to the cohesive stiffness. In Fig. 2.6 the crack tip opening displacement after Schwalbe et al. [6], δ_5 , is plotted as a function of the load line displacement for various cohesive stiffnesses. As expected, the δ_5 value from a softer cohesive law becomes larger. Crack initiation of all computations approximately occurs at the loading ca. $v_{LL} = 5 \text{ mm}$, at

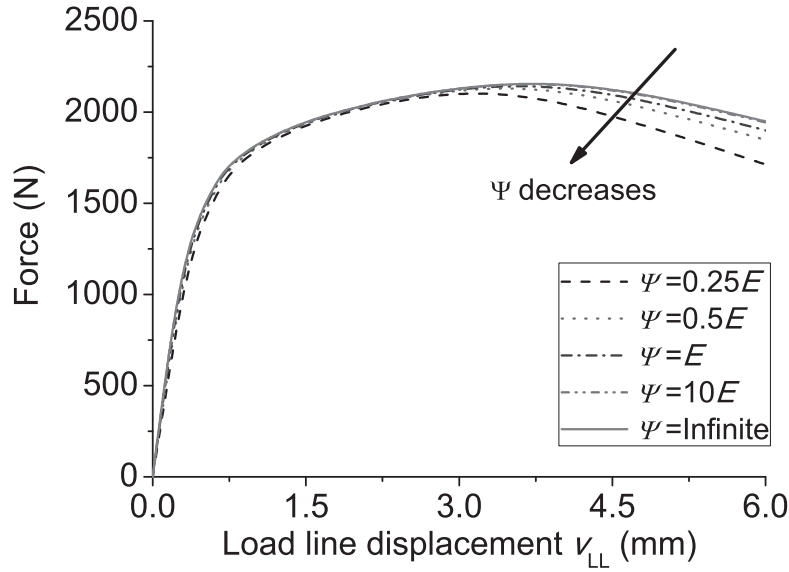


Figure 2.5: Load vs. loading line displacement for C(T) specimen using various cohesive laws.

which the discrepancy between different cohesive stiffnesses does not seem large enough for correction. The maximal difference is limited by δ_u , which is much smaller than the final fracture separation. For $\Psi > E$, the difference of δ_1 for various Ψ is less than 0.1 mm, which is much smaller than the CTOD at crack initiation. Therefore, the effect of Ψ becomes negligible. With crack propagation, the discrepancy is accumulated and grows. Deviations of the fracture parameters are, however, limited to 5% if $\Psi > E$.

More quantified results about the δ_5 discrepancy are presented in Fig. 2.7. In the figure, the deviations of the δ_5 values for $v_{LL} = 1.5$ mm, 3 mm, 4.5 mm and 6 mm are summarized as functions of E/Ψ . δ_5 of the rigid cohesive zone is taken as reference, denoted as δ_{50} . Obviously, the crack tip opening displacement grows, as the cohesive stiffness decreases, and the deviation increases linearly with E/Ψ . For the cohesive stiffness $\Psi \geq E$, however, the difference is less than 5%.

The cohesive law influences crack propagation. Fig. 2.8 shows crack growth vs. load line displacement for various cohesive stiffnesses. Significant differences of crack growth are found in Fig. 2.8. The lower cohesive stiffness leads to more rapid crack growth. This trend is similar to the δ_5 curves, but shows much larger discrepancy. More results are shown in Fig. 2.9 with crack growth difference as a function of the cohesive stiffness. The reference crack growth Δa_0 is taken from the rigid cohesive zone modeling. The figure shows crack growth at three different loading stages: $v_{LL} = 3$ mm, 4.5 mm and 6 mm. The results confirm that the predicted crack growth is very sensitive to the cohesive stiffness. For the case with the cohesive stiffness $\Psi = E$, the predicted crack propagation deviates more than 35% from the rigid cohesive model. For $\Psi \geq 5E$, the deviation is less than 1%. Generally, the soft cohesive zone model will delay crack propagation, compared to the rigid cohesive zone model.

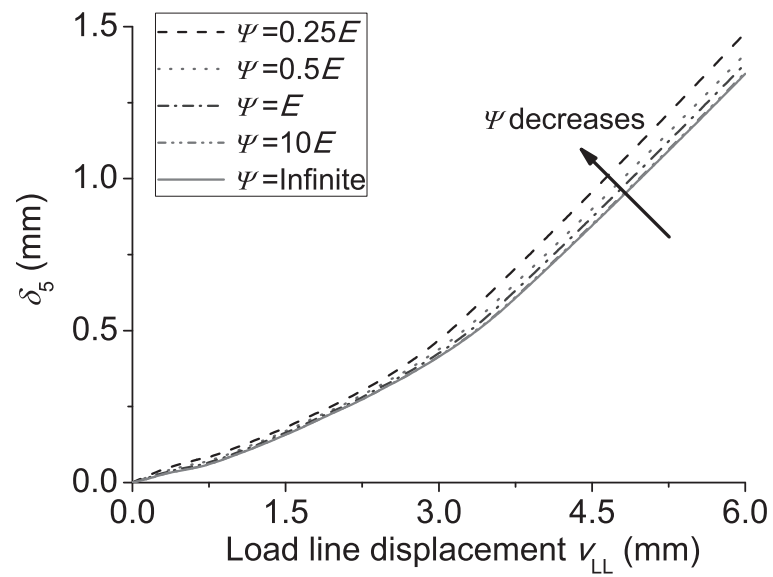


Figure 2.6: The CTOD δ_5 vs. loading line displacement for various cohesive stiffnesses.

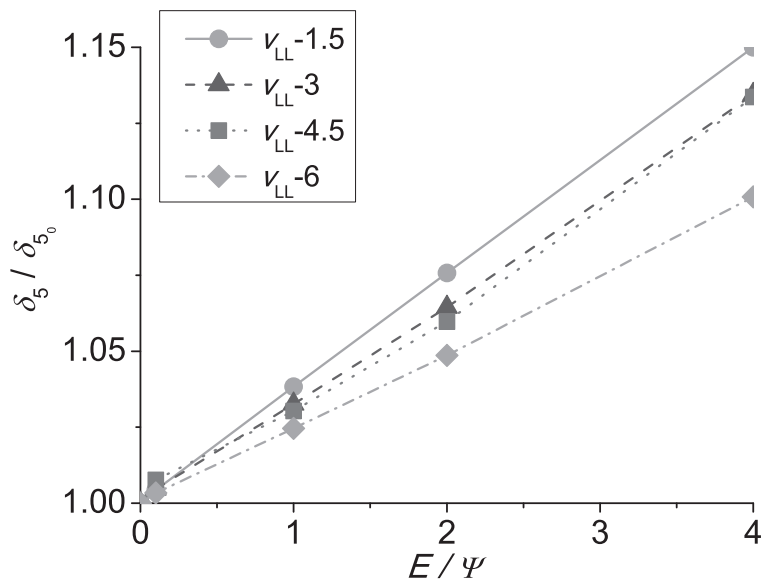


Figure 2.7: Influence of the cohesive stiffness to the fracture parameter δ_5 .

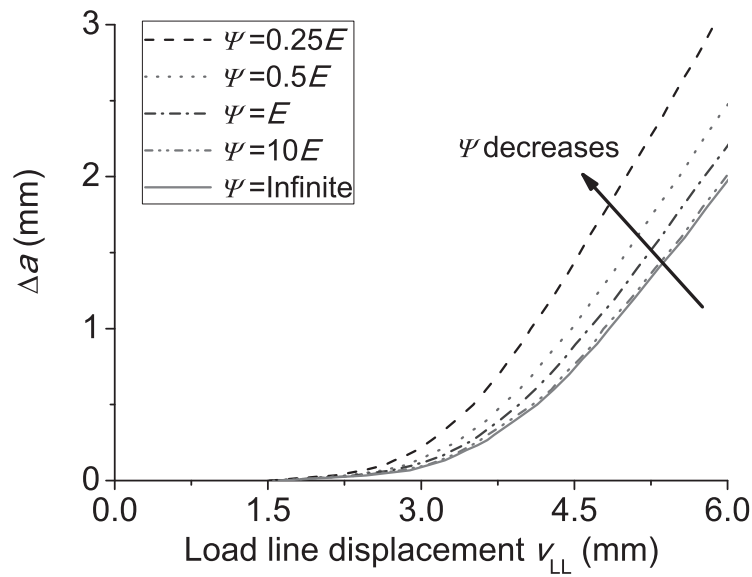


Figure 2.8: Δa vs. load line displacement for the various cohesive stiffnesses.

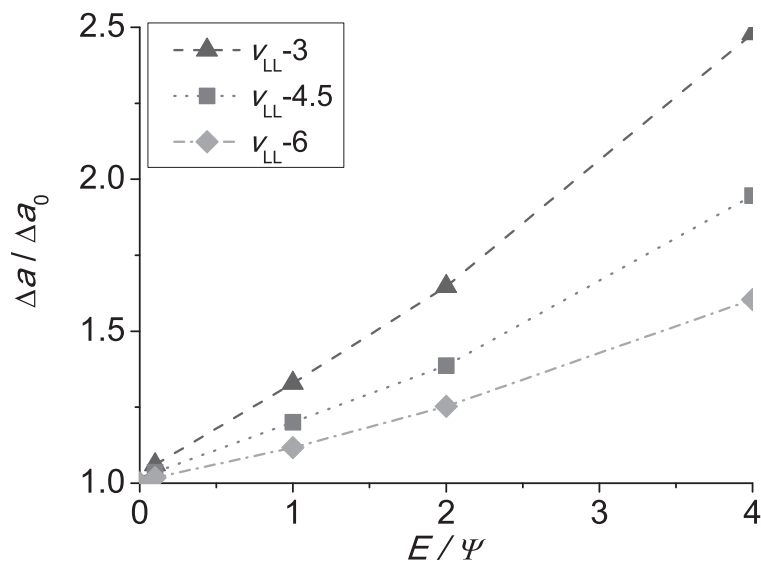


Figure 2.9: Influence of the cohesive stiffness on crack propagation Δa .

2.4 Energy balance in crack propagation with a cohesive zone

In nonlinear fracture mechanics the energy release rate is introduced as fracture parameter, which can be evaluated based on the J -integral. The fracture energy for crack initiation is equal to the energy input from the applied load represented by the far field J -integral due to its path-independence. In FEM, the J -integral is calculated using the virtual crack extension technique [71]. The fundamental condition for the energy consideration is the conservative mechanics field in the cracked specimen. Only energy dissipation is caused by the crack propagation. Under this condition, the J -integral can be evaluated as

$$J = \int_S W dy - t_i u_{i,1} dS, \quad (2.6)$$

where W denotes the strain energy density, t_i is the traction vector along the integration path S , u_i is the displacement vector. The illustration of integral path for J -integral is shown in Fig. 2.10. For a crack field under deformation theory of plasticity, the J -integral is independent of S and is related with the energy dissipation in the fracture process zone,

$$J = \int_{S_c} W dy - \mathbf{T} \cdot \frac{d\mathbf{u}}{dx} dS = - \int_{S_c} \mathbf{T} \cdot \frac{d\mathbf{u}}{dx} dS = J_{\text{tip}}. \quad (2.7)$$

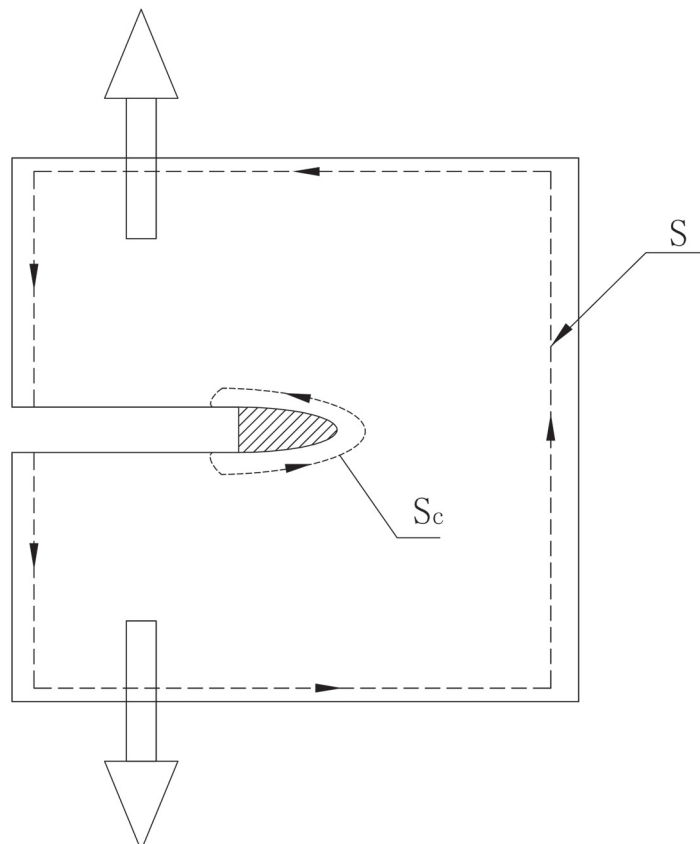


Figure 2.10: Integral paths for the J-integral.

Since the integration is conducted along the surfaces of the cohesive zone, the vertical height of the integration path is zero and thus the first integral in Eq. (2.7) over y vanishes. J_{tip} denotes the energy dissipation for crack growth.

The condition for the path-independent J -integral is the existence of a potential function W , that is, the stress field in an elastic-plastic material may not allow non-proportional loading and elastic unloading [73]. Eq. (2.7) is valid only for nonlinear elastic behavior around the crack tip. In simulation of crack propagation in elastic-plastic materials, the crack field is accompanied by significant elastic unloading, so that the J -integral becomes path-dependent. The distribution of the path-dependent J -integral is an increasing function of the path size [74]. The energy input from the applied load is absorbed by both creating new crack surface and plastification of material surrounding the crack tip,

$$J = J_{\text{tip}} + J_{\text{pl}}, \quad (2.8)$$

with $J_{\text{pl}} > 0$. Only if the crack tip field is a potential field, J_{pl} vanishes. Since both energy amounts, J_{tip} and J_{pl} , are positive, the J -integral representing the total energy input from the applied load is generally larger than the fracture energy for creating crack surface, J_{tip} .

If the cohesive zone exists ahead of the crack tip, the integration (2.7) runs along the cohesive zone borders, S_c . The traction, \mathbf{T} , in Eq. (2.7) denotes the cohesive traction of the cohesive zone and is a function of separation of the cohesive zone, $[\mathbf{u}]$. It follows

$$J_{\text{tip}} = \int_{u_-}^{u_+} \mathbf{T} \cdot d\mathbf{u} = \Gamma_0. \quad (2.9)$$

The crack tip J -integral equals the cohesive energy, Γ_0 . If no elastic unloading occurs around the cohesive zone, $\Gamma_0 = J_i$. Here J_i denotes the J -integral in the far field, or the critical fracture energy release rate for crack initiation.

Recalling the cohesive zone modeling, the ductile fracture process should be considered in the nonlinear traction-separation curve, the cohesive law. The cohesive energy, Γ_0 , represents the fracture energy for creating a unit crack surface. During crack blunting, the material around the cohesive zone is severely plastified and absorbs mechanical energy. The absorbed energy in the plastic zone dissipates during elastic unloading induced by the cohesive damage, that is, the cohesive strength decreases with separation. Since the cohesive zone model describes a continuous damage process, the critical energy release rate varies with the cohesive law. Due to cohesive damage, crack tip field becomes non-proportionally loaded or even unloaded. The J -integral loses its path-independence even before crack initiates.

Figure 2.11 shows variations of the J -integral at crack initiation, J_i , with the specific cohesive stiffness, E/Ψ , by keeping constant cohesive strength, T_0 , and constant cohesive energy, Γ_0 (as shown in Fig 2.4). Understandably, J_i is larger than the cohesive energy Γ_0 , but decreases monotonically with E/Ψ . Since the cohesive strength is generally higher than yield stress of the bulk material, the plastic zone size decreases with E/Ψ . When the material is damaged, the cohesive traction diminishes and, that is, the bulk material around the crack tip is elastically unloaded, it leads to plastic energy dissipation and J_{pl} increases. For a soft cohesive zone (smaller Ψ), the plastic dissipation energy is less than that of a rigid or hard cohesive zone. The fracture energy difference between a rigid cohesive zone and a cohesive zone with the stiffness $\Psi = E$ is 6.25%. It implies that the cohesive stiffness affects the critical energy release rate slightly, for a high cohesive strength $T_0 = 4\sigma_y$.

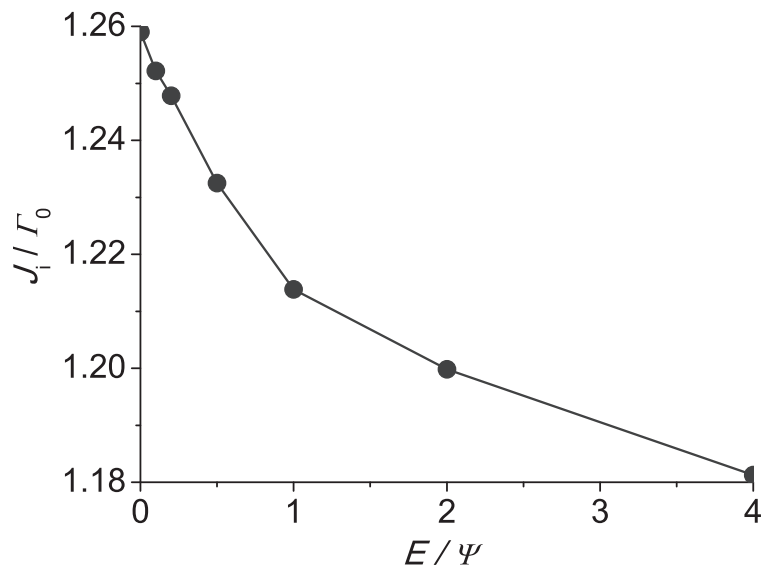


Figure 2.11: The energy release rate at crack initiation as a function of the cohesive stiffness with $T_0 = 4\sigma_y$.

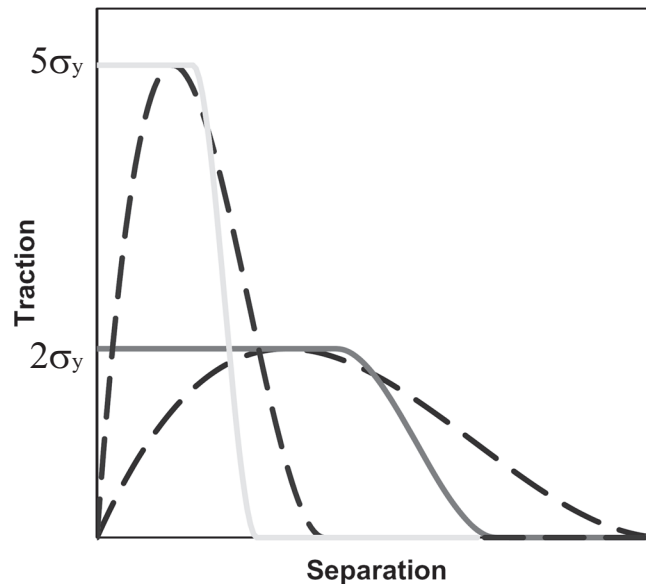


Figure 2.12: Different cohesive laws used for studying fracture energy at crack initiation. The solid curves are described by Eq. (2.1), whereas the dashed curves are from Eq. (2.10).

Furthermore, the cohesive strength and the curve form may affect the fracture energy in crack simulation. To study effects of the cohesive law more systematically, a polynomial cohesive law is additionally defined as

$$T = \begin{cases} \frac{27}{4} T_0 \frac{\delta}{\delta_u} \left(1 - \frac{\delta}{\delta_u}\right)^2 & \delta \leq \delta_u \\ 0 & \text{otherwise} \end{cases} \quad (2.10)$$

The significant difference of the polynomial law from Eq. (2.1) is in the cohesive stiffness, as shown in Fig. 2.12. The rigid cohesive zone model of Eq. (2.1) contains a constant traction after cohesive zone initiation, whereas the model of Eq. (2.10) is a soft cohesive zone model. The cohesive strengths are assumed to be $2\sigma_y$ and $5\sigma_y$, respectively. δ_u is determined by the constant cohesive energy. All curves contain the same cohesive energy of $\Gamma_0 = 100 \text{ N/mm}$.

Fig. 2.13 illustrates dependence of the fracture energy at crack initiation on the cohesive law. Only fracture energy release rate for crack initiation is considered. Each point in the figure is an independent computation. For the case with $T_0 = \sigma_y$, the whole specimen is purely elastic and no plastic dissipation exists, i.e. $J_i = \Gamma_0$.

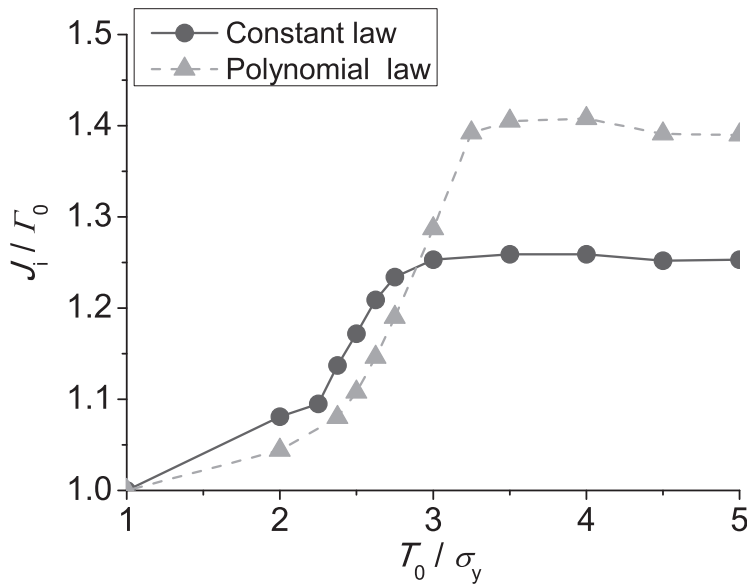


Figure 2.13: Effects of the cohesive law to the fracture energy at crack initiation.

The plastic zone around the crack tip grows with T_0 and elastic unloading becomes more severe. It follows larger plastic dissipation and higher fracture energy since more mechanical energy flows into plastification, that is, the ratio J_i/Γ_0 increases. For high enough T_0 , however, the plastic energy dissipation reaches a plateau since the plastic zone size becomes constant determined by Γ_0 , as predicted in fracture mechanics. The plastic zone size is related to

$$r_p = \alpha \frac{J_i}{\sigma_y}, \quad (2.11)$$

with α as dimensionless factor. It follows that, J_i/Γ_0 becomes constant for further increasing T_0 . The critical value of T_0 should be sufficiently high to avoid its influence on the energy balance in crack initiation, although it is difficult to be determined analytically. Obviously, the critical value of T_0 depends on the cohesive law. The present computations reveal that the critical value of T_0 is approximately $3\sigma_y$ for constant J_i/Γ_0 in both types of the cohesive laws.

Generally speaking, the difference between fracture energy and cohesive energy is substantial. For plane strain computations with $T_0 > 3\sigma_y$, the deviations become stable and reach 30% for the rigid cohesive zone model and 40% for the polynomial soft cohesive zone model, which is influenced by the cohesive stiffness in combining with T_0 . Due to its higher cohesive stiffness, the energy dissipation in the rigid CZM rises more quickly and stabilizes at a lower T_0 value. The polynomial CZM generates higher energy dissipation for its lower cohesive stiffness and stabilizes at a higher T_0 . Generally, to perform a quantitative simulation of the cracked specimen, one has to note the difference between the cohesive energy and J_c . The cohesive energy is smaller than the fracture energy release rate for crack initiation.

2.5 Summary

Two fundamental issues about the cohesive law have been studied from computational aspects: the cohesive stiffness and the fracture energy balance in using the cohesive zone model. For this purpose, a special cohesive element has been developed and implemented into the commercial FEM code ABAQUS. Computational results confirm the following conclusions:

- Effects of the initial cohesive stiffness are negligible in the load vs. load line displacement curve, but limited up to 5% for the fracture parameter, such as δ_5 . The soft cohesive zone model generates the higher δ_5 value.
- In predicting the crack propagation amount the cohesive stiffness becomes more sensitive. The Δa deviations among models reach 35%, even for a stiffer cohesive zone model ($\Psi = E$). The over-estimate of the crack growth increase linearly with E/Ψ . To obtain a realistic crack propagation, one has to further increase the stiffness of the cohesive zone to $\Psi = 5 - 10E$.
- The fracture energy release rate from the cohesive zone model computation is generally not equal to the cohesive energy, Γ_0 . The J -integral for crack initiation is significantly larger than Γ_0 . The difference depends on the cohesive law and disappears only in an elastic specimen. With increasing cohesive strength, the discrepancy grows and becomes stable for $T_0 > 3\sigma_y$ under plane strain loading conditions. The maximum deviation exceeds 40%.

3 Experimental investigation on fatigue cracks

3.1 Introduction

The cohesive zone model has been particularly attractive for practical application since it is very computation effective. To verify the efficiency and the predictability of CZMs, the experimental data are desired under both monotonic and cyclic loading conditions. Experiments should be carried out to provide the material response associated with crack growth. In addition, the applications of CZM with cyclic loading need to quantify the crack growth rate under different loading conditions. In the present study, experimental works will contain three major topics:

- In the metallic structure, most failure occurs often developing from the surface cracks propagation. It is well known that the stresses near a crack tip have a square-root singularity and are characterized by the stress intensity factor (SIF). However, for the structural components with a round cross section, the problem is complex since the SIF varies along the crack front and its closed solution is not always available. Furthermore, the shapes of the surface crack vary during the fatigue crack propagation of a rod bar. Experimental tests and numerical studies will be performed in the present study to examine the fatigue crack growth behavior of a rod bar. Backtracking technique is applied to record the surface crack evolution and the actual surface crack is represented by an elliptical arc.
- For the ductile fracture, the variables influencing the fracture resistance include the microstructural properties, the continuum properties of the solid, and the crack tip constraint. The crack tip constraint influences both the amount of plastic deformation and the material degradation process in the fracture process zone. In the low cycle fatigue regime, the similar mechanism will dominate the fatigue crack growth, which must depends on the stress-state as well. Therefore, it would be interesting to quantify the fatigue cracks under different constraint conditions. In the present study, the geometry effect on fatigue cracks will be examined by performing the fatigue tests on C(T) specimens with different thicknesses. The failure mechanisms are analysed by comparing the local crack profiles and the fatigue crack growth rates.
- Since the CZM is a phenomenological model, the identification of the damage evolution within the cohesive zone based on the experimental evidences is still an open issue. In the present work, special compact-tension-shear (CTS) specimens with different notch heights are designed to model the fracture process zone. By performing the tension tests under monotonic and cyclic loading conditions, the development of the damage within the process zone can be identified, which could represent the feature of the cohesive law.

3.2 Material and C(T) loading tests

S460 steel is chosen for the current investigation. Its chemical composition is given in Tab. 3.1. The mechanical properties are obtained through uniaxial tests which are performed on smooth round tensile bars with the diameter of 6 mm, as shown in Fig. 3.1(a). Tensile tests are carried out with the strain rate $10^{-4}/s$ at room temperature in MTS 809 servo hydraulic dynamic tension-torsion testing machine. The gauge length of the extensometer used is 12 mm. The monotonic stress-strain curve for S460 steel is shown in Fig. 3.1(b). The mechanical properties are summarized as follows: initial yield strength $\sigma_y = 460$ MPa, ultimate strength $\sigma_u = 580$ MPa, reduction of area $\varphi = 77\%$, elongation $\varepsilon_f = 48\%$, Young's modulus $E = 208$ GPa and Poisson's ratio $\nu = 0.3$.

Table 3.1: Chemical composition of S460

C	Si	Mn	P	S	Cr	Ni	Fe
0.18	0.45	1.48	0.03	0.03	0.12	8.1	bal.

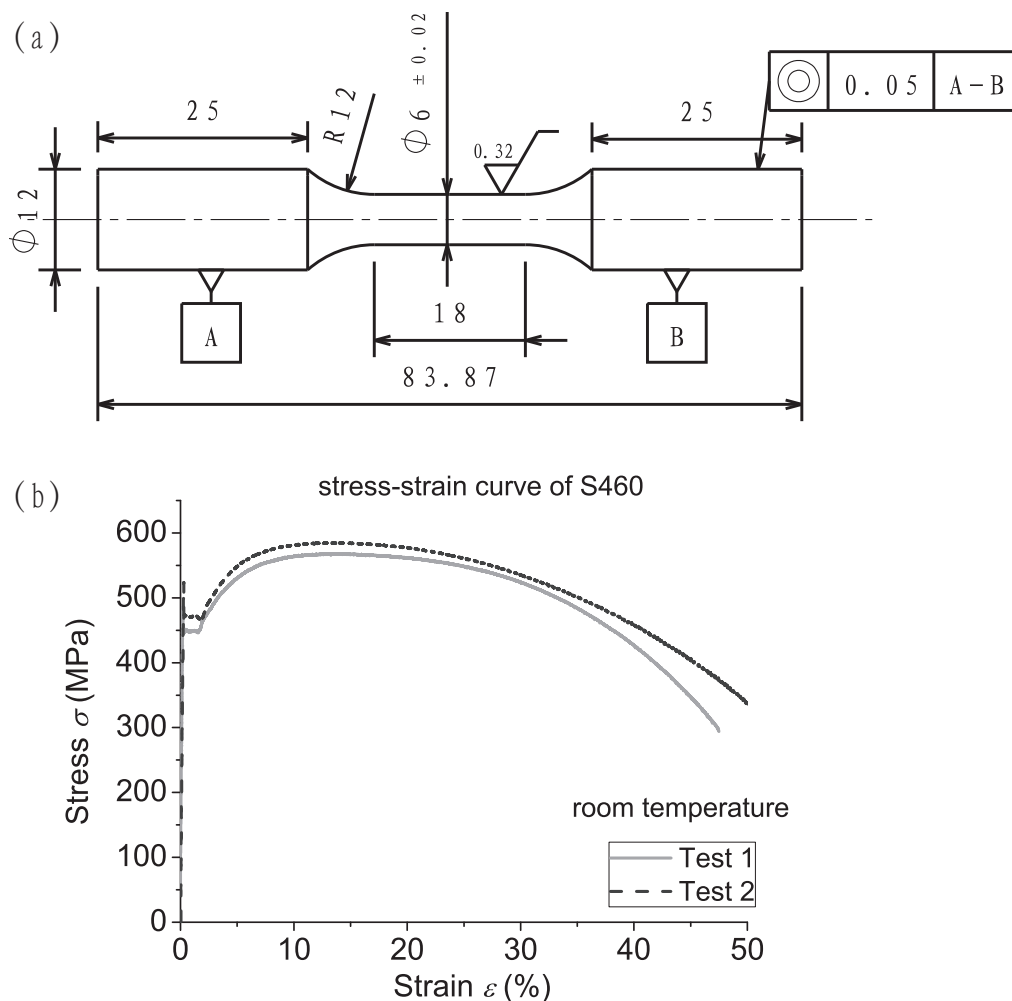


Figure 3.1: (a) Smooth round tensile bar for the uniaxial test; (b) Monotonic stress-strain curve for S460 steel.

The mode I fatigue crack tests are carried out by using C(T) specimens. The C(T) specimens are fabricated according to ASTM standard E647 [75]. The dimensions of the specimen are illustrated in Fig. 3.2(a). The thickness of C(T) specimens for fatigue crack tests is $B=12.5$ mm with a width of $W=50$ mm. All fatigue pre-cracks of specimens are generated under the constant mode I loading using a high frequency testing machine at the loading frequency of approximate 90 Hz. The principles during the process of the fatigue pre-cracking follow ASTM standard E647 [75]. The fatigue pre-crack length Δa shall not be less than $0.1B$ or 1 mm, whichever is greater. The final stress intensity factor K_{\max} corresponding to $a + \Delta a$ should not exceed the initial value of K_{\max} for the fatigue crack growth test. The stress intensity factor of the C(T) specimen could be calculated based on the following equation,

$$K = \frac{F}{B\sqrt{W}} \frac{(2 + \alpha)}{(1 - \alpha)^{3/2}} [0.886 + 4.64\alpha - 13.32\alpha^2 + 14.72\alpha^3 - 5.6\alpha^4], \quad (3.1)$$

where F is the applied force, B is the specimen thickness, W is specimen width, $\alpha = a/W$ and a is the crack length. Eq. (3.1) is valid for $\alpha \geq 0.2$. The fatigue pre-cracking is carried out with the initial $\Delta K = 23.5 \text{ MPa}\sqrt{\text{m}}$ at the loading ratio $R = 0.1$.

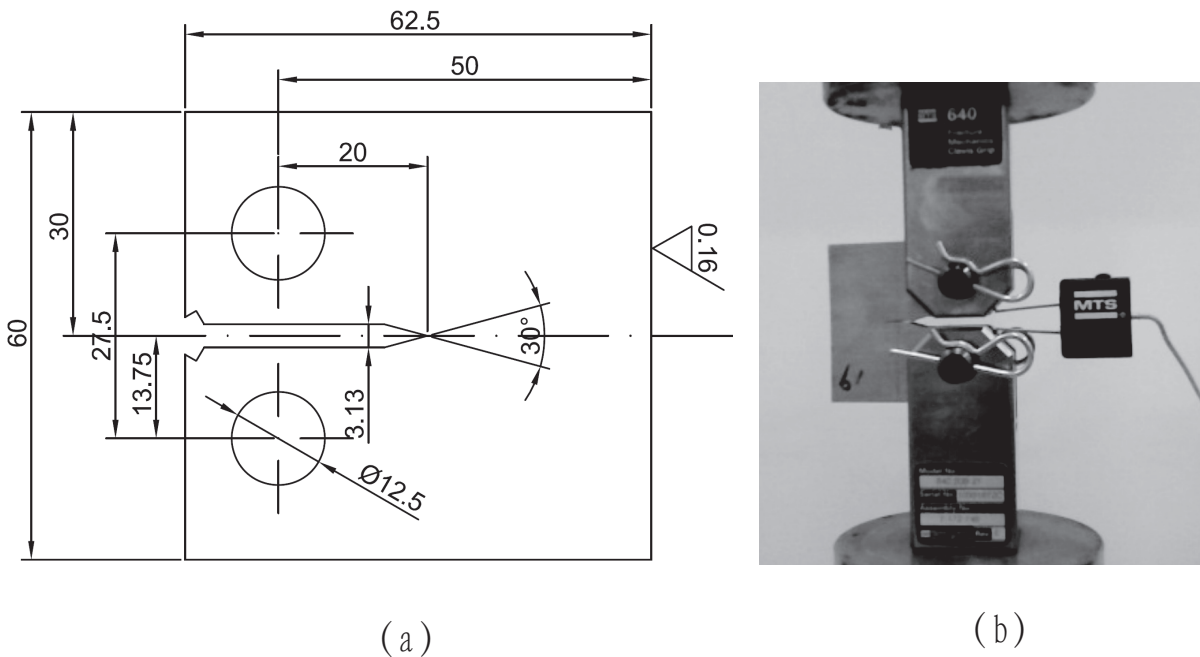


Figure 3.2: (a) The dimensions of C(T) specimens. (b) Fatigue crack growth rate measurement of a C(T) specimen by using the COD method in MTS 809 servo-hydraulic testing system.

The fracture and fatigue tests are carried out by a MTS 809 servo-hydraulic testing system which consists of load frame, load cell, grips, hydraulic actuator and digital controller etc. The load path of the machine should be calibrated such that each load components should lie on the center line of the load path system. The compliance method (COD method) is used for measuring the crack length which is based on the dependence between the compliance and the crack length of the specimen, as shown in Fig. 3.2 (b).

All fatigue tests are performed at room temperature with the constant force spectrum with sine waveform at the frequency of 10 Hz. The fatigue crack growth rate is measured

by using the compliance method at the intermediate loading level for C(T) specimens. The MTS 632.02 clip-on displacement gage is adopted to measure the COD of specimens. Fatigue crack growth are conducted under different loading ratios, $R=0.0, 0.1, 0.4$ and 0.7 . With growing the crack length, the stress intensity factor K increases under the constant force amplitude. The normalized gradient of K is defined as [75],

$$C = \frac{1}{K} \frac{dK}{da} = \frac{1}{K_{\max}} \frac{dK_{\max}}{da} = \frac{1}{\Delta K} \frac{d\Delta K}{da}. \quad (3.2)$$

This expression is valid for a constant loading ratio. In K -increasing tests, the gradient C should be positive and the value is set to 0.08 in all experiments. Fig. 3.3 shows the fatigue crack growth of C(T) specimens with various loading ratios. The experimental results of loading ratio $R = 0.1$ from the beach marking method are also plotted. The beach marking method would be explained in detail in the following sections.

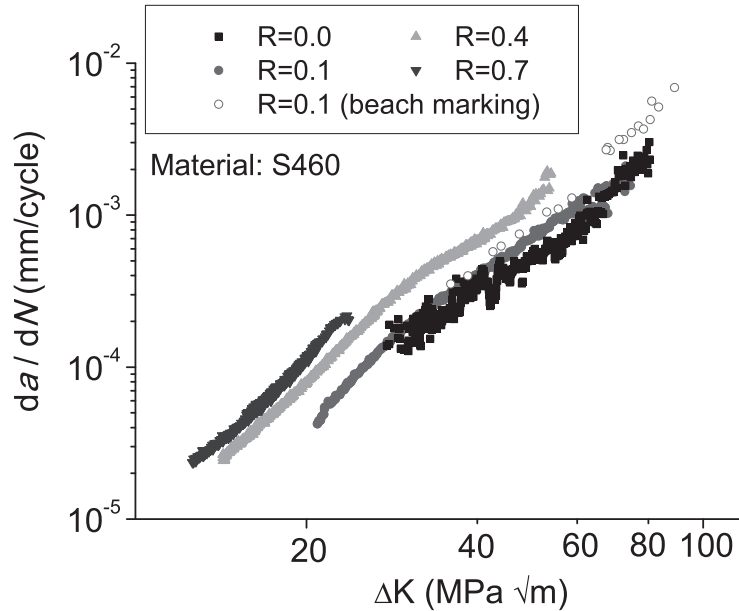


Figure 3.3: Experimental fatigue crack growth under various loading ratios for S460 steel.

The linear elastic or the SSY condition is required by using Eq. (3.1) or COD method. The crack tip plastic zone size r_p for plane strain conditions [3] can be estimated by

$$r_p = \frac{1}{6\pi} \left(\frac{K}{\sigma_y} \right)^2 \quad \text{for monotonic loading} \quad (3.3)$$

$$r_p = \frac{1}{24\pi} \left(\frac{\Delta K}{\sigma_y} \right)^2 \quad \text{for cyclic loading}$$

An approximate suggested restriction without significant violation of SSY principles is $8r_p \leq a$ [76]. The initial tensile stress of S460 has been determined as $\sigma_y = 460$ MPa. Accordingly, the experimental results shown in Fig. 3.3 are valid for the fatigue crack growth stages.

During engineering applications, the K -based model, e.g. Erdogan and Ratwani [27] is often used to correlate the experimental data. The model considers all three regimes by introducing the threshold value ΔK_{th} and the fracture toughness K_c as,

$$\frac{da}{dN} = \frac{C(\Delta K - \Delta K_{th})^m}{(1 - R)K_c - \Delta K}. \quad (3.4)$$

In the present study, the fracture toughness K_c is estimated through the monotonic loading tests. The C(T) specimens are the same as those used in the fatigue tests. Specimens are firstly pre-cracked until the initial crack length around 30 mm. The initial crack length is measured by using the COD method. During the monotonic loading, the corresponding critical force for the crack initiation is recorded. Then, the stress intensity is calculated according to Eq. (3.1) and this value is taken as K_c . In fact, due to the high ductility of S460, the geometrical dimensions of C(T) specimen for present study dissatisfy the ASTM standards E399 and E1820 [77, 78]. Accordingly, the value obtained is only a rough estimation, which is applied only for fitting the Erdogan model. The estimated K_c for present study is approximately $120 \text{ MPa}\sqrt{\text{m}}$.

The threshold value ΔK_{th} is determined empirically. According to Forman et al. [79], for present study, ΔK_{th} is taken $7.5 \text{ MPa}\sqrt{\text{m}}$.

In Erdogan model, two calibrated parameters C and m are required. The algorithms proposed by Li [80] are adopted for the fitting. Using Log function on Eq. 3.4 is given by,

$$\lg\left(\frac{da}{dN}\right) + \lg[(1 - R)K_c - \Delta K] = m\lg(\Delta K - \Delta K_{th}) + \lg C. \quad (3.5)$$

Define that

$$\begin{aligned} X_i &= \lg(\Delta K - \Delta K_{th}), \\ Y_i &= \lg\left(\frac{da}{dN}\right) + \lg[(1 - R)K_c - \Delta K], \\ u &= m, \\ w &= \lg C, \end{aligned} \quad (3.6)$$

consequently the total square deviation I and the systems of equations for parameters u and m are,

$$I = \sum_{i=1}^n (uX_i + w - Y_i)^2, \quad (3.7)$$

$$\begin{cases} u \sum_{i=1}^n X_i^2 + w \sum_{i=1}^n X_i = \sum_{i=1}^n (X_i Y_i) \\ u \sum_{i=1}^n X_i + w \sum_{i=1}^n 1 = \sum_{i=1}^n Y_i \end{cases}. \quad (3.8)$$

With the known values of ΔK_{th} and K_c , the calibrated parameters C and m can be determined by solving Eq. 3.8. The corresponding model parameters are $C = 10^{-4.38}$ and $m = 1.82$. The correlations of experimental data according to the fitting curves are shown in Fig. 3.4. For material S460, the curves can fit the experimental data for $R=0.0$, $R=0.1$

and $R=0.4$ successfully. However, for the experimental data $R=0.7$, the fitting curve shows significant deviation. With the loading ratio $R=0.7$, the fatigue crack growth rate da/dN presents only a small shift, which was also reported by Vormwald [81].

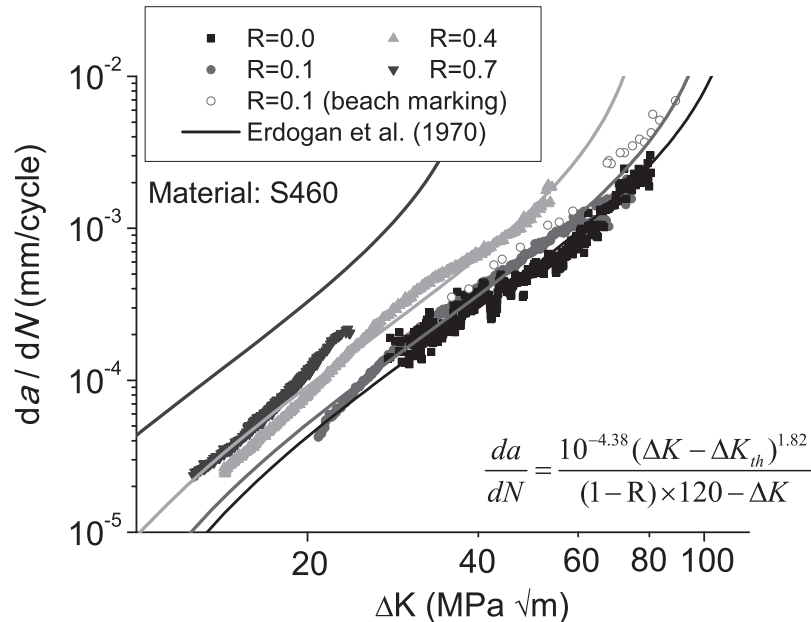


Figure 3.4: The fitting curves of experimental data of C(T) specimen through Erdogan model.

3.3 Surface fatigue crack tests under cyclic axial loading

In engineering, critical cracks exist mainly on surfaces of mechanical components. To predict fatigue crack growth life, characterization and verification of a surface crack through the conventional fracture mechanics specimen, such as C(T) specimen, are of interesting. From fracture analysis it is known that the stress field in a 3D surface crack differs from the conventional plane strain tip field. The stress intensity factor (SIF) depends additionally on crack front curvature, crack edge to free surface and structure configuration. Especially, SIF may vary non-proportionally with crack growth. Predictability and accuracy of the fracture mechanics to 3D surface crack are still interesting issue for many mechanical parts under complex loading conditions.

3.3.1 Rod specimen with a straight-front surface crack

The straight-fronted surface crack is often used in experiments due to easy manufacturing. Such a crack can be considered as an extreme shape of either the part-circle or part-elliptic surface crack. The outer geometry configuration of a specimen is shown in Fig. 3.5. The diameter D is 12 mm and the length L is 25 mm in the test section. Using a linear cutting machine, straight-edge surface cracks are cut with the initial flaw depths $a_0 = 1.5$ mm.

The geometry parameters in the test section of a specimen and those to describe the crack growing process are shown in Fig. 3.6. An equivalent elliptical-arc edge flaw is used to replace the actual part-through crack after some steps of crack growth. In the figure,

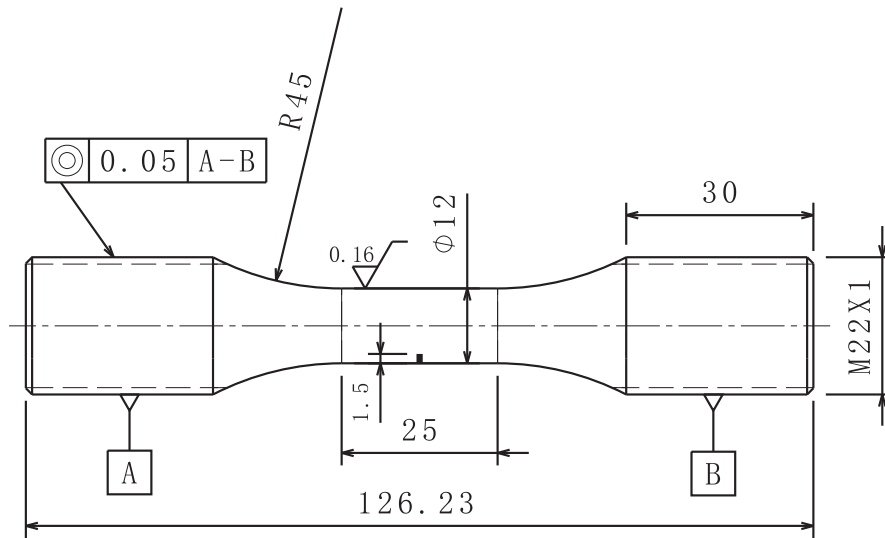


Figure 3.5: Details of the rod specimen with a straight-front surface crack.

a denotes the current crack depth. The crack front may be approximated by an elliptical curve with semi-minor axes a and semi-major axes b . Noted that the length b of the semi-major axes of the assumed ellipse is only an estimated value. For a certain crack depth, the crack shape can be controlled by an aspect ratio $\alpha = a/b$. A straight-front crack can be obtained in case of $\alpha = 0$ whereas $\alpha = 1$ represent a part-circular crack [82–86]. The intersection point C of the crack front with the surface can be measured by the axes of the elliptical curve a and b , and the diameter of the rod specimen, D . The distance from the point C to the axis of symmetry OY is m . The location of the points on the crack front can be described by the location ratio parameter x/m . The crack length in the surface direction can be obtained by the arc length s .

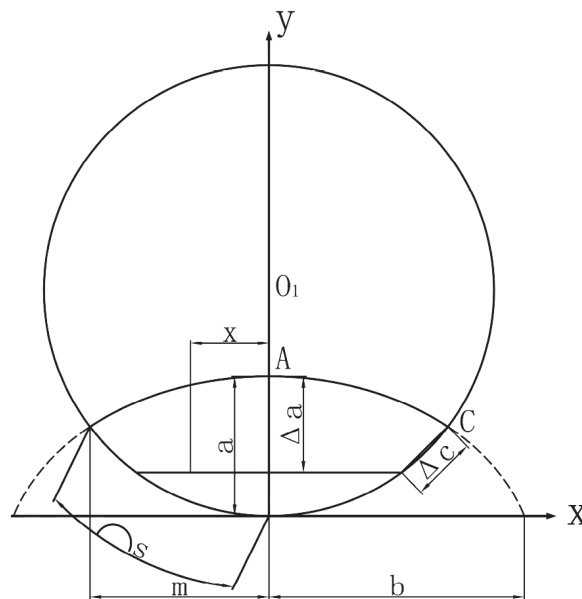


Figure 3.6: Illustration of surface crack geometry parameters.

3.3.2 Crack growth monitoring

All tests are performed on a MTS809 servo-hydraulic tension-torsion test machine and are carried out at 15 Hz at room temperature. For the simple cyclic tension tests, three different applied stress amplitudes with the same stress ratio $R = 0.1$ are used to study the effects of loading. The loading form is sinusoidal and the tests are performed in load control. To reduce the experimental error, two specimens are tested in the same condition and it is shown that the test results have good repeatability. The shape and depth growth of fatigue cracks are monitored using a zoom microscope and beach marking [85, 87].

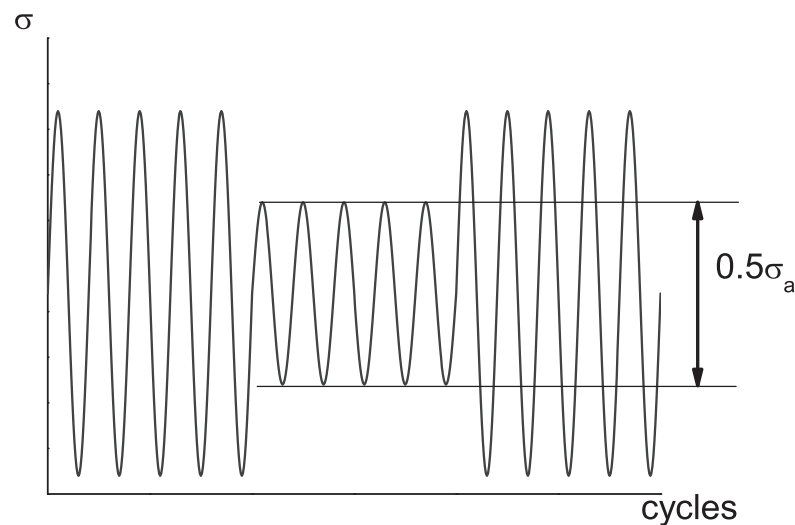


Figure 3.7: Loading curve and marked curve for the cyclic tension.

Instantaneous crack fronts are recorded by creating beach marking using a waveform that the mean load will keep constant but the load amplitude will reduce to 50% for several cycles. A sketch of the loading curve and marked curve is shown in Fig. 3.7. By comparing successive crack profiles obtained after loading for designated cycle numbers of each interval, the crack growth rate at different points on the crack front can be evaluated. The typical beach markers are shown in Fig. 3.8 (a). The markers on the cross-section of different specimens are clear, and it is possible to use these markers to fit elliptical-arc as shown in Fig. 3.8 (b). From the shape features of the specimen cross-sections, the relations of the crack depth a and surface crack arc length s can be measured using a comparison microscope.

3.3.3 Experiment results

The shape evolution of the straight-fronted surface cracks during the tests is determined using beach marks and the microscope measurements. The results are observed for several different tension amplitudes. An example of the shape developments is shown in Fig. 3.8 (a). The photograph is for the specimen with the initial crack depth of 1.5 mm and for cyclic tension loading of 24 kN. As is shown in the figure, crack propagation appears first

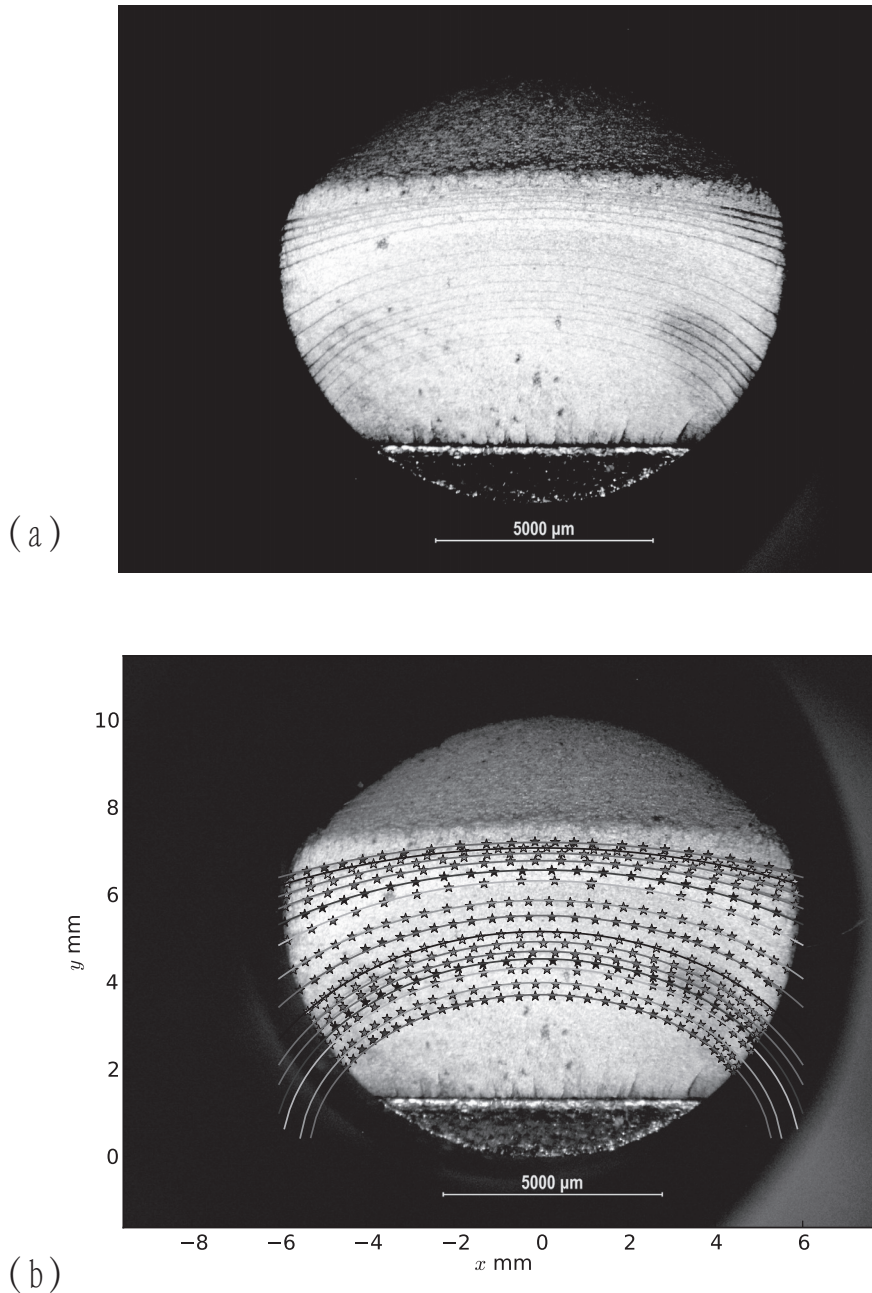


Figure 3.8: Fatigue crack growth process with initial crack depth 1.5 mm and 24 kN cyclic tension loading. (a) Photograph of the cross-section of a specimen with beach markers. (b) The sketch of the elliptical-arc fitting corresponding to each beach marker.

in the deepest point of the cylinder bar. At the beginning of crack growth, the growth rate in the central point of the crack front is faster than that at the intersection with the external surface. Consequently, a straight-fronted crack tends to become curved, and the flaw aspect ratio a/b increases. When a/b gets to some value, the deepest point and the external surface points on the crack front have almost the same stress intensity factor (SIF). After that, the crack growth rate at the intersection of the crack with the external surface is higher than that at the deepest point and the curve tends to flatten. Detailed calculations of the SIF for the surface crack are presented in following sections.

The developments of crack growth in depth direction a/D and surface direction s/D under three different applied stress amplitudes are summarized in Fig. 3.9. The results are also compared with the results from [86]. It is shown that the effect of the tension loading amplitudes on the shape evolution is not large, the sketch of the crack growth curves may be collected from several tested specimens. For the specimens with different notch depth, the crack propagation paths differ for different initial flaws, but they tend to converge to the same configuration. For the material S45 (hollow dots), the crack depth is equal to about 0.5. For the material S460 (solid dots), the crack depth is equal to about 0.55.

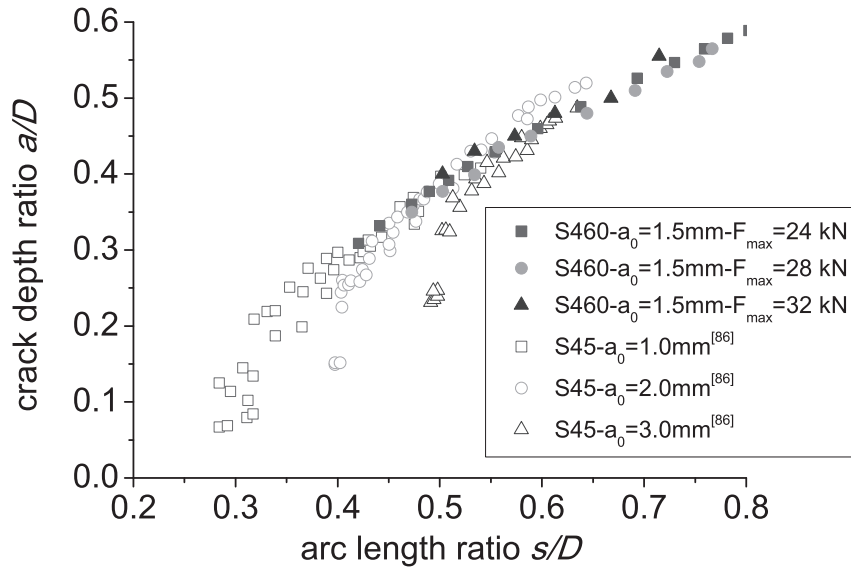


Figure 3.9: Relationship of crack growth in depth and surface directions.

3.3.4 Virtual crack closure technique (VCCT)

The virtual crack closure technique is widely applied in computing energy release rates based on results obtained from finite element analysis. The method is based on the crack closure integral [3] and mainly required two analysis steps. In the model the crack gets extended for a finite length prior to the second analysis. Consider a 2D crack problem with a thickness of t under mode I case, the crack is assumed to extend by Δa from a to $a + \Delta a$. The method provides the energy release rate G_I based on the work to be done by the nodal force $F_{y,i}(a)$ against the relative nodal point displacement $\Delta u_{y,i}(a + \Delta a)$ in order to close the crack by Δa [88, 89]. The nodal force $F_{y,i}(a)$ can be obtained from the first step analysis where the crack is closed. The nodal point displacement can be obtained from the second step analysis where the crack has been extended to its full length $a + \Delta a$, as illustrated in Fig. 3.10,

$$\Delta E_y = \frac{1}{2} F_{y,i}(a) \cdot \Delta u_{y,i}(a + \Delta a), \quad (3.9)$$

$$\Delta G_1^{2D} = -\frac{\Delta E_y}{t \cdot \Delta a}. \quad (3.10)$$

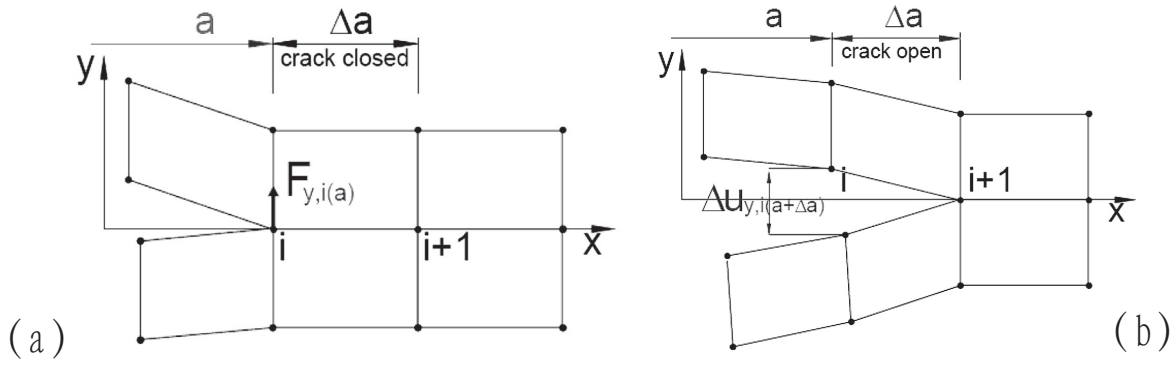


Figure 3.10: Illustration of two steps VCCT. (a) First step-crack closed. (b) Second step-crack extend.

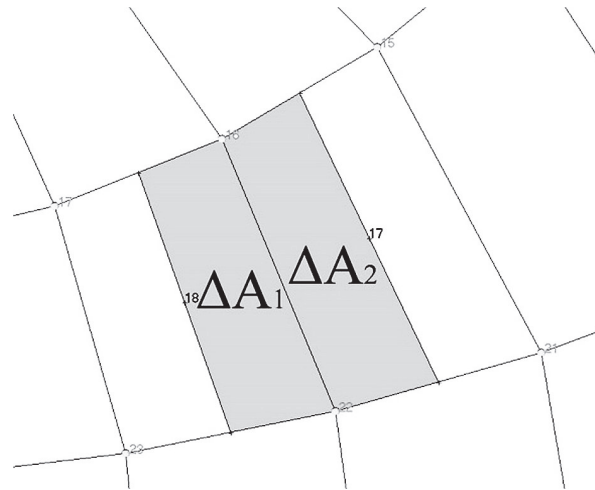


Figure 3.11: Cross section of a 3D finite element model of arbitrary crack shape.

Equation (3.10) has been derived under the assumption that the crack front is straight. For an arbitrary shaped front the mode definition constantly changes along the counter. A local crack tip coordinate system is necessary to be defined at each nodal point along the front [89]. Fig. 3.11 denotes crack front cross section of a 3D solid element model. ΔA_1 and ΔA_2 represent the areas of contributing element surfaces of point i . Assume a 3D model under mode I case and the remote tension in z direction, an expression of energy release rate G_I yields:

$$\Delta E_z = \frac{1}{2} F_{z,i}(a) \cdot \Delta u_{z,i}(a + \Delta a), \quad (3.11)$$

$$\Delta G_I^{3D} = -\frac{\Delta E_z}{\Delta A_1 + \Delta A_2}. \quad (3.12)$$

In linear elastic fracture mechanics (LEFM), the conversion equation of energy release rate G to stress intensity factor K can be expressed as:

$$K = \sqrt{G \cdot E'}, \quad (3.13)$$

where $E' = E$ for plane stress conation and $E' = E/1 - \nu^2$ for plane strain conation. In above equations, E denotes the Young's modulus and ν denotes the Poisson's ratio.

3.3.5 Stress intensity factor (SIF) analysis of surface crack

The geometry parameters in the test section of a rod specimen and those to describe the crack growing process have been shown in Fig. 3.6. An equivalent elliptical arc curve is used to indicate the actual crack after certain number cycles of crack growth. To obtain the SIF distribution along the actual crack, 3D FE model which is in compliance with the crack configurations is generated with symmetric boundary conditions applied, as shown in Fig. 3.12.

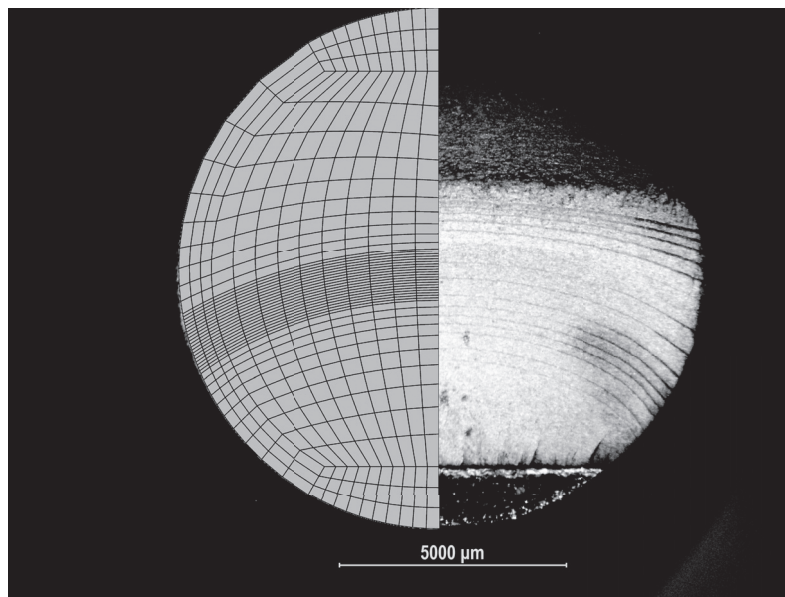


Figure 3.12: Element meshes of the cross section in compliance with the crack configurations.

In the FE model, the equivalent elliptical arc curve is dispersed into 13 elements. The element length near the free surface is about 0.25 mm and the element length near the middle plane is about 0.45 mm. In the crack propagation direction, the smallest element length around the crack is about 0.05 mm. In the vertical direction, the element height of the first layer is 0.1 mm. Algorithms of the VCCT for different element types may refer to the work of Richard [90] and Krueger [89]. It is general accepted that there is a small dependence on element size through the VCCT.

According to the geometrical dimensions defined, a simplified model of SIF K_I for surface crack under fatigue tension loading can be expressed as:

$$K_I = F \cdot \sigma \sqrt{\pi a}, \quad (3.14)$$

where σ is the tension stress and a is the crack depth at internal deepest point A . F is considered as a geometric factor. For one point on the crack front, F is a function of the elliptic semi axes a and b and the location ratio x/m .

To verify the computation of surface crack analysis, the geometry factor F is plotted as a function of the crack depth a/D , as shown in Fig. 3.13. Present results confirm

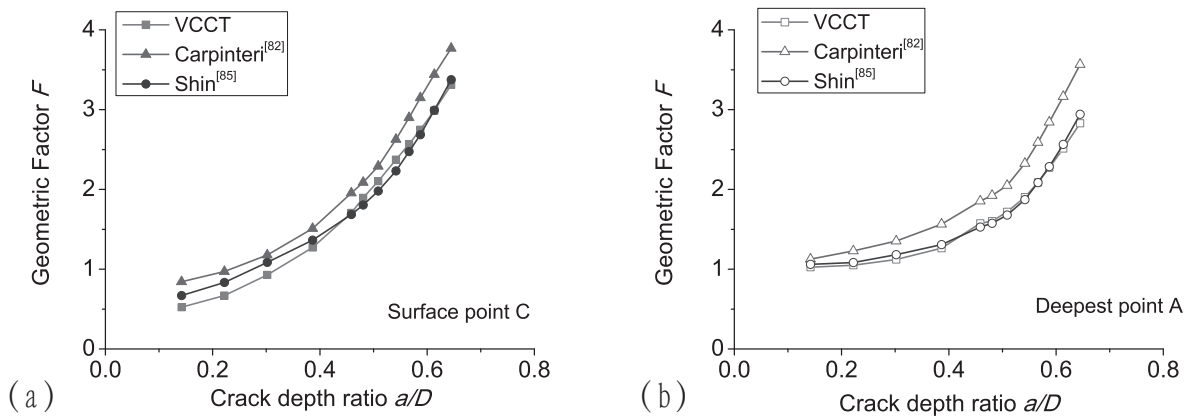


Figure 3.13: Results comparison of the geometry factor F with the crack growth for the surface point C and deepest point A .

that VCCT provides reliable results at the surface point as well as at the deepest point in comparing with [82, 85]. In general, the FE solution by Carpinteri [82] seems higher, whereas the FE results from Shin [85] are nearly coincident with the results of VCCT.

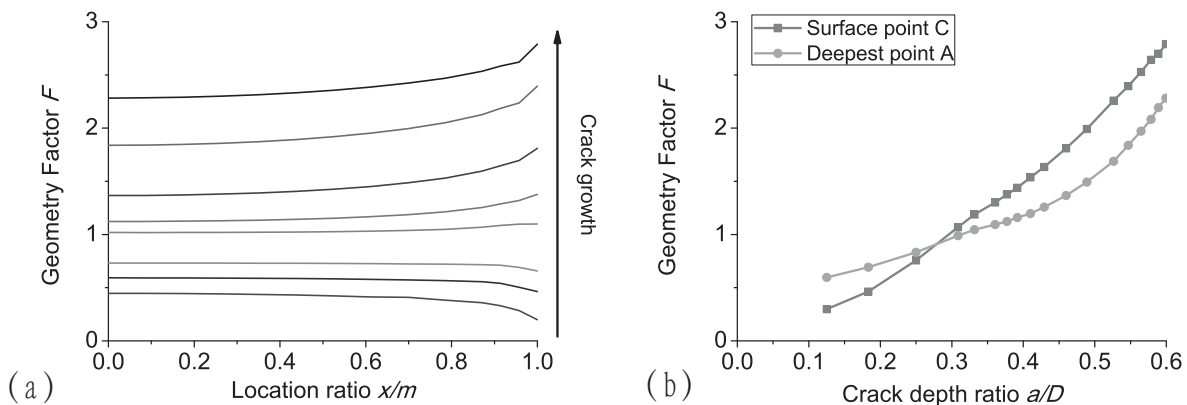


Figure 3.14: (a) Geometry factor F along the crack front with crack growth. (b) Development of the geometry factor F for the surface point C and deepest point A with the crack growth.

Figure 3.14(a) shows variations of F along the crack front during crack shape evolution in the rod specimen and Fig. 3.14(b) shows geometry factor F for Points A and C as a function of crack growth. For the initial notch, a straight crack front with the crack aspect ratio $\alpha = 0$ reveals the maximum SIF in the specimen middle and the SIF decreases with the distance x/m . It implies that the crack propagation starts at Point A and the crack front tends to become curved. With the crack developed α increases, the distribution of SIF reaches gradually constant in the whole crack front. In this region the crack front attains a uniform growth rate. Due to varying geometry of the circular rod, the stationary crack growth cannot maintain long. The SIF at the crack front near rod surface increases

and becomes maximal in the SIF distribution. It follows that the crack propagation near the rod surface is quicker than elsewhere. The curvature of the crack front decreases with crack growth. Variations of the geometry factor F agree with experimental observation, as shown in Fig. 3.8.

It should be noted that for the application of VCCT, the plastic zone ahead of the crack tip must be small enough so that the crack tip stress field can be expressed by the stress intensity factor. The stress intensity along the surface crack front is non-uniform and the plane stress conditions dominate near the free surface. Eq. (3.3) is valid for the plane strain condition, generally, the plane stress plastic zone size is usually taken as three times of the plane strain value [76]. Therefore, considering the crack length of the rod bar is smaller in comparing with the value of C(T) specimen, the restriction is violated of the final two cracks near the free surface, where $\Delta K \geq 80 \text{ MPa } \sqrt{\text{m}}$. However, VCCT is valid for the most surface crack growth stages.

A typical crack growth feature of the external surface point and the internal deepest point is clearly illustrated in Fig. 3.15. The crack growth behavior base line is obtained from C(T) specimens. It implies that at lower ΔK values, the crack growth at the internal point is faster than the surface point, as shown in Region I. With the crack developed and ΔK increases, crack growth behavior at two locations merge together, as shown in Region II. This phenomenon is also reported by Shin [85]. Experiments confirm that the fatigue crack growth in surface cracked specimens can be described by the crack growth behavior identified in conventional C(T) specimens. The predictions are rather precisely at lower ΔK . Deviation emerges with the loading range is getting higher. The mainly reason would be the plastic zone effect occurs with higher ΔK , due to the differences of the geometries and loading configurations of the surface cracked specimen and C(T) specimen, which leads to the deviation.

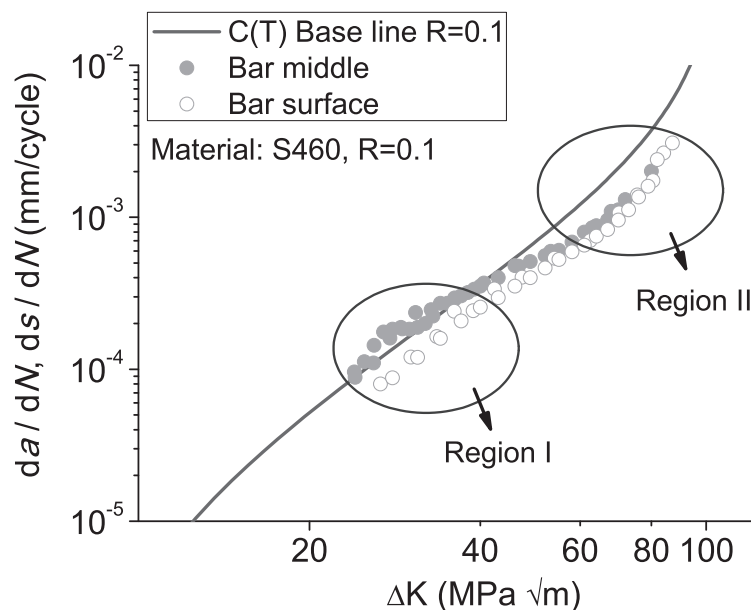


Figure 3.15: Crack growth behavior of rod specimen.

3.4 Fatigue crack propagation of C(T) specimens with different thicknesses

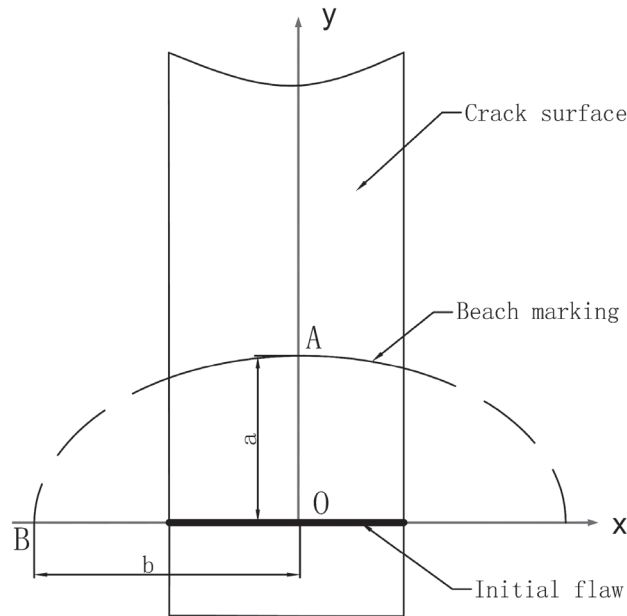


Figure 3.16: Illustration of the crack profile fitting with elliptical arc.

It is known that the plastic deformation at the tip of a crack inhibits the build-up of high stresses, and in turn governs the initiation and growth of cracks in structural materials. According to the conventional concept, the crack-tip plastic zone across the thickness of the specimen is given by the so called "dog-bone" model, which assumes a state of plane strain inside the specimen (centre) and a state of plane stress on the surface of the specimen. The crack growth is therefore effected by the in-plane and out-of-plane constraints mixed. In the present work, experiments are performed to examine the geometrical effect on fatigue crack growth.

C(T) specimens with the same geometrical dimension but different thicknesses are designed for the investigation. The geometrical dimension is shown in Fig. 3.2(a). Three different thicknesses, $B=12.5$ mm, $B=8$ mm and $B=4$ mm are carried out with the same width $W=50$ mm. As specified previously, the high frequency testing machine is used for the fatigue pre-cracking. Fatigue tests are performed in load control with the sinusoidal loading form at the frequency of 10 Hz. Two load amplitudes with the loading ratio $R = 0.1$ are carried out. Due to different thicknesses, for each loading level, the value of $\frac{F}{B\sqrt{W}}$ would keep constant for all specimens.

Beach marking method is used for tracing the crack profiles. The method has been introduced in detail. Since the fatigue pre-crack is generated at very low stress intensity level with high frequency, the whole specimen should experience pure mode I failure case. This way, the plastic deformation of the whole specimen can be neglected. Nevertheless for the fatigue crack growth tests, the dominance of plane stress conditions near the free surface would be obvious, the fatigue crack profiles of C(T) specimen would be no longer straight but curved with crack propagation. Accordingly, similar to the surface crack, an

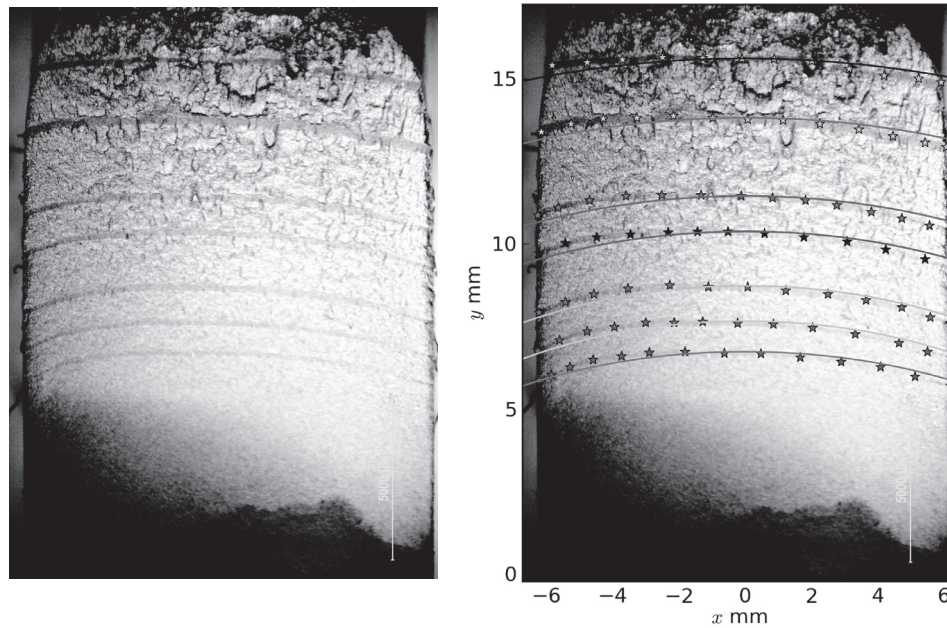


Figure 3.17: The fatigue crack surface of specimen $B=12.5$ mm, $F_{\max}=10$ kN.

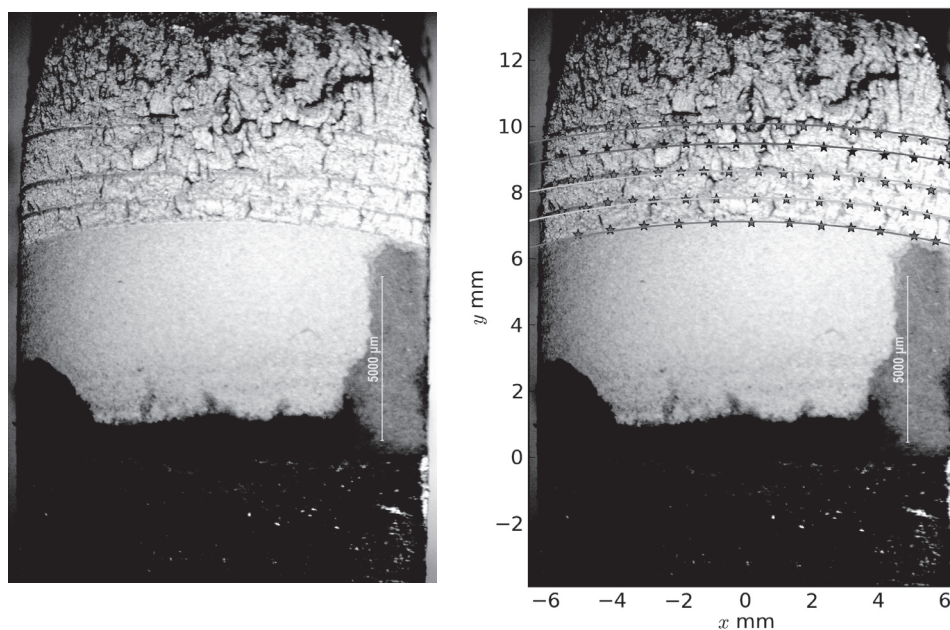


Figure 3.18: The fatigue crack surface of specimen $B=12.5$ mm, $F_{\max}=18.75$ kN.

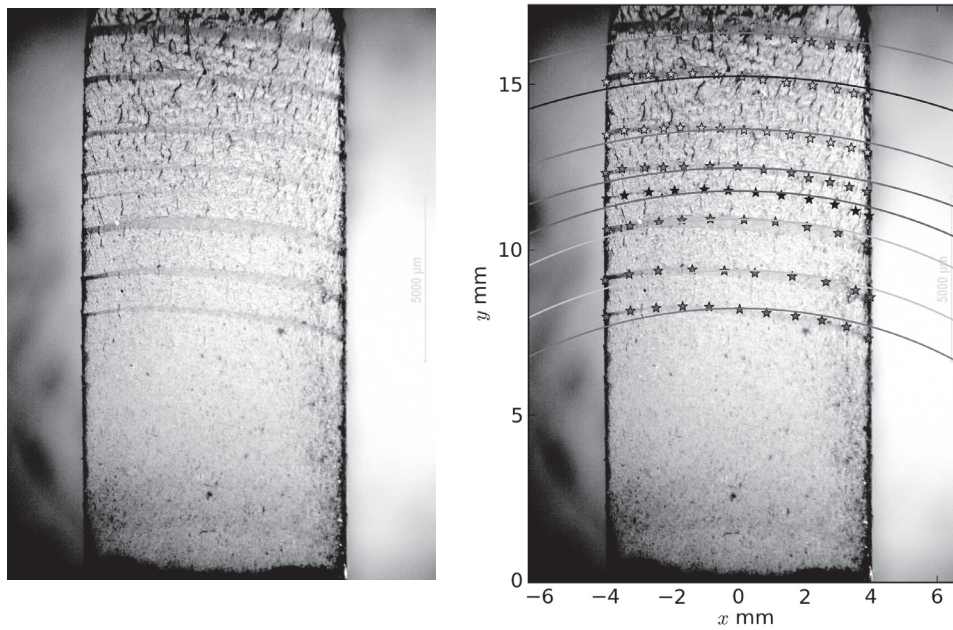


Figure 3.19: The fatigue crack surface of specimen $B=8.0$ mm, $F_{\max}=6.4$ kN.

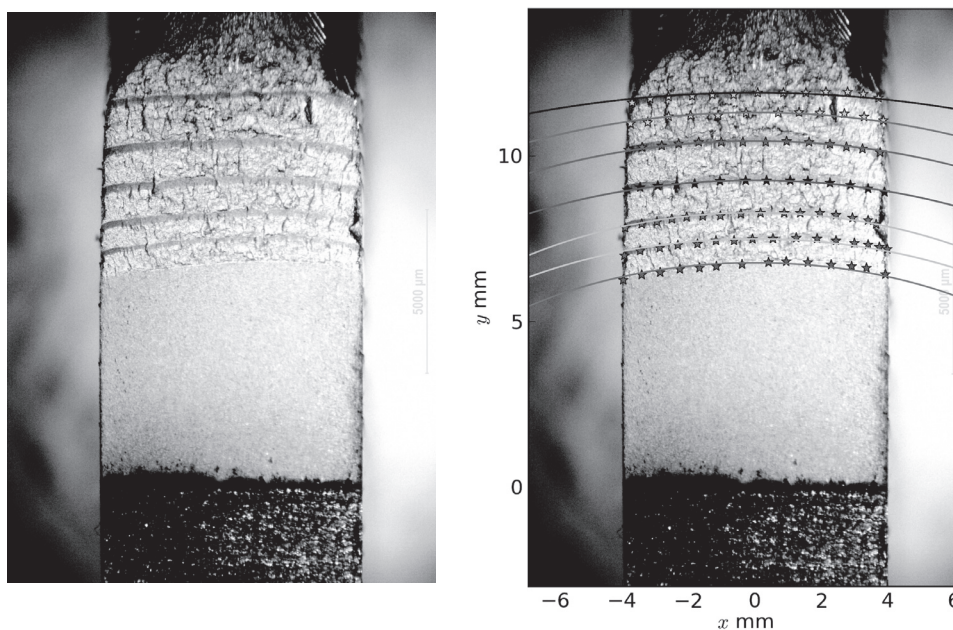


Figure 3.20: The fatigue crack surface of specimen $B=8.0$ mm, $F_{\max}=12$ kN.

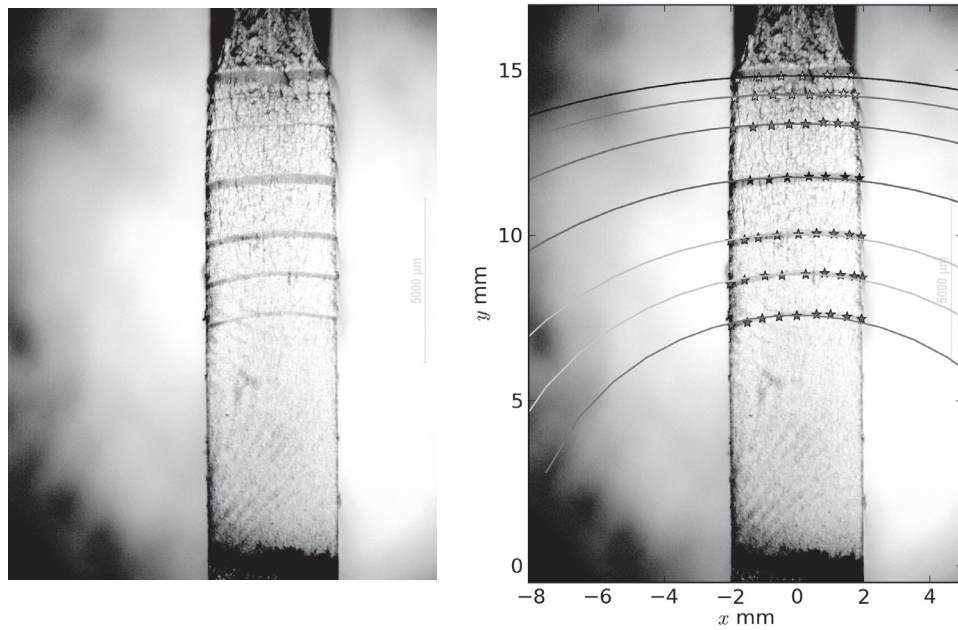


Figure 3.21: The fatigue crack surface of specimen $B=4.0$ mm, $F_{\max}=3.2$ kN.

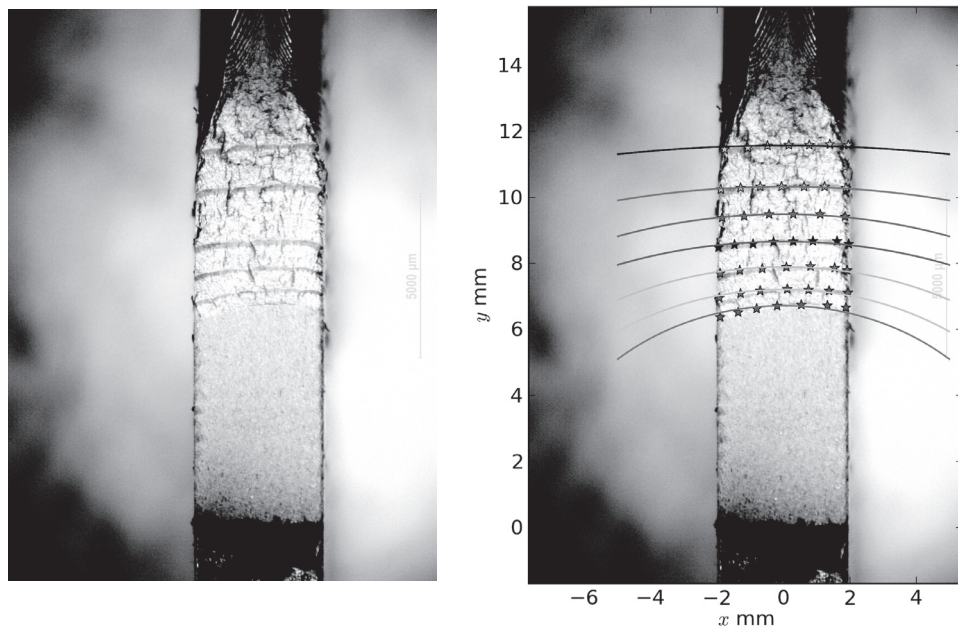


Figure 3.22: The fatigue crack surface of specimen $B=4.0$ mm, $F_{\max}=6.0$ kN.

equivalent elliptical-arc with semi-minor axes a and semi-major axes b , is used to fit the actual beach marking. A diagrammatic drawing is shown in Fig. 3.16. Obviously, a small value of a/b denotes a flat crack and a constant value of the curvatures should indicate a homogeneous crack growth. In this case, the crack growth rates at the free surface and the middle plane are the same. It is noted that the horizontal axis is along the initial flaw and the length of the initial flaw is 20 mm for all specimens.

The fatigue crack surfaces of specimens with different thicknesses are shown from Fig. 3.17 to Fig. 3.22. Note that due to the significant plastic deformation, the crack surfaces obtained from high loading level are very rough. Smooth crack surfaces are generated with low loading level, obvious rough area occurs only near the end of the crack surface. For each specimen, the elliptical-arc fitting lines corresponding to the beach markers are also illustrated. More detailed evolutions of the crack profiles with crack propagation for different thickness specimens are shown in Fig. 3.23. For all C(T) specimens, the stress intensity is calculated according to the middle crack length through Eq. (3.1).

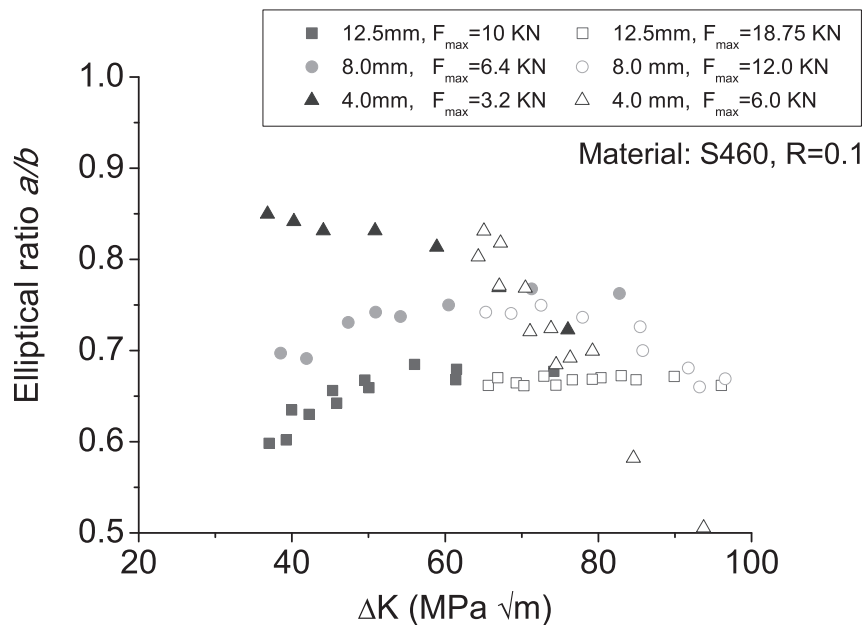


Figure 3.23: Comparisons of the crack profile variation with crack propagation for different thickness specimens.

The evolutions of the fatigue crack profiles show significant geometry dependent. For the thickest specimen of $B/W = 0.25$, the curvature of the crack profiles keeps nearly constant during stable crack propagation. This would imply that a nearly identical crack growth rate is performed at the free surface and at the middle plane. An important point should be noted that during elastoplastic fatigue crack propagation, area of the dominance of plane stress conditions should be contributed by the mode I and mode III failure simultaneously. Accordingly, the driven force near the free surface should be $K_I + K_{III}$. Although the plastic deformation accumulates near the free surface during fatigue crack growth, experimental results reveal a homogeneous crack growth. In addition, the experimental results also indicate that the failure mechanism near the free surface varies during crack growth. For the specimen of $B/W = 0.25$, at low stress intensity level which is approximately $K \leq 70$

$\text{MPa}\sqrt{\text{m}}$, no obvious plastic deformation occurs. In this case, it is reasonable to believe that the driven force of K_I should dominate near the free surface. At high stress intensity level where the crack growth rate is approaching the region III, severe plastic deformation occurs. Therefore, the driven force of K_{III} should be the major effect.

For the specimen of $B/W = 0.16$, the curvature of the crack profiles is larger. Obviously, with the same value of $\frac{F}{B\sqrt{W}}$, the percentage of the plane stress areas in the thinner specimen is larger in comparing with the value in the thicker specimen. The retardation near the free surface is therefore more obvious. The evolution of the crack profiles shows a nearly constant curvature until the stress intensity is approximately $80 \text{ MPa}\sqrt{\text{m}}$. With a further crack propagation, the crack profiles seem getting flatter. The failure mechanism for obtaining an identical crack growth rate at the free surface and the middle plane has been specified. However, for a thinner specimen, the plastic deformation during crack growth should be more serious. Eventually, the specimen would get fully-yielded at high stress intensity level. In this case, the crack growth rate at the middle plane is also slow down due to the effect of plastic deformation. It has been specified that with large plastic deformation, the crack propagation near the free surface should be mainly controlled by K_{III} , whereas the failure at the middle plane should be pure mode I case. This way, with a fully-yielded state, the crack growth rate at the free surface would be larger in comparing with the crack growth rate at the middle plane. Finally, the crack profiles would be getting flatter which leads to a smaller curvature.

For the thinnest specimen of $B/W = 0.08$, the largest curvature of the crack profiles is obtained due to the largest percentage of the plane stress areas in the specimen. Accordingly, experimental results denote that with crack propagation, the specimen gets fully-yielded when the stress intensity is approximately $60 \text{ MPa}\sqrt{\text{m}}$. As specified previously, with a further crack growth, the crack growth rate at the middle plane would be seriously retarded whereas the failure at the free surface would be mainly effected by the mode III case. Therefore, the curvature of the crack profiles would decrease continuously.

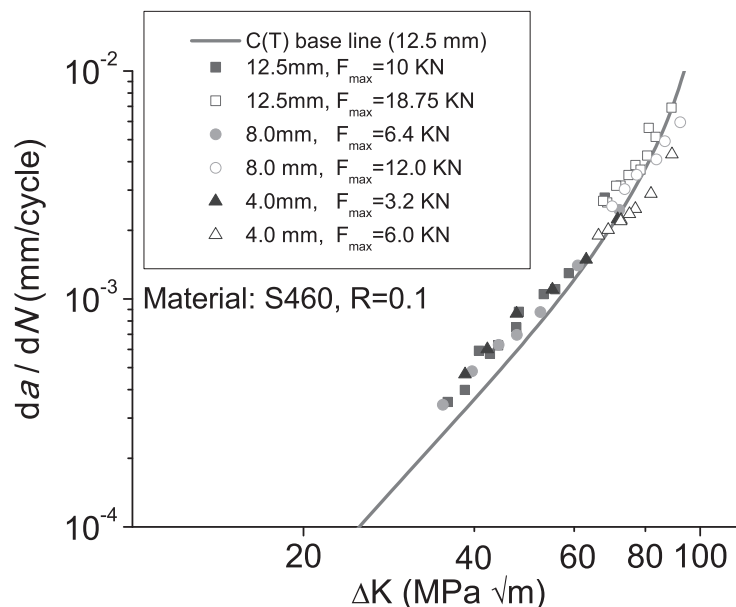


Figure 3.24: Comparison of the fatigue crack growth rate for different thickness specimens.

Detailed comparisons of the fatigue crack growth rates of different thickness specimens are shown in Fig. 3.24. The crack growth rates are measured according to the middle crack length. Note that before the thinner specimens getting fully-yielded, the crack growth rates of all specimens are coincident. Deviation emerges at high stress intensity level. Due to the effect of plastic deformation of the middle plane, the crack growth rate shows obviously retardation.

3.5 Cohesive law identification based on special CTS specimens

The cohesive model was introduced into finite element computations for simulating crack initiation and propagation along interfaces. Details of the cohesive constitutive relation, which is referred as the cohesive law, are particularly important. Various cohesive laws have been introduced as shown in Fig. 1.3. However, all known cohesive laws will be empirically assumed, which are derived by a hypothetical potential function. No effective method has been yet found to derive the cohesive law by experimental measurement.

In the present investigation, plate specimens with different notch heights are designed. Obviously, the notch area could represent the fracture process zone. Note that the cohesive zone model assumes the material response in the fracture process zone is represented by a cohesive law, which is describing the loss of load bearing capacity. Accordingly, the development of damage in the fracture process zone should characterize the feature of the cohesive law.

3.5.1 Specimen design and experimental procedures

AISI304 stainless steel is selected for the tests and its composition is given in Tab. 3.2. Before the manufacture of testing specimens, the material is annealed to eliminate the residual stress of the original material. The heat treatment method for the raw material is heating in a vacuum at 1100 °C for one hour following by quick cooling in air. The mechanical properties of AISI304 are obtained through uniaxial tests performed smooth round tensile bars as shown in Fig. 3.1(a). The mechanical properties are summarized as follows: initial yield strength $\sigma_y = 230$ MPa, ultimate strength $\sigma_u = 650$ MPa, elongation $\varepsilon_f = 100\%$, Young's modulus $E = 200$ GPa and Poisson's ratio $\nu = 0.3$.

Table 3.2: Chemical composition of AISI304

C	Si	Mn	P	S	Cr	Ni	Fe
0.04	0.41	1.05	0.035	0.03	17.1	8.1	bal.

The loading configuration of the plate specimen is similar to that of the compact-tension-shear (CTS) specimen. The specimens are designed with two different heights of the damage zone, $h=0.2$ mm and $h=2$ mm. The midsection area of both specimens is the same. To distinguish, the specimen with the thinner zone is named as *CTS crack* specimen whereas the specimen with the thicker zone is called *CTS notch* specimen. The dimensions of the specimens are shown in Fig. 3.25 and Fig. 3.26 respectively. The damage zone is

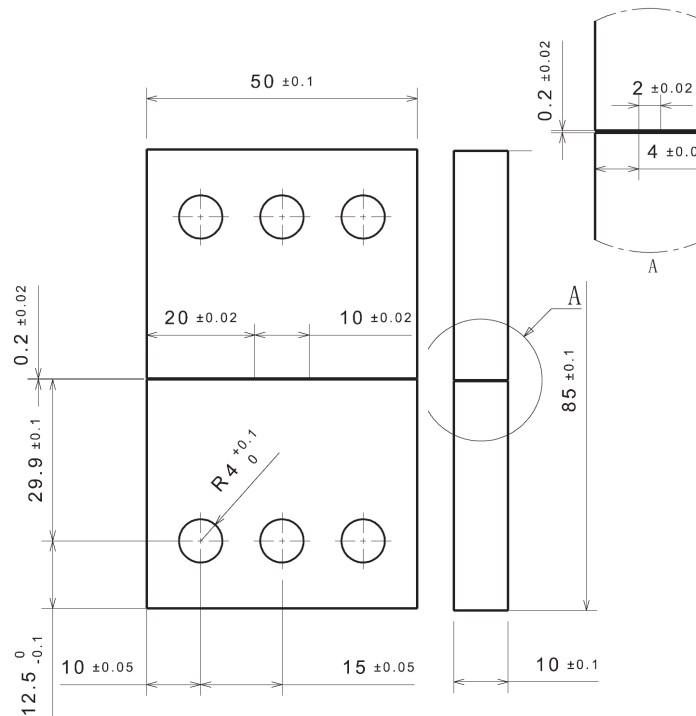


Figure 3.25: The dimensions of *CTS crack* specimen. The height of the damage zone is 0.2 mm with a thickness of 2 mm.

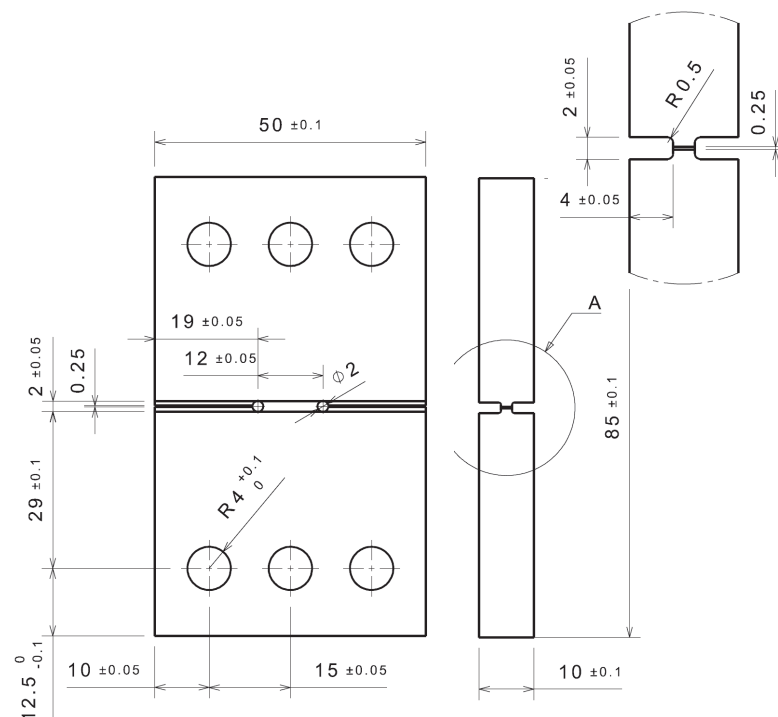


Figure 3.26: The dimensions of *CTS notch* specimen. The height of the damage zone is 2 mm with a thickness of 2 mm.

generated by using wire-electrode cutting and the effects of machining on the damage zone are neglected.

According to Lemaitre's suggestion [91], material damage can be expressed by diminishing of the elastic modulus

$$D = 1 - \frac{E(\varepsilon)}{E_0}, \quad (3.15)$$

where E_0 denotes the initial elasticity modulus of the material without damage and E depending on deformations stands for actual elasticity modulus. With developing material damage, the stiffness of the material decreases. In present investigation, the stiffness of the damage zone can be defined as the ratio of force F versus the opening displacement u_{open} , which can be written as

$$\psi = F/u_{\text{open}}. \quad (3.16)$$

Note that the opening displacement of the damage zone is measured at the position approximately 2.5 mm away from the edges of the zone. Due to symmetry, the positions should locate along the center line of the specimen. The value of the opening displacement is evaluated by the laser extensometer. In current work, only the damage from mode I case is investigated. Tension tests are performed to quantify the effect of damage evolution. The stiffness is determined from unloading which is controlled by the force to avoid compression. Under uniaxial tension condition, the stiffness is the slope of the elastic unloading line.

3.5.2 Monotonic loading test

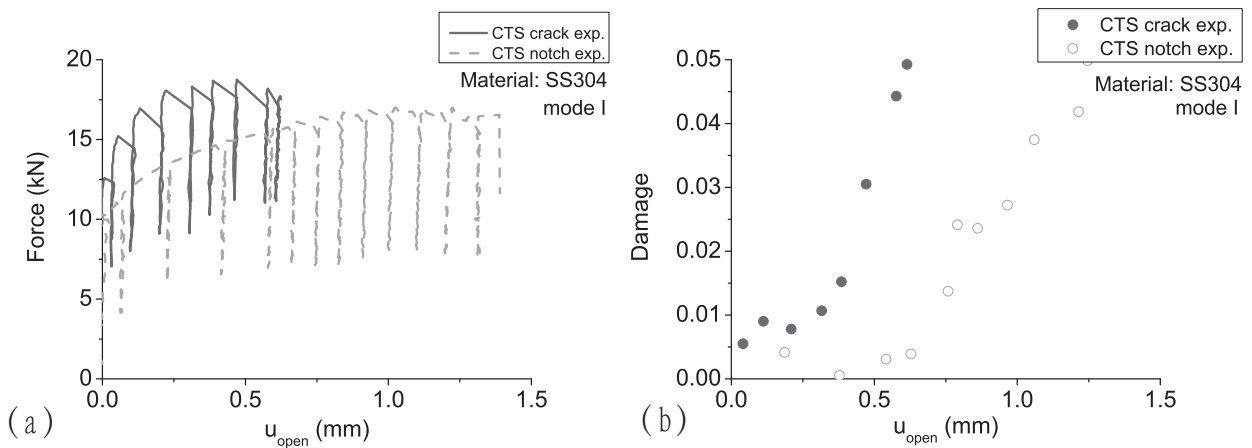


Figure 3.27: Loading-unloading for determining damage evolutions in mode I tension tests. (a) Force vs. opening displacement curves. (b) Evolutions of damage.

Under monotonic loading condition, the experiments are performed at room temperature on a MTS servo hydraulic universal testing machine and the cross head displacement is 0.05 mm/min for the tests to result in a quasi-static material response. Fig. 3.27(a) illustrates the loading-unloading force versus opening displacement curves of both specimens. The corresponding damage evolutions are shown in Fig. 3.27(b). Generally, the *CTS crack*

specimen responds higher resistance whereas the *CTS notch* specimen experiences larger deformation until final rupture. Due to the same midsection area of both specimens, the thinner zone would generate higher stress concentration which leads to higher reaction force, whereas the deformation within the thicker zone would be more homogeneous which requires larger deformation for the damage initiation. For both specimens, final failure occurs when the damage accumulation reaches approximately 5%.

To understand the deformation within the damage zone in detail, numerical calculations are performed. Three-dimensional elastic-plastic finite element computations are carried out and no damage model is applied in present analysis. Due to symmetry, only one-eighth of the geometry needs to be analysed. For all FE models, 20-noded quadratic elements (C3D20R) with 8 reduced integration points are used in the calculations. For both specimens, the critical displacement u_c , at which the final failure happens, will be recorded from the experiments. In FE computations, the models are displacement controlled and are applied to the corresponding displacement.

To make the numerical results can be compared, all results are obtained at the top of the damage zone. Fig. 3.28(a) shows the tensile displacement distributions of the free edge and the symmetric plane in thickness direction. Numerical results confirm that at the final failure, the deformation of *CTS notch* specimen is larger in comparing with the deformation of *CTS crack* specimen. Note that this result is agreed with the experimental observation as shown in Fig. 3.27(a). For both specimens, the deformation of the free edge is larger and more homogeneous than the deformation of the symmetric plane. At the symmetric plane, the largest deformation occurs at the free surface then decreases towards the middle plane. Numerical results indicate that both specimens should experience a same failure process. During monotonic loading, the damage should initiate at the free edge firstly, then the micro cracks/voids at the free surface would nucleate and finally, the macro cracks would extend from the free surface to the middle plane.

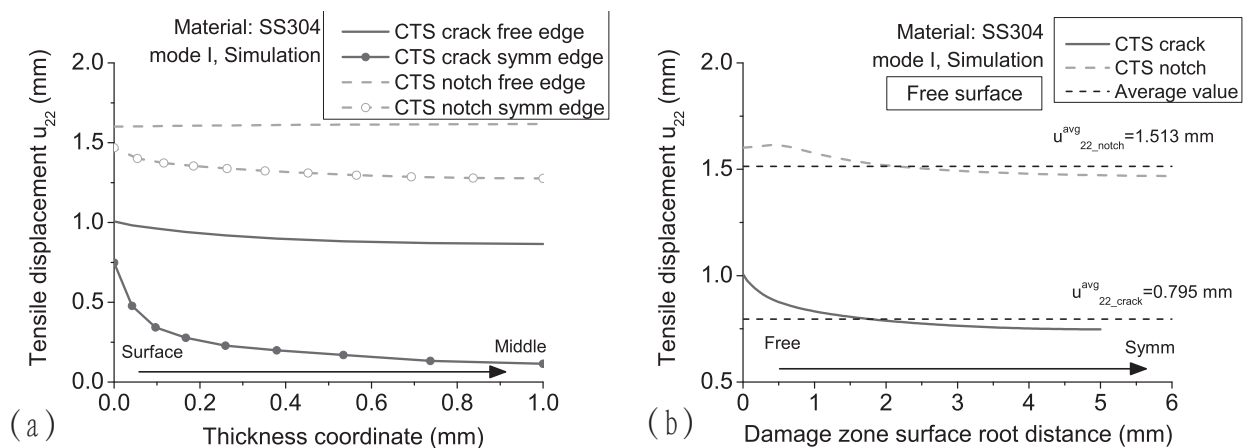


Figure 3.28: At the top of the damage zone, numerical results of the distributions of tensile displacement. (a) In thickness direction, at the free edge and the symmetric plane. (b) At the free surface, from the free edge to the symmetric plane.

In addition, Fig. 3.28(a) also indicates that the differences of the tensile displacement at the free surface are much smaller in comparing with the differences at the middle plane.

Accordingly, the deformation at the free surface should show no significant gradient. The tensile displacement distributions of the free surface are shown in Fig. 3.28(b). Since the damage initiates at the free surface, the average displacements of the free surface are calculated to represent the deformations of both damage zones respectively.

The computed stress-displacement curves are included in Fig. 3.29(a). Since the stable crack extension is not simulated in the analysis, the agreement of the computation and the experiment is good only up to the crack initiation point. The nominal stress σ^{nominal} is calculated according to the reaction force and the midsection area. Note that both specimens contain the same midsection area. As specified previously, due to stress concentration, the nominal stress obtained from *CTS crack* specimen should be higher.

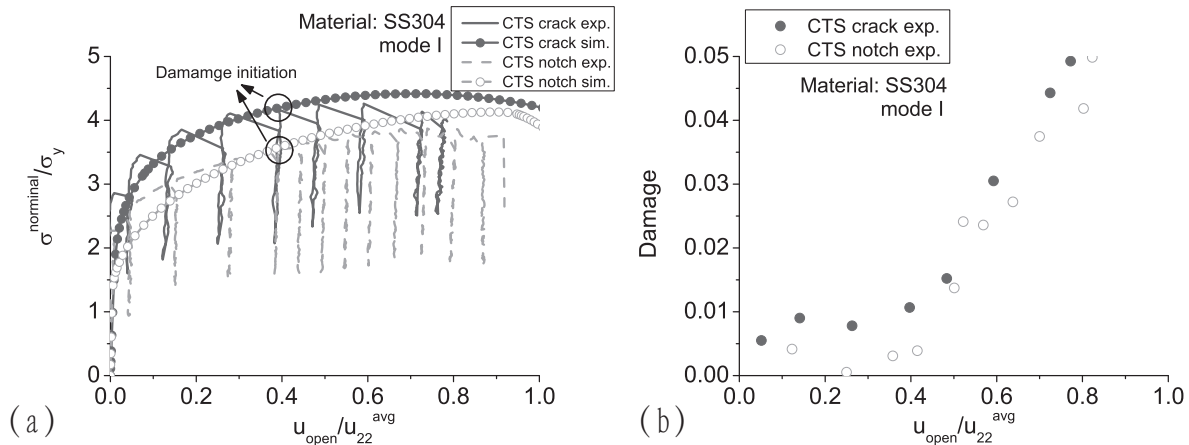


Figure 3.29: (a) Comparisons of the simulated and experimental dimensionless stress-displacement curves. (b) Evolutions of damage versus dimensionless displacement.

Should the opening displacements be divided by the deformations, a very similar damage process is shown in Fig. 3.29(b). Fig. 3.29(b) denotes that for both damage zones, damage initiates at a same value. This result should be significant which indicates that the damage evolution in the damage zone could be described uniquely, from the viewpoint of phenomenological damage mode, i.e. by a cohesive law. The damage initiation point can be considered where the maximum traction is achieved, after that, the load bearing capacity loses. In this case, the experimental result also confirms that the monotonic damage should be taken into account in constructing a cohesive law.

However, due to the too fast damage evolution of the material, the shape of the cohesive law could not be identified directly according to the present experimental results. To establish the characteristic features of the macroscopic response of the cohesive law, requires more detailed experimental investigations and taking into account the damage evolution in the FE computations, which is a motivation for the future work.

3.5.3 Cyclic loading test

Experiments are also performed to identify the damage evolution of the damage zone under cyclic loading condition. The specimen would be firstly monotonic loaded. After the maximum force is achieved, the specimen is further tested by the cyclic loading. The

frequency of the cyclic loading tests is 10 Hz. As specified in the monotonic loading test, the damage evolution is determined according to the decreasing of the stiffness of the damage zone.

Figure 3.29(a) shows the force versus opening displacement curve of *CTS notch* specimen. The cyclic loading is force controlled with the load ratio $R = 0.1$. No significant diminishing of the stiffness is obtained from the experiment. Fig. 3.29(b) shows the corresponding damage evolution with different maximum forces. Under force controlling, the damage evolution shows no accumulation during cyclic loading. It seems the final failure happens abruptly. The reason would be mainly due to the force controlling, the significant fast damage evolution of the material. For each loading cycle, the maximum force keeps

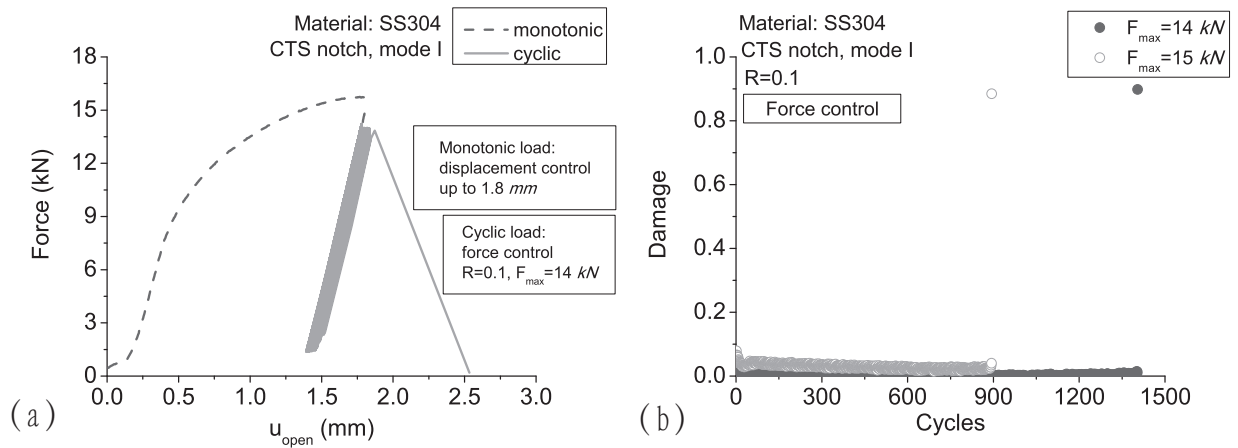


Figure 3.30: Experimental results of *CTS notch* specimen. (a) Force vs. opening displacement curve. The cyclic loading is force controlled with the load ratio $R = 0.1$. (b) The damage evolutions as functions of the loading cycles.

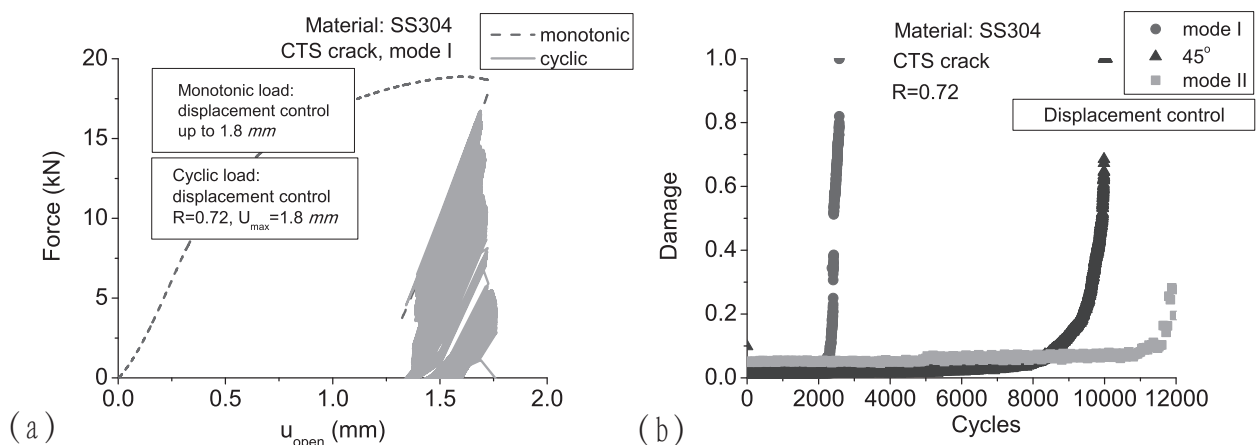


Figure 3.31: Experimental results of *CTS crack* specimen. (a) Force vs. opening displacement curve. The cyclic loading is displacement controlled with the load ratio $R = 0.72$. (b) The damage evolution as functions of the loading cycles in mode I, mode II and mix mode cases.

the the same. In this case, once the damage initiates, the force would not be allowed to decrease which leads to the damage increasing continuously. The final rupture would occur in one cycle and thus, the stiffness decreasing cannot be detected.

Displacement controlled cyclic loading tests are performed with *CTS crack* specimens. The tests are carried out with a high load ratio $R = 0.72$ to avoid the compression. Under displacement controlling, the maximum displacement would keep constant for each loading cycle. In this case, with the developing of the damage, the loading bearing capacity of the material decreases which leads to the decreasing of the force. This way, the stiffness of the damage zone is diminished and the evolution of damage can be identified. Force versus opening displacement curve of *CTS crack* specimen is shown in Fig. 3.31(a) and the corresponding damage evolution in different loading modes are illustrated in Fig. 3.31(b). Experimental results confirm that cyclic damage develops very slowly at the initial stage. Then the damage accelerates with cycles increasing, following with a rapid increasing until the final failure. Mix mode fatigue tests are also performed using the loading device proposed by Richard et al. [92]. Experimental results show that with the same loading condition, the damage accumulation in tensile loading case (mode I) is the fastest whereas the slowest damage accumulation occurs in shear loading case (mode II).

3.6 Summary

In the present work, the fatigue crack growth behavior of material S460 steel has been investigated systematically. The focus is primarily on the surface crack growth behavior and the geometrical effect on fatigue crack growth. The experimental results confirm the following conclusions:

- The stress intensity factor along the surface crack front non-uniformly varies with the crack growth. The crack growth rate is proportional to the stress intensity factor distribution in the three-dimensional cracked specimen. After the crack grows up over the crack front, the maximum of the stress intensity factor appears near the free surface of the tensile rod, so that the crack front curvature becomes smaller.
- The fatigue crack growth in surface cracked specimens can be described by the crack growth behavior identified in conventional C(T) specimen at low stress intensity level. With the crack propagation, due to the effect of plastic zone, the surface crack growth rate is slower in comparing with that of C(T) specimen.
- The fatigue crack profiles show obvious geometrical dependence. Larger curvature of the crack profiles is obtained from the thin specimen than that from the thick specimen. Furthermore, severe plastification occurs with the high rate of fatigue crack growth approaching Regime III. The thin specimen would be fully-yielded so that the crack growth rate at the middle plane shows obviously retardation.
- The damage evolution of the notch area of the CTS specimen has been investigated to find the experimental evidence to derive the cohesive law. Numerical results of the deformation of the notch area indicate that the damage initiates at the free edge firstly, then the macro cracks extend from the free surface to the middle plane. The damage evolution of the notch area manifests the macroscopic response of the



cohesive law. However, one cannot identify the cohesive law directly based on present experimental results. More detailed experimental results and the extension of the FE computations with proper damage models should be provided in the further research.

4 Stress-triaxiality-dependent cohesive zone model

4.1 Introduction

4.1.1 State of art of constraint dependent CZM

Studies have shown that fracture mechanisms in ductile metals are strongly influenced by the state of stress. To quantify this effect, a measure of the triaxiality of the stress-state is defined as the ratio between the hydrostatic stress and the effective stress: $\eta = \sigma_h / \sigma_e$.

In the development of cohesive zone model, the importance of triaxiality was first discussed a decade ago by Siegmund and Brocks [33]. In their study, a plane strain unit cell model with degradation of material properties represented through GTN model was subjected to a state of stress with a in-plane stress ratio, $\beta = \sigma_{11} / \sigma_{22}$. The stress ratio β varied between 0 and 1. Thus, the triaxiality parameter η under the assumption of incompressible plastic deformation could be calculated as $\eta = \frac{1+\beta}{\sqrt{3}(1-\beta)}$. During the loading process, the perpendicular elongation of the element, u_{cell} , showed a relationship with the applied stress, σ_{appl} . The authors directly used this relationship as the cohesive law. Numerical results from the GTN model showed that the cohesive parameters were strongly influenced by the stress triaxiality condition, as Fig. 4.1. Later, the similar idea was adopted by Scheider for the axisymmetric element [93]. Under plane strain condition, the approach was extended to include the effect of strain rates by Anvari et al. [34].

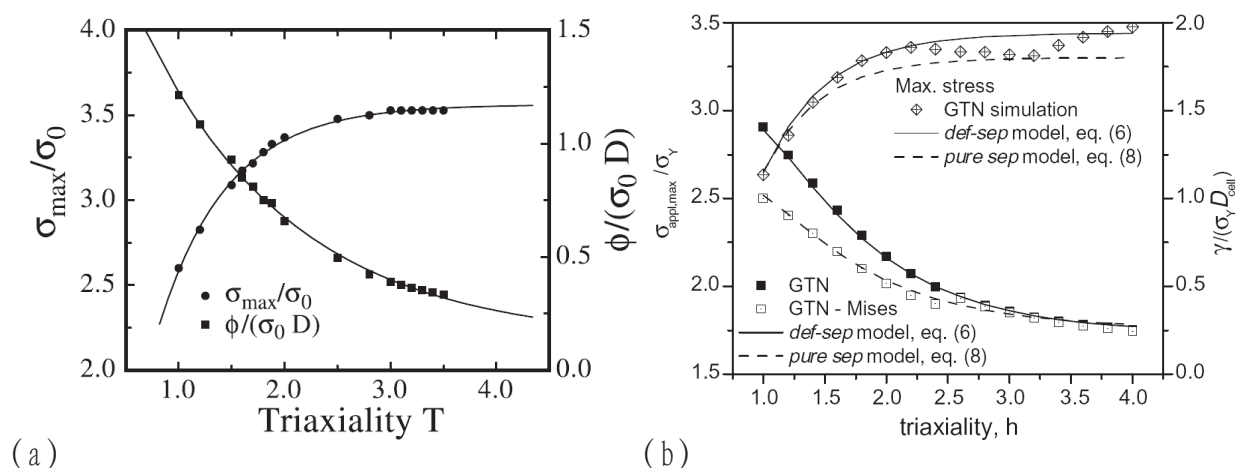


Figure 4.1: The dependence of cohesive parameters on the stress triaxiality from tension test for one cell element by using the GTN model. (a) In plane strain condition [33]. (b) In axisymmetric condition [93].

Accounting for the dominant effect of the stress-state on the ductile fracture process, Banerjee and Manivasagam [61] proposed a cohesive zone model for prediction of ductile fracture in different stress-states. The model described therein for plane strain mode I ductile fracture is formulated by using basic elastic-plastic constitutive equations combined with two stress-state independent new model parameters, which capture the triaxiality dependent failure strain. Later, Banerjee et al. developed procedures for estimation of model parameters of the high-ductility mild steel [94] as well as the low-ductility aluminum alloys [95].

It should be noted that, despite the methodologies of identifying the correlations of the stress triaxiality and cohesive parameters from GTN model as well as Banerjee model can reproduce the experimental data successfully, there still exist some inevitable limitations of both models: (i) Extending the stress-state dependent law to the scope of CZM still relies on the porous metal plasticity model for establishing the cohesive parameters, thereby requiring the determination of the GTN parameters first; (ii) There is a significant limit in discussions based on the GTN model, which considered damage cases only with high stress triaxiality [96]; (iii) Banerjee et al. [95] adopted a two-dimensional FE model which is predominantly composed of plane stress elements and a very narrow zone around the crack plane has plane strain elements, this kind of FE model may lead to unrealistic approximation in numerical computations.

Recently, Mahler and Aktaa [97] presented experiments and simulations of notched tensile specimens. The cohesive strength was obtained by fitting the whole stress vs. triaxiality information over specimen cross section and generating extrapolated values for higher triaxialities. The verification was shown on SEB and C(T) specimens by applying constant cohesive energy and the results were in very good agreement to the experimental data.

4.1.2 Motivation

Following the work of Yuan and Brocks [18], the systematic understanding of structural obstacle against the plastic deformation requires a detailed study of crack-tip plastic deformation in three-dimensional to distinguish between in-plane constraint and the out-of-plane constraint. In fact, in most of the cases the in-plane and out-of-plane constraints are mixed in such a way that their effects cannot be separated. Integration of the stress triaxiality into the cohesive zone model becomes a necessary step to apply it for quantifying out-of-plane constraint in three-dimensional cracks. Most published works were mainly on in-plane constraint effects, the formulation of the stress-triaxiality-dependent cohesive zone model (TCZM) and the identification of the cohesive parameters are still to be investigated.

In the present work, a new TCZM with constraint effects for three-dimensional cracks is introduced and implemented based on the technique discussed in [98]. The correlations of the stress triaxiality and cohesive parameters are discussed and identified based on experiments. Furthermore, the proposed TCZM is applied for three-dimensional crack propagation simulation.

4.2 Stress-triaxiality-dependent cohesive zone model

In cohesive zone modeling, material failure is described by a cohesive law. For a mode I crack, the cohesive model describes only normal failure, so that only the normal traction T and the separation δ on the separation surface are active. The focus of the cohesive zone model research is in formulation and identification of the cohesive law. For three-dimensional elastic-plastic cracks the cohesive law can generally be written as

$$T = T(\delta, \eta; T_0, \delta_0, \delta_u), \quad (4.1)$$

where δ denotes the normal separation of the cohesive zone. η is the current stress triaxiality. Generally the cohesive law is a function of the two variables, δ and η . Cohesive zone models contain the known parameters, such as the cohesive strength against material failure, T_0 , the separation for the hardening stage, δ_0 , the ultimate separation for failure, δ_u and so on. The shape of cohesive law taken for present study is shown in Fig. 5.1. The cohesive law's function and the cohesive energy are defined in Eq. (5.4) and Eq. (5.5) respectively. It is confirmed that the model above contains three model parameters, T_0 , δ_0 as well as δ_u , and can properly reproduce both monotonic and fatigue crack growth in metals under mode I and mixed-mode loading conditions [98].

To formulate a cohesive law depending on both δ and η explicitly, one can generalize Eq. (5.4) directly and assume the model parameters to be dependent on the stress triaxiality. From fracture mechanics it is known that the fracture energy increases with decreasing of the specimen thickness, that is, the cohesive energy should be a decreasing function of η . Furthermore, tensile test shows that the ultimate stress of material increases with the stress triaxiality [33, 61, 93], it implies the cohesive strength must be an increasing function of η . These experimental observations reveal that both cohesive energy and cohesive strength are affected by the constraint. Therefore, the cohesive parameters Γ_0 and T_0 in conventional CZM should be substituted by $\Gamma(\eta)$ and $T_{\max}(\eta)$ in TCZM respectively.

As Yuan and Li [54] pointed out, the initial cohesive stiffness has to be large enough, to avoid computational deficit and δ_0 seems to influence computational results hardly. In this sense δ_0 should be independent of η . For ductile metals generally $\delta_0 \ll \delta_u$, and the ultimate separation in the cohesive zone can be expressed in terms of the cohesive energy and the cohesive strength as

$$\delta_u(\eta) = 2 \left[\frac{\Gamma(\eta)}{T_{\max}(\eta)} - \delta_0(e - 2) \right] + \delta_0. \quad (4.2)$$

In summary both cohesive energy and cohesive strength depend on the stress triaxiality explicitly and have to be determined from experimental data.

In the present work, finite element computations are performed by using the general purpose commercial code ABAQUS. The cohesive model is implemented in ABAQUS by use of the cohesive element coupled with UMAT subroutine [71]. The stress triaxiality is computed accessing the solid elements via the UARM subroutine. In three-dimensional finite element computations the cohesive zone is introduced as an interface between two solids. The stress triaxiality at the interface are achieved from adjacent solid elements. The value of the stress triaxiality at the integration points are averaged and transferred to the nodes building the cohesive zone, as shown in Fig. 4.2. In ABAQUS, the field quantities can be transferred to the user defined subroutine only for the converged increment step,

that means, the cohesive parameters in the current step are determined based on the result of the previous increment step. The errors induced by this algorithm become negligible, if the time increment is small enough.

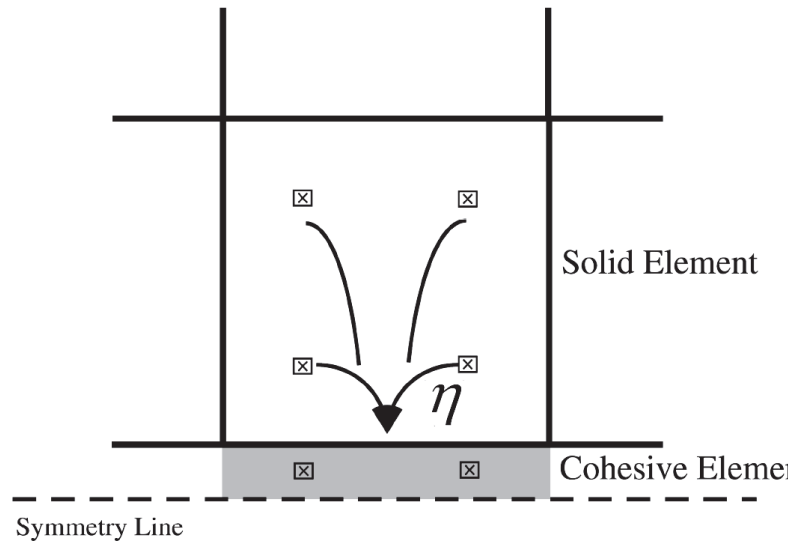


Figure 4.2: Schematic illustration of triaxiality value being transferred to a cohesive element from the adjacent continuum element [33].

4.3 Identification of the cohesive parameters

4.3.1 Material and specimens

To investigate the cohesive zone model presented in the previous section, a German construction steel S460 is chosen for experiments. Since the cohesive zone model is computational and cannot directly be measured, the experiments should provide evidences about material failure for identifying model parameters.

The mechanical properties are obtained through uniaxial tests which has been specified in Chapter 3. The initial tensile stress $\sigma_y=460$ MPa, the ultimate stress $\sigma_u=580$ MPa, Young's modulus $E=208$ GPa. The plastic behavior of the material is described by a power-law as

$$\varepsilon_t^p = \left(\frac{\sigma_t}{K} \right)^{\frac{1}{n}}, \quad (4.3)$$

with bulk modulus $K=866$ MPa and the strain hardening exponent $n=0.15$.

The dimensions of fracture mechanics specimens, the C(T) specimen and the cracked rod bar, have been illustrated in Fig. 3.2(a) and Fig. 3.5. Both specimens are pre-cracked to form an initially sharp crack tip. To obtain different triaxiality conditions at crack initiation, a series of C(T) specimens with different thicknesses was fabricated. The thickness of the smooth C(T) specimens varies from $B=2$ mm, 4 mm, 8 mm, 12.5 mm, 20 mm and 25 mm. The in-plane dimension is the same as the smooth C(T) specimen (Fig. 3.2(a)). Additionally, a side-grooved C(T) specimen was fabricated for studying fracture

process and diminishing effects of the specimen surfaces. The thickness of the side-grooved C(T) is $B=12.5$ mm and the net thickness is $B_N=9$ mm.

For fracture tests, all specimens are fatigue pre-cracked to ensure an initially sharp crack tip. By using a high frequency testing machine at the loading frequency of ca. 90 Hz, the fatigue pre-cracking is generated under the constant mode I loading with a very low load intensity. All fracture tests have been performed at room temperature on an MTS servo hydraulic universal testing machine. To ensure the experimental results loading rate independent, the cross head displacement is limited to 0.05 mm/min for all experiments. The initial crack front is straight in all specimens.

4.3.2 Correlation between the cohesive energy and η

The detailed study in [54] reveals that the J -integral does not equals Γ . For elastic-plastic materials Γ_0 is generally smaller than J_i and the discrepancy increases with the applied load intensity, that is, to the plastic zone size. However, one may image that the correlation between the cohesive energy and the specimen geometry is affected by J_i , the J -integral value at crack initiation in given specimens. From fracture tests, one knows that J_i is sensitive to the specimen thickness. For a given material, the ductility of the C(T) specimen decreases with specimen thickness. Therefore, one can find the correlation between the fracture energy, i.e. J_i , and η by means of FE computation in combining with fracture tests.

Distributions of local J -integral and the stress triaxiality η at crack initiation are calculated using the three-dimensional FE method, as shown in Fig. 4.3. The initial crack length and the critical force for crack initiation are measured from the experiment. In all computations, 8-nodal isoparametric elements with full integration are used. The results represent the distributions under crack initiation load, within the conventional J_2 theory. The element length in the crack extension direction and the height direction is 0.1 mm, i.e. 0.4% of the crack length. The values of J -integral are calculated by using the contour integral algorithm implemented in ABAQUS [71].

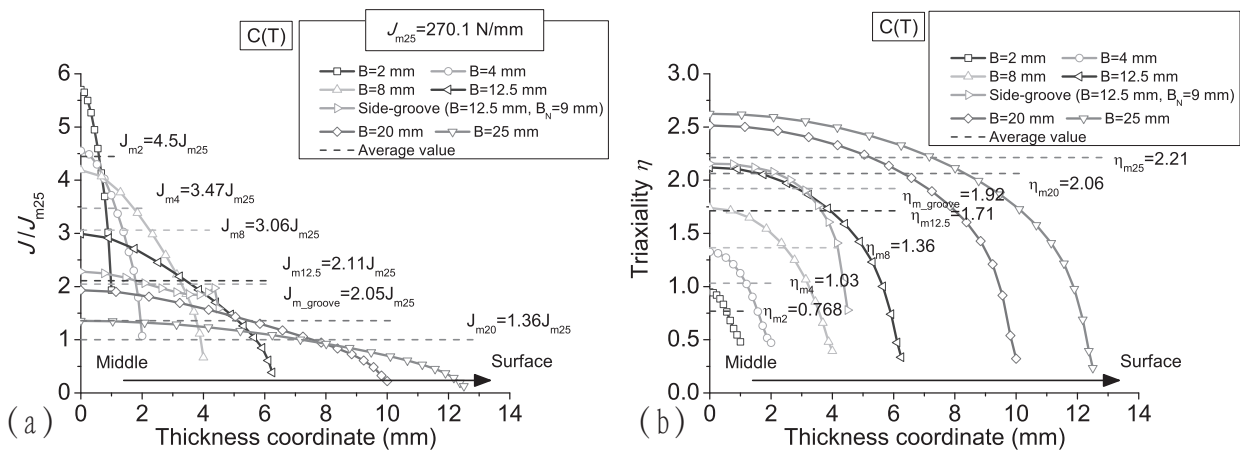


Figure 4.3: Variations of (a) J -integral and (b) η at $r/(J_m/\sigma_y) = 1$ along the crack front from center to surface at crack initiation of C(T) specimens with different thicknesses.

The distribution of the J -integral for different specimens is summarized in Fig. 4.3(a) at the crack initiation load. In the figure J_{m25} stands for the average J value of the C(T) specimen with $B = 25$ mm. In three-dimensional crack analysis, the J -integral depends generally on the z -coordinate in the thickness direction and describes the local energy release rate against crack propagation [99]. The results show that the local J -integral value varies along the crack front significantly. The maximum appears at the middle of the specimens, whereas J at specimen surfaces is a fraction of the average J -integral, which implies much smaller crack propagation speed at the specimen surface. Such variations were observed many years ago, as reported in [18, 24]. As discussed in [18], the plane stress state dominates the crack front field in a thin specimen and the J -integral at surface becomes much smaller than that of the specimen middle. In the side-grooved specimen, J is numerically uniform over a large portion of the crack front and decreases only slightly towards the surface.

Additionally, the J distribution shows significant influence of the thickness. With decreasing specimen thickness, the distribution of the J -integral becomes extremely inhomogeneous (Fig. 4.3(a)). The average J -integral, J_m , at crack initiation decreases with the specimen thickness B dramatically, which implies significant changes in J_i as a function of B . It should be noted that experimental measured J_i is effectively the average J value, J_m . According to [12], the average J is defined as

$$J_m = \frac{1}{B_{\text{net}}} \int J(b)db. \quad (4.4)$$

The stress triaxiality η characterizes the stress-state ahead of crack front, which depends on the distance to the crack tip in the finite element computations. The element size effect on triaxiality distribution along the ligament is shown in Fig. 4.4. The distributions are calculated through two specimen thicknesses. Numerical results of both thicknesses show that mesh size dependence is obvious inside the area of $r/(J_m/\sigma_y) = 0.5$. The peak value obtained from the calculation with larger element size is lower. Computations denote that the distributions of different element sizes merge together at the positions $r/(J_m/\sigma_y) > 0.5$. In accordance with the crack tip field analysis [10, 18, 24], the stress triaxiality for a crack tip is evaluated at a distance $r/(J_m/\sigma_y)=1$, to avoid influence of finite strains and finite element size.

As shown in Fig. 4.3(b), variations of the local η shows the same tendency as J . The highest value occurs at the specimen middle and decreases towards the surface. For a given specimen the average η is meaningful for characterizing crack front state, which is defined as

$$\eta_m = \frac{1}{B_{\text{net}}} \int \eta(b)db. \quad (4.5)$$

As shown in Fig. 4.3, the mean η value increases significantly with the specimen thickness, while J_m decreases. The correlation between J_m and η_m can be obtained from Fig. 4.3 and is plotted in Fig. 4.5. The symbols are taken from Fig. 4.3 and represent correlation between J_m and η_m at crack initiation. It is known that J_i depends on the specimen thickness and decreases with B monotonically, which can be represented by the stress triaxiality, as observed in [33, 61, 63, 93]. The present test series shows a linear relation between J_i and η , that is,

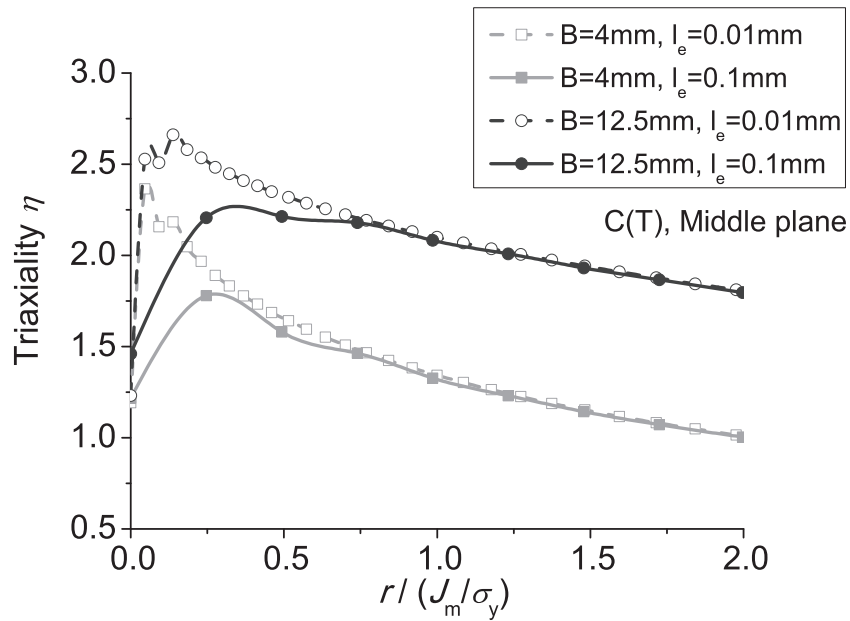


Figure 4.4: With the specimen thickness $B = 4$ mm and $B = 12.5$ mm, element size effect on stress triaxiality distribution along the ligament coordinate.

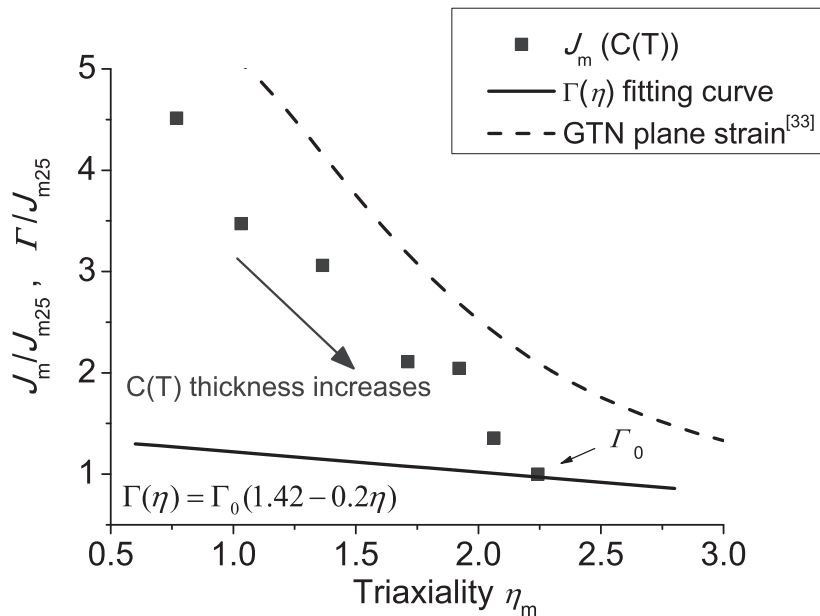


Figure 4.5: J_m with the corresponding cohesive energy Γ_0 verse η_m .

$$J_i(\eta) = J_{m25}(a - b \cdot \eta), \quad (4.6)$$

where J_{m25} denotes the lower limit of J_i obtained from the thick specimen with $B=25$ mm and characterizes fracture energy release rate under plane strain conditions. a and b are fitting parameters.

As discussed in [54], J_i is generally larger than the cohesive energy Γ_0 due to elastic unloading around the cohesive zone. If the plastic zone is negligibly small, J_i is equal to Γ_0 . Since plastic energy dissipation varies with specimen geometry, one cannot formulate a unique relation between J_i and Γ . If the cohesive energy shares the same correlation to η and can be approximately expressed as

$$\Gamma(\eta) = \Gamma_0(A - B \cdot \eta), \quad (4.7)$$

where Γ_0 is the reference cohesive energy for the plane strain specimen, approximated by the specimen with $B=25$ mm, by neglecting the influence of plastic deformations [54]. In the present study, Γ_0 takes the value of J_m with $B=25$ mm.

Obviously, the fitting parameters A and B differs from a and b . Computational experiments confirmed that Γ is hardly affected by the bending-tension loading configuration, i.e. the in-plane constraint [49, 97, 100]. Due to decreasing plastic deformation with η , one may image the cohesive energy will be not strongly sensitive to η as the J -integral. The maximum cohesive energy in the cohesive zone model should be less than $2\Gamma_0$. That means, the $J_m - \eta$ relation cannot be adopted for the cohesive zone modeling directly. From numerous computational experiments, the coefficients in Eq. (4.7) are assumed as $A=1.4$ and $B=0.2$, which gives the best approximation to the experimental results.

4.3.3 Correlation between the cohesive strength and η

The cohesive strength represents the ultimate tensile strength of the cohesive zone model. From tensile tests on notched specimens one knows that the maximum tensile stress at the notch root of a notched specimen decreases with the notch radius. That is, the ultimate strength is not constant and varies with specimen geometry as well as loading configuration. In the present work the ultimate strength should be determined experimentally from cracked specimens.

To obtain the correlation between the cohesive strength and the stress triaxiality, $T_{\max}(\eta)$, monotonic crack propagation tests were performed on the side-grooved C(T) specimen and the cracked rod bar shown in Fig. 4.6. During the tests, the stabilized crack profiles in specimens are recorded, together with the applied load, F_c . In steady-state crack growth, the local stress and the stress triaxiality along the crack front are stable and the axial stress represents the critical tensile strength depending on η . As known, η varies along the crack front. Hence, the correlation of the local tensile strength and the stress triaxiality can be obtained, with help of detailed finite element computations. It is noted that the local tensile strength distribution is the critical stress-state for stable crack growth. Accordingly, the local tensile strength is the cohesive strength for the varying stress triaxiality.

The fatigue crack propagation with lower loading amplitudes creates rather smooth crack surface. For the S460 steel, a large amount of plastic deformation is associated with monotonic crack propagation, containing significant plastic strains identified from very

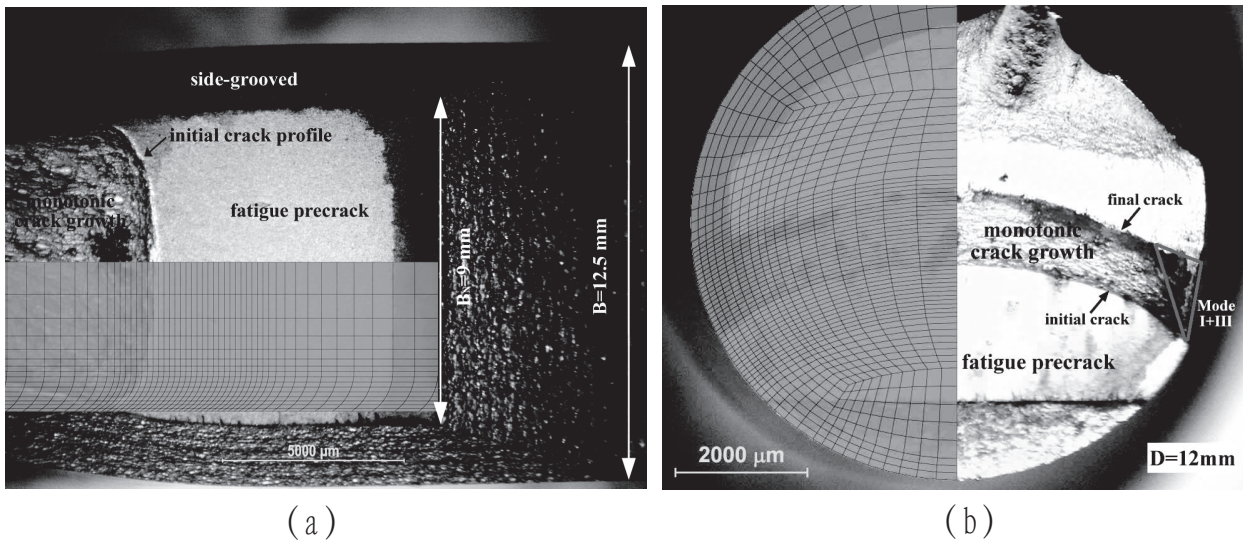


Figure 4.6: The fracture surfaces of both cracked specimens. (a) C(T) specimen; (b) cracked rod bar.

rough fracture surfaces. Changes between fatigue crack growth and monotonic fracture create obvious crack contours, which imply steady-state crack profiles under given loads, as shown in Fig. 4.6(a) for the side-grooved C(T) specimen. In finite element computations, special meshes are generated in accordance with the crack profiles, as shown in Fig. 4.6, for the given load F_c . With help of finite element computations one can find the stress distributions around a growing steady-state crack front.

Variations of the crack front in the cracked rod bar are non-uniform since the geometry of the uncracked ligament changes with crack growth. In contrast to the side-grooved C(T) specimen, slant fracture is clearly observed near the free surface of the cracked rod bar. Thereby, a critical crack front should be obtained after the onset of significant tearing crack extension, which is referred as the final crack as shown in Fig. 4.6(b).

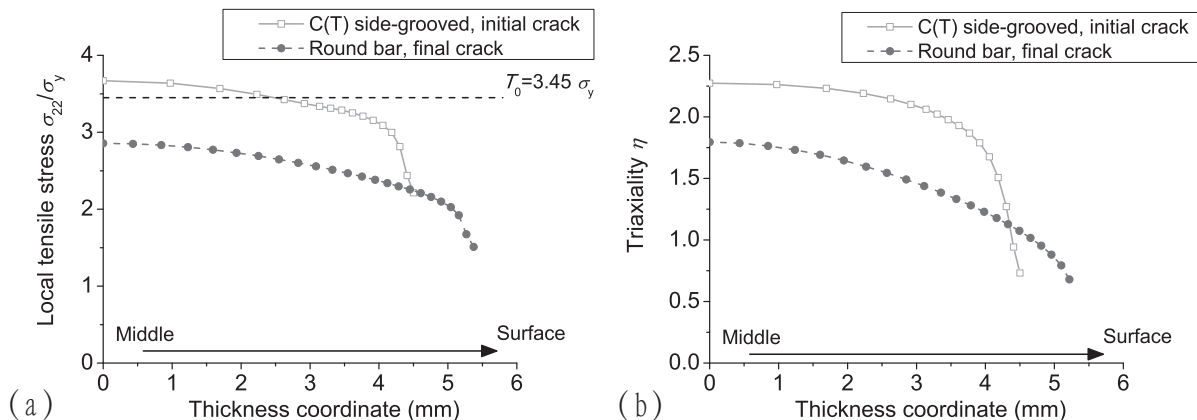


Figure 4.7: Variation of (a) the local tensile stress σ_{22} and (b) the stress triaxiality η along the crack front from center to surface of the initial crack of side-grooved C(T) specimen and the final crack of rod bar specimen.

The local tensile stress σ_{22} at the uncracked ligament $x/(J_{m25}/\sigma_y)=1$ is assumed to be the cohesive strength, together with the stress triaxiality η . Both σ_{22} and η change along the crack front. Both maximum tensile stress and η occur in the specimen middle and decreases towards the surface, as show in Fig. 4.7. It is obvious that the cohesive strength determined from the crack front stress is proportional to η . Generally, the tensile stress and the triaxiality of the cracked rod bar are smaller than those of the side-grooved C(T) specimen. It implies different cohesive strengths in the two specimens.

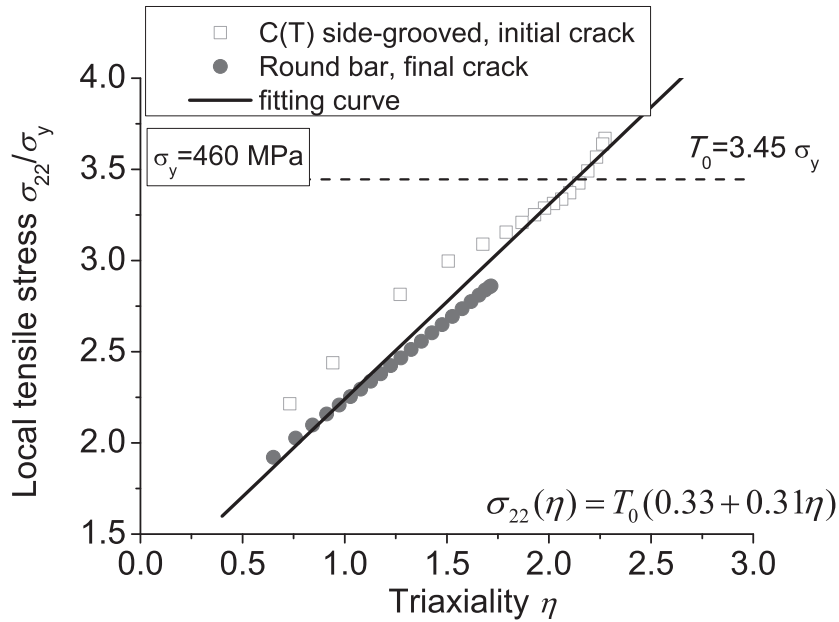


Figure 4.8: Correlation between the tensile stress and the stress triaxiality during steady-state crack growth in a side-grooved C(T) specimen and a cracked rod bar.

The correlation between the tensile stress σ_{22} and the triaxiality η is summarized in Fig. 4.8, for both specimens. During stable crack growth one may assume that the relation between the local tensile stress and the triaxiality is characteristic for the material and can be applied for cohesive zone modeling. As shown, the tensile stress increases with the triaxiality significantly, representing relation between the cohesive strength and stress triaxiality. The correlation can be approximated as a linear function, as

$$T_{\max}(\eta) = T_0(C + D \cdot \eta), \quad (4.8)$$

with T_0 as the reference traction in the cohesive zone model. Since the reference cohesive energy Γ_0 is taken from J_m with $B=25$ mm, T_0 is determined for the thick specimen with $3.45 \sigma_y$. The fitting parameters are identified as $C=0.33$ and $D=0.31$.

4.4 Computations and Discussions

To verify the proposed stress-triaxiality-dependent cohesive zone model, three-dimensional finite element computations are conducted on the side-grooved C(T) and the cracked rod bar. Cohesive elements are arranged on the ligament plane to simulate the crack extension.

Due to symmetry, only one quarter of the specimens needs to be simulated. The inelastic behavior of the material is described by the J_2 plasticity of ABAQUS. The true stress-strain curve was determined from tensile tests. The cohesive parameters for CZM and the correlations between the cohesive parameters and the stress triaxiality for TCZM have been specified in the previous sections.

In cohesive zone modeling, material degradation occurs with softening in traction-separation. To improve convergence, the cohesive parameters are adjusted with the stress triaxiality only before δ_0 is reached. That is, damage process in the softening stage is not further affected by the stress triaxiality and the parameter values will be inherited from the last increment as a function of the stress triaxiality.

4.4.1 Crack growth simulation in the side-grooved C(T) specimen

In the side-grooved C(T) specimen, the initial crack front is straight. The FE mesh was generated with a straight crack front. Eighteen element layers were implemented in the thickness direction, with a bias ratio of 5.0. The groove notch radius of 0.1 mm was included in the model. Five extra element layers were generated for the side-grooved part of the specimen. The smallest element length is 0.1 mm in both crack extension and height directions.

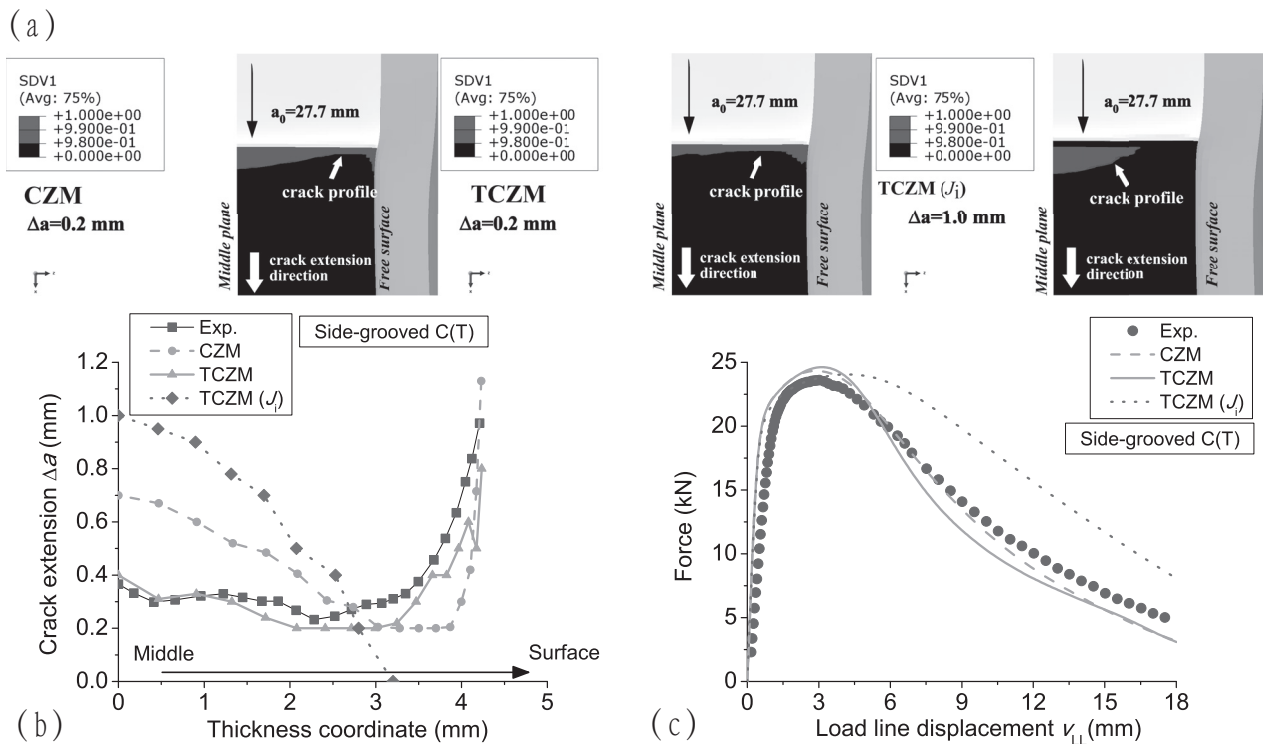


Figure 4.9: Comparison between experimental and computational predictions of the side-grooved C(T) specimen using different cohesive zone models. (a) The predicted fracture surfaces. (b) Crack profiles. (c) Load-line displacement curves.

The side-grooved C(T) specimen was computed based on different cohesive model parameters, i.e. CZM for the conventional cohesive zone model, TCZM for the stress-triaxiality-

dependent cohesive zone model as well as $\text{TCZM}(J_i)$ for the TCZM correlated by the experimental $J_i - \eta$ curve. Comparison between computations and experiment is plotted in Fig. 4.9(c), in which curves of the load versus load line displacement are illustrated. Agreement between the TCZM/CZM simulations and the experiment is obvious. Both load-load line displacement curves from TCZM and CZM computations seem not sensitive to stress triaxiality dependence in the modeling. They give generally good agreement to the experiment.

Significant difference from computations is observed in crack profile development. Fig. 4.9(a) shows the predicted fracture surfaces. Curves in Fig. 4.9(b) represent computational and experimental crack fronts in the side-grooved C(T) specimen, which is no longer straight after crack initiation. Due to additional stress concentration from the side groove, the crack near the surface grows more quickly than that in the specimen middle. This behavior can be caught by the TCZM correctly, while the CZM model gives a different profile from the reality. Due to constant cohesive strength and fracture energy, the crack under higher triaxiality is much quicker than the crack with lower triaxiality. It results in a extremely difference in specimen middle and near the notch root, while the crack below the notch extends too little. The TCZM model provides a reasonable prediction in both global and local fracture parameters.

In Fig. 4.9 an additional computation is documented for comparison, under the symbol $\text{TCZM}(J_i)$, which denotes the computation with the experimental correlation of J_m vs. η_m , Eq. (4.6), for the stress triaxiality dependence of the fracture energy. That is, the experimental relation is directly used for $\Gamma(\eta)$. The computation reveals that, due to the extremely high fracture energy applied near the free surface, no crack extension is observed near the notch root, even with the middle crack extension up to 1 mm. In addition, the excess fracture energy leads to overestimate in the load-displacement curve. From such observation Eq. (4.6) is not adequate for crack growth simulation.

Figure 4.10(a) shows development of the crack fronts of the side-grooved C(T) specimen from both CZM and TCZM. As observed, the crack near the grooved surface extends

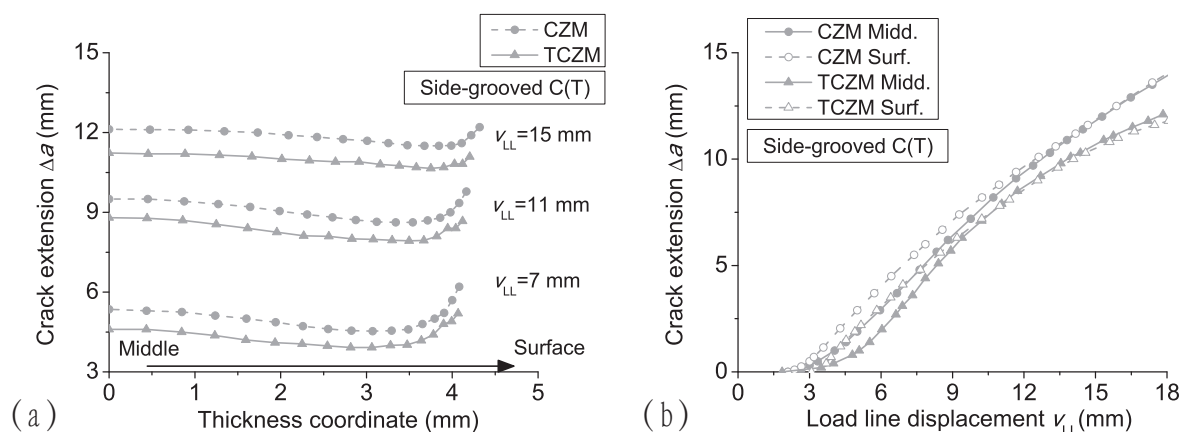


Figure 4.10: Comparison of computational predictions from different cohesive zone models on the side-grooved C(T) specimen. (a) Development of the crack front. (b) Crack extension vs. load-line displacement.

faster than the middle plane one after crack initiation. With crack growth, however, both models predict acceleration in the middle plane crack. The difference between the surface crack length and the middle plane crack disappear with crack growth and the crack front is approaching a straight line again. TCZM predicts a flatter crack front than that from CZM. The comparisons of the crack extension at the free surface and the middle plane vs. load-line displacement from both models are shown in Fig. 4.10(b). The predicted crack extension from TCZM is always smaller in comparing with the result from CZM. The discrepancy in the numerical results can be explained from stress triaxiality evolution with crack extension.

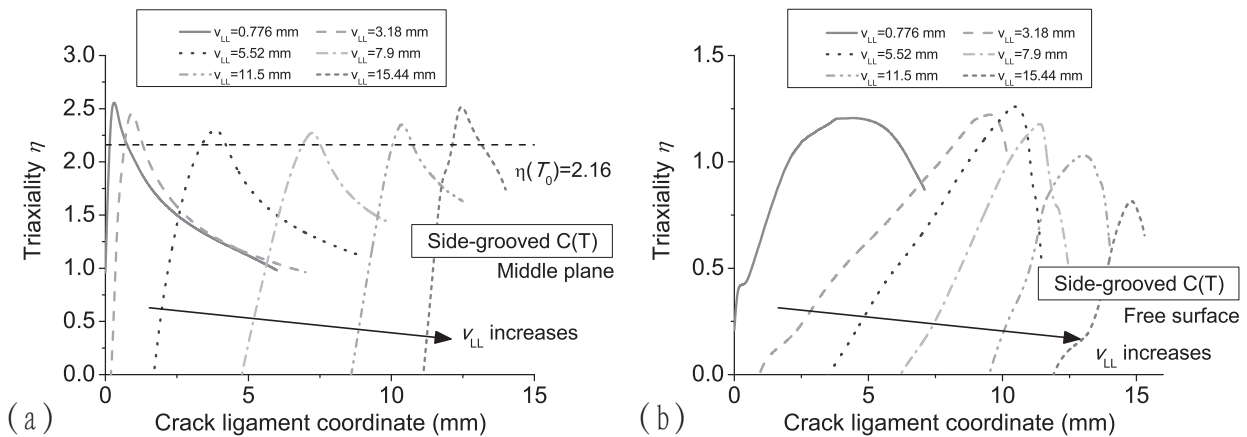


Figure 4.11: Stress triaxiality variations along uncracked ligament at various loading stages in the side-grooved C(T) specimen. (a) Middle plane. (b) Free surface.

Figure 4.11 shows stress triaxiality variations along uncracked ligament at various loading stages in the middle plane and the free surface, respectively. With crack extension, the peaks of the stress triaxiality shift. The peak values from the TCZM modeling depend on cohesive strength and are generally higher than the triaxiality from Eq. (4.8) for constant cohesive strength T_0 . This implies that the cohesive strength in TCZM at the middle plane is always higher than T_0 , it results in slower crack growth predicted from the TCZM.

At the free surface of side-grooved specimen, the fracture energy is dominant for crack extension [68]. As shown in Fig. 4.11(b), the triaxiality values at the free surface are much lower in comparing with the values at the middle plane. According to Eq. (4.7), a larger cohesive energy in TCZM is needed for a crack increment, which leads to slower crack growth prediction at the free surface. Consequently, the predicted crack extension predicted from TCZM is retarded in comparing with CZM.

4.4.2 Crack growth simulation for the cracked rod bar

In the rod bar the crack front is generally a curve. The fatigue crack front is obtained from the specimen for EF meshing for the stress intensity factor distribution. The FE meshes are generated in compliance with the initial crack profile. The thickness of the region near the free surface is partitioned about 1.5 mm. Ten layers of elements are used through this region. Each layer has the same thickness. Fifteen layers of elements are used through the

rest region of the cross section till the middle plane. The layer thickness in this region has a bias ratio of 3.0. The smallest element length near the crack front in crack extension direction and the height direction is 0.1 mm.

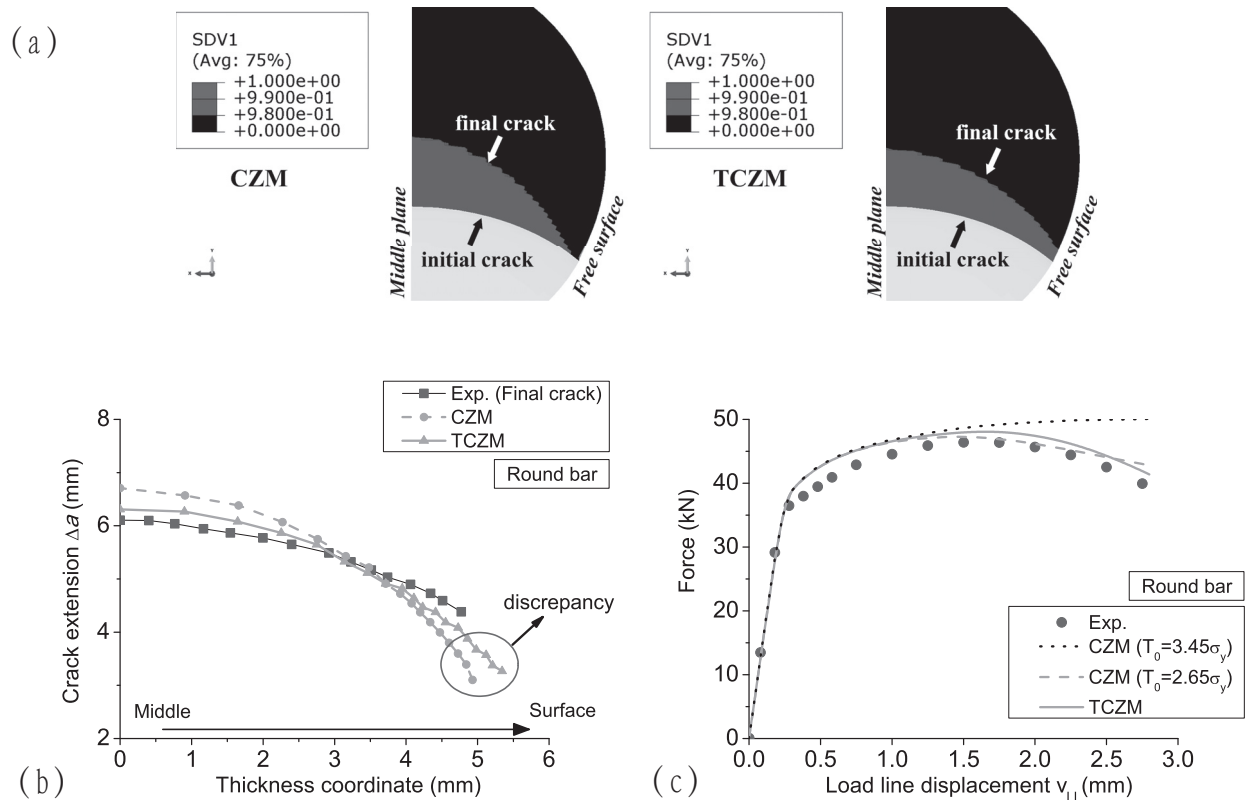


Figure 4.12: Comparison between experimental and computational predictions of the cracked rod bar using different cohesive zone models. (a) The predicted fracture surfaces. (b) Crack profiles. (c) Load-line displacement curves.

Predictions from cohesive zone models are illustrated in Fig. 4.12, together with experimental records. With the same initial crack profile, computations were conducted under displacement controlling. CZM denotes the conventional cohesive zone model with constant model parameters, while TCZM is from the stress-triaxiality-dependent model. The computation of CZM shows much higher loading capacity if the cohesive parameters identified in the side-grooved C(T) specimen are applied, as shown in Fig. 4.12(c). The reason can be explained in Fig. 4.7. It shows that due to the geometric effect, the tensile stress and the triaxiality values of the cracked rod bar are much smaller in comparing with the values of the side-grooved C(T) specimen.

Figure 4.12(b) shows the comparison of the crack profiles between experimental result and predictions. The crack growth near the specimen center predicted from the TCZM seems to give more accurate results than that from the const CZM. It can be explained based on the triaxiality dependence, as observed in the C(T) specimen.

The results near the free surface, however, that the computations do not approach the experimental front. As shown in Fig. 4.6(b), the crack front near the free surface is influenced by shear failure mode, so that the crack surface becomes locally not plain. Present

4 Stress-triaxiality-dependent cohesive zone model

discussions of cohesive zone model can only simulate normal failure and the predictions from TCZM gives too low crack growth velocity. No crack extension at the free surface was predicted by the CZM.

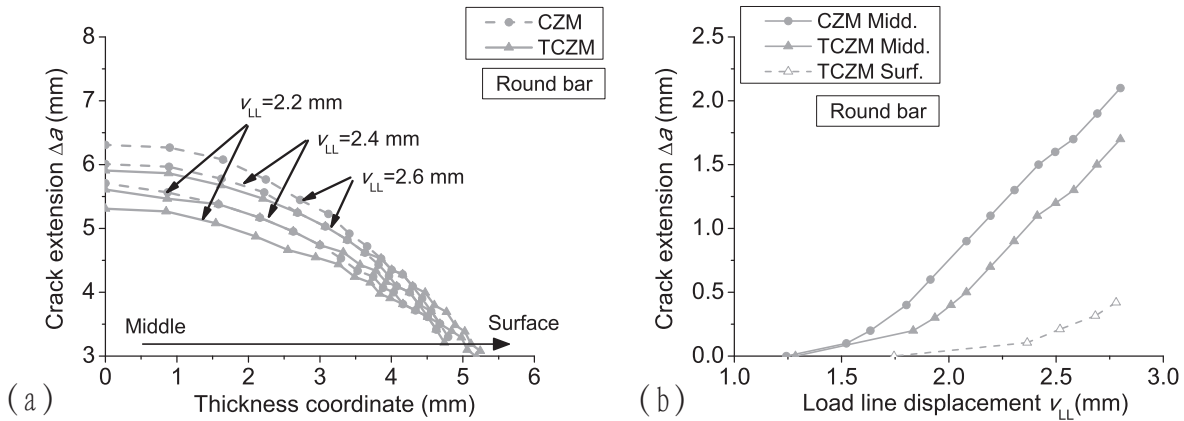


Figure 4.13: Comparison of the numerical results from different cohesive zone models of the cracked rod bar. (a) Variation of the predicted crack fronts for various loading stages. (b) The predicted crack extension vs. load-line displacement.

Figure 4.13(a) shows the predicted crack fronts corresponding to various loading stages of both models. The comparisons of the crack extension at the free surface and the middle plane vs. load-line displacement from both models are shown in Fig. 4.13(b). Similar to the numerical result of the side-grooved C(T) specimen, the predicted crack extension at the center of the specimen from TCZM is always slower in comparing with the result from CZM. In addition, with crack propagation, crack extension at the free surface is predicted from TCZM, although the simulated result is much smaller in comparing with the experimental result.

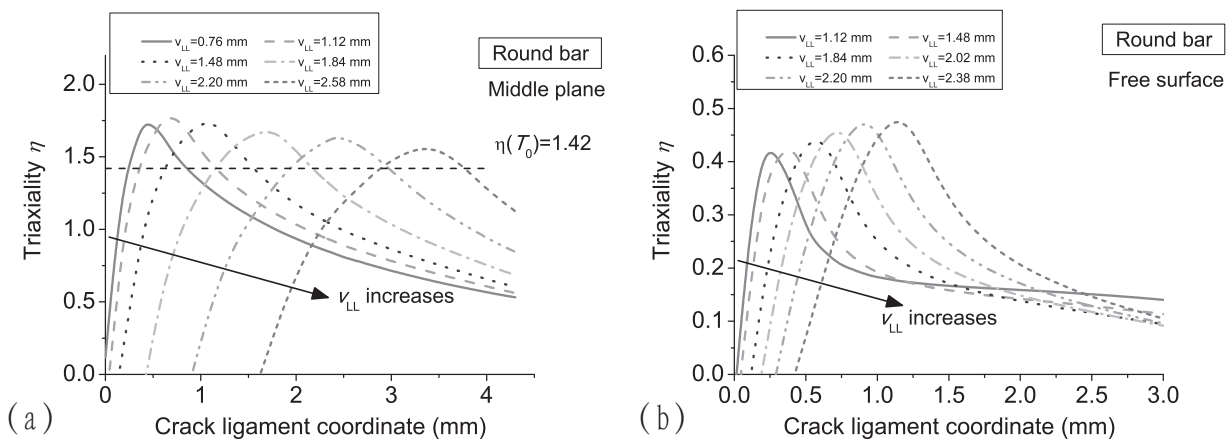


Figure 4.14: The triaxiality distribution in the uncracked ligament at various loading stages of the cracked rod bar. (a) Middle plane; (b) Free surface.

Figure 4.14(a) shows the triaxiality distributions along the ligament coordinate at the middle plane. Note that the peak values of the triaxiality distributions are higher in comparing with the triaxiality value of the constant cohesive strength. Higher triaxiality value should correspond to higher cohesive strength. This way, the resistibility of crack extension in TCZM would be obvious which leads to slower crack extension prediction. Fig. 4.14(b) shows the triaxiality distributions at the free surface. Note that the peak values are much lower in comparing with the values at the middle plane. For the smooth specimens, it has been confirmed that the cohesive strength would influence the computational results primarily. Thus, excessive lower cohesive strength applied in TCZM makes the possibility of crack extension at the free surface.

4.5 Summary

The formulation and validation of a stress-triaxiality-dependent cohesive zone model is presented. It is confirmed that cohesive parameters, cohesive strength and cohesive energy, are not material constants as they depend on the triaxiality of the stress-state. The correlations of the stress triaxiality and cohesive parameters are identified based on the experimental results. Proposed TCZM and conventional CZM have been applied to model three-dimensional crack extension, which were represented by the side-grooved C(T) specimen and the cracked rod bar containing a semi-elliptical surface crack. Experiments on these specimens were carried out to validate the simulation results. The present results confirm the following conclusions:

- Experiments reveal that the cohesive parameters are stress triaxiality dependent. The linear triaxiality dependence in the cohesive zone model significantly improves three-dimensional crack growth computation. Generally, the cohesive strength increases with the stress triaxiality is higher, whereas the cohesive energy decreases.
- The cohesive traction seems more sensitive to the stress triaxiality than the cohesive energy. The correlation of cohesive strength vs. stress triaxiality, $T_{\max}(\eta)$, can be determined by calculating a critical stress-state at the onset of stable crack growth over the whole crack profile.
- The correlation of cohesive energy vs. stress triaxiality, $\Gamma(\eta)$, can be determined according to the tendency of the values of J -integral at crack initiation under different stress triaxiality conditions. However, due to the dominance contribution of J_i from plastic dissipation energy at lower stress triaxiality condition, the value of J_i would be significant larger than Γ_0 . Consequently, the precisely determination of $\Gamma(\eta)$ has to verify the predictions with the experimental results.
- Present study can only consider normal failure simulation. For the rod bar specimen, tearing crack extension is observed near the free surface. Predictions show significant deviation with the experimental result in predicting mix mode (mode I+III) crack. The quantification of the effect of the stress-state requires the Lode parameter apart from the triaxiality parameter [101–103]. Extension of the present correlations $T_{\max}(\eta)$ and $\Gamma(\eta)$, and prediction of the crack growth for different cracks in different ductile metals are required to further substantiate the versatility of the model.

5 A uniform CZM for both fatigue and fracture crack simulation

5.1 Introduction

5.1.1 State of art of cyclic cohesive zone model

Cohesive zone modeling provides an alternative way to predict crack growth in ductile materials under elastoplastic loading conditions. The applicability of cohesive zone model for fatigue crack propagation, which is denoted as cyclic cohesive zone model (CCZM), has been introduced in Chapter 1. Here, the representative milestones in the development of CCZM are summarized.

a. de-Andrés model

The attempts have been made to use CCZM to describe fatigue failure since the end of 20th century. de-Andrés et al. [104] simulated the fatigue crack propagation by adding a linear un/reloading path towards the origin to the exponential cohesive law. A damage variable D which varies between zero to unity, is introduced to describe damage process. However, the damage evolution is not included in the formulation of the cohesive law as an intrinsic variable. In this way, the unloading and subsequent reloading would coincide, cyclic damage accumulation is not considered. The cohesive zone eventually stabilizes which causes shake down effects and crack arrest under cyclic loading [105]. To prevent this problem, the hysteretic un/reloading as well as the damage evolution in the cohesive zone should be introduced.

b. Nguyen model

Nguyen et al. [105] developed a linear cohesive law that incorporates the un/reloading hysteresis to predict fatigue life under several loading conditions. The loading stiffness is chosen as an internal variable in the spirit of damage theories and the damage evolution equation is governed by the loading path direction, the current stiffness value and the normalized separation rate. The unloading path is linear towards the origin, but the reloading stiffness evolves in accordance with the evolution equation and degrades steadily. The accumulation of damage within the cohesive zone is accounted for on a cycle-by-cycle basis and eventually leads to complete decohesion and crack extension. In a parallel development, Yang et al. [106] proposed a similar model by defining the un/reloading stiffness in a general polynomial expansion. The evolution law of the stiffness is attached to the displacement jump between crack faces and the model also allows for damage accumulation during unloading.

In a further application of Nguyen model, Maiti and Geubelle [107] simulated the fatigue crack growth of polymers and then to investigate the effect of fatigue crack retardation induced by crack closure [108]. Eliáš and Le [109] investigated fracture behaviors of quasibrittle structures under compressive fatigue. In combination with an exponential cohesive law, Serebrinsky and Ortiz [110] showed the ability of the model to predict the fatigue-crack nucleation. Later, Arias et al. [111] extended the model to study the electro-mechanical ferroelectric fatigue.

It should be noted that consideration of un/reloading hysteresis has the important consequence of preventing shakedown, thus allowing for steady crack growth. Moreover, regarding the damage evolution equation, the cohesive behavior of the material under cyclic loading is independent of specification of the monotonic cohesive law.

c. Roe-Siegmund model

The paper about the CCZM attracted many researchers was published by Roe and Siegmund [112] for simulating the interface fatigue crack growth. Based on the concepts of continuum damage mechanics by Lemaitre [91], a damage variable is supplemented by an evolution law to account for the accumulation of damage. The description of the damage evolution is defined in the form of $\dot{D}_c = \dot{D}_c(T, \delta, D_c)$, with $\dot{D}_c \geq 0$. Within the cyclic loading process, the accumulative damage makes the degradation of cohesive law by substituting the initial cohesive strength, T_0 , by the current one, $T_{0_cyc} = (1 - D)T_0$. The damage evolution law includes the material endurance limit and damage initiation condition. Originally, Roe and Siegmund [112] assumed the un/reloading path follows a linear relationship with a stiffness equal to that of the current cohesive law at zero separation, which leads to residual separation.

The model has been applied to investigate the fatigue crack growth in various conditions and can reproduce many basic characteristics which are similar to the experimental phenomena, i.e. the shield of crack bridging [113], the multi-layer structures with different constraint conditions [114, 115], the mismatched bi-material interfaces [116] and the effect of strain gradient plasticity [117]. In addition, Abdul-Baqi et al. [118] described the fatigue damage process in a solder bump. Jiang et al. [119] predicted the influence of overload and loading mode on three-dimensional fatigue crack growth. Liu et al. [120–122] utilized the model to investigate the influence of shot peening on the fatigue crack growth and relaxation of residual stress under cyclic load.

d. Extensive damage evolution equations

The key feature in CCZM is the description of cyclic damage accumulation and its combination with the general cohesive law. Common for all the considered methods is that the development of damage is described by an evolution equation. One can find a large variety of realisations.

In the framework of XFEM combined with CCZM, Xu and Yuan [39, 40] proposed a new evolution equation for the damage variable, which neglected the damage induced by the shear stress based on the experimental observation that the crack propagation is dominated by mode I mechanism [123]. In this model, nucleation of damage once the nonlocal equivalent principal stress, σ_{eq} , ahead of the cohesive zone tip is greater than the material fatigue limit f_0 . Numerical predictions successfully obtained linear curves

comparable to the Goodman formulation. Li and Yuan [124] extended the model to include the effect of stress ratio R on the accumulated cohesive length.

Bouvard et al. [125] formulated a damage evolution equation in a thermodynamic framework. The thermodynamic force associated with the damage variable is employed as the driven force for damage evolution. The incremental damage evolution is expressed as $\Delta D_c = \Delta D_c(D_c, Y, \delta)$ with the following features: (i) damage only begins if the thermodynamic force Y is higher than a threshold Y_0 ; (ii) the damage increment is related to the opening increment; (iii) damage occurs only under loading conditions. In the work of Bouvard et al. [125], a creep damage was defined additionally to take into account the time effect observed in loadings at low frequency. An enhancement of Bouvard model was proposed by Moriconi et al. [126] to study the fatigue crack propagation in a hydrogenous environment. Sun et al. [127] adopted the creep damage variable to study the intergranular crack growth in a nickel-based superalloy.

Ural et al. [128] used a damage degradable cohesive stiffness and a damage evolution law which considered the possibility of damage healing if the surface traction falls below a threshold. In this way, fatigue crack growth retardation effects due to overload could be modeled. Moreover, a damage-accumulation scaling function is adopted through scaling the cohesive parameters in predicting high cycle fatigue.

Gong et al. [129] presented a CCZM for interface fatigue problems. The cumulative damage is related to the average opening displacement across the interface δ^{avg} and the cohesive ultimate separation δ_u . The cohesive properties of the cohesive zone gradually reduce as the opening displacement increases for each loading cycle.

Cycle-by-cycle calculation can be applied in the low or very low cycle fatigue regime. For high cycle fatigue, it would be more efficient to formulate fatigue damage growth relations in cycle-based format by assuming the damage increment per cycle to be very small. Different formulations of the damage evolution rate aimed at high cycle fatigue simulation have been published, i.e.

- Turon et al. [130] combined damage mechanics and the Paris' law to establish damage evolution in terms of the fatigue crack growth rate. A cycle jump strategy was implemented in the calculation. This CZM was applied for fatigue crack growth analysis in composites.
- Khoramishad et al. [131–133] proposed a strain based fatigue damage rate function, wherein the strain is defined using the interface separation of cohesive elements with non-zero initial thickness.

5.1.2 Motivation

The CCZMs published have been applied for predicting the fatigue crack growth behavior and many fatigue features can be captured. However, most proposed models only consider cyclic damage accumulation without full interactions with monotonic damage. That is, the contribution of the material rupture mechanism is negligible. In this case, these models can only generate the essential fatigue features, especially for fatigue crack growth in Regime II. Regime III associated with the high rate of fatigue crack growth and severe plastification cannot be represented. Furthermore, the CCZM needs more detailed experimental verification.

In the present work, a new CCZM is developed for predicting fatigue crack growth in both Regime II and Regime III. Experiments of fatigue cracks are performed to establish and verify the model. Much emphasis are put on examining the performance of the CCZM with plastic unloading.

5.2 A new cyclic cohesive zone model

The cohesive model is introduced to characterize localized material failure around the crack-tip. In simulation of fatigue crack growth the CCZM has to be able to consider both ductile failure and accumulative damage due to cyclic fatigue loading, which builds the significant difference from the conventional CZM for rupture. The CCZM should characterize different damage evolution mechanisms for fatigue crack growth in metallic materials: monotonic damage due to high plastic deformations and cyclic damage from repeated accumulative stresses/strains. Since both damage mechanisms are so different that two damage evolution equations become necessary. In the present work, it is assumed that the total damage evolution is decomposed as

$$\dot{D} = \dot{D}_m + \dot{D}_c, \quad (5.1)$$

where the damage variable $D = \int_t \dot{D} dt$ stands for the material degradation and represents failure if $D = 1$.

5.2.1 Damage evolution for monotonic loading

Under monotonic loading condition, following the feature of traction-separation behavior in the cohesive zone, cohesive traction increases/keeps constant with accrued separation until a critical separation δ_0 is reached. Therefore, no damage accumulation is assumed for the ascending stage. Once δ_0 is exceeded, the traction decreases towards zero with further separation. For the descending stage, the constitutive equations of traction-separation relation can be expressed with the incorporated damage evolution mechanism. The cohesive traction degrades with increased monotonic damage accumulation, as

$$T = T_0 \begin{cases} g(\delta) & 0 \leq \delta \leq \delta_0 \\ (1 - D_m) & \delta_0 < \delta \leq \delta_u \\ 0 & \delta_u < \delta \end{cases} \quad (5.2)$$

In above, $g(\delta)$ is a monotonic function which experiences an ascending tendency with respect to δ . The expression of the monotonic damage variable D_m is related to δ_0 and δ_u , for the conditions of $D_m = 0$ at $\delta = \delta_0$ and $D_m = 1$ at $\delta = \delta_u$. For instance, a linear monotonic damage can be defined by,

$$D_m = \frac{\delta - \delta_0}{\delta_u - \delta_0}. \quad (5.3)$$

The monotonic function between δ_0 and δ_u ensures that \dot{D}_m is always a positive value. Should $g(\delta)$ take an exponential function which suggested by Needleman [47], a cohesive law can be formulated for the monotonic loading case, as

$$T = T_0 \begin{cases} \exp(1 - \frac{\delta}{\delta_0})(\frac{\delta}{\delta_0}) & 0 \leq \delta \leq \delta_0 \\ (1 - \frac{\delta - \delta_0}{\delta_u - \delta_0}) & \delta_0 < \delta \leq \delta_u \\ 0 & \delta_u < \delta \end{cases} \quad (5.4)$$

According to Eq. (1.3), the cohesive energy for material separation can be obtained from Eq. (5.4) as

$$\Gamma_0 = T_0(\delta_0(e - 2) + \frac{1}{2}(\delta_u - \delta_0)), \quad (5.5)$$

where $e = \exp(1)$ is the Euler's number. An illustration of monotonic damage evolution with the corresponding cohesive law is shown in Fig. 5.1.

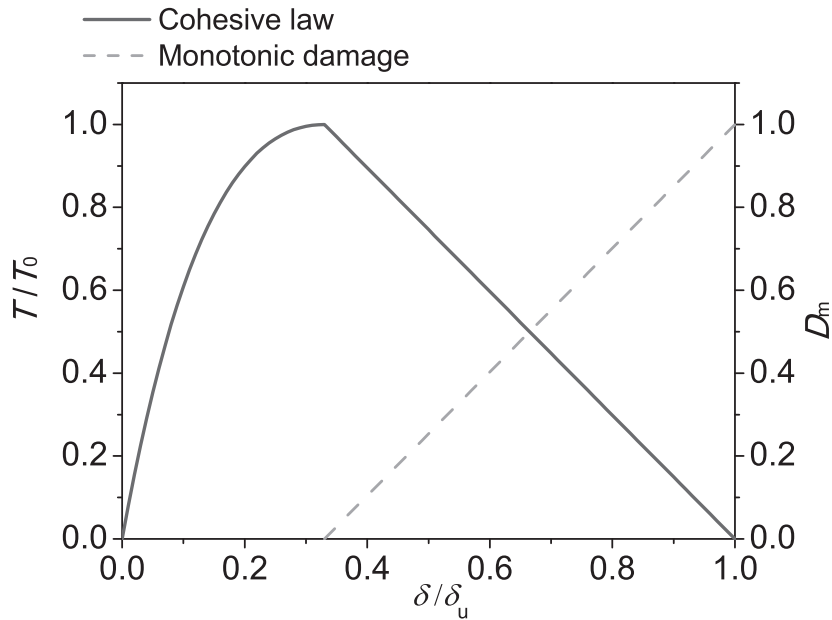


Figure 5.1: Illustration of monotonic damage evolution with corresponding cohesive laws.

5.2.2 Damage evolution for cyclic loading

a. Cyclic damage evolution equation

Fatigue failure under cyclic loading has to be described by a varying damage accumulative process. For present study, the fatigue damage evolution equation suggested in [112] reasonably reflects the accumulative damage for ductile materials, which reads

$$\dot{D}_c = \frac{\dot{\delta}}{d_\Sigma} \left(\frac{T}{T_0(1-D)} - n \right) H(\delta_{acc} - \delta_0), \quad \dot{D}_c \geq 0. \quad (5.6)$$

Here, the total damage variable D which covers both monotonic damage D_m and cyclic damage D_c is applied to describe the current maximum cohesive traction, $T_0(1-D)$. $\dot{D}_c \geq 0$

represents the irreversibility of cyclic damage accumulation. $\dot{\delta}$ is the separation increment, with $\dot{\delta} = \delta_t - \delta_{t-\Delta t}$. δ_{acc} is defined as the separation accumulation and $\delta_{\text{acc}} = \int |\dot{\delta}| dt$. The Heaviside step function $H(\delta_{\text{acc}} - \delta_0)$ implies that the cyclic damage will not start to evolve until the current accumulated separation is greater than the critical separation δ_0 .

The cyclic damage evolution \dot{D}_c is also dependent on two additional parameters. The accumulative length d_Σ is used to scale the increment of the material separation. Normally, it is a multiple of δ_0 . n is the material dependent damage controlling parameter.

b. Un/reloading path

To properly describe fatigue crack propagation under cyclic loading, the definition of unloading and reloading paths is indispensable. The present study focuses on the low cycle fatigue regime, hence, the ductile unloading mechanism is applied in the current CCZM, as shown in Fig. 1.5(b). Following the suggestions in [40, 65, 112], for ductile material, the unloading and reloading processes are assumed to proceed along with a current computed stiffness

$$k = \frac{T_0(1-D)e}{\delta_0}. \quad (5.7)$$

For the case no damage accumulation, $D = 0$, the slope equals to the initial cohesive stiffness at zero separation. This assumption leads to that after a completed unloading, there exists the possibility for the presence of residual separation within the cohesive zone. Correspondingly, the traction-separation behavior follows a linear relationship, as

$$T_t = T_{t-\Delta t} + k\dot{\delta}, \quad (5.8)$$

where T_t and $T_{t-\Delta t}$ are the cohesive traction in the different time increments. During numerical simulation, a single progress of unloading or reloading consists of several increments so that the loading force is removed or added gradually. Within an increment, the stiffness is modified according to the current value of total damage, D . As a result, the path for a single unloading or reloading is a multi-linear line.

After the cohesive element is broken, to prevent adjacent continuum elements from penetrating each other during the unloading or compression period, a contact condition should be considered in the normal direction. A high penalty stiffness A is introduced to prevent the overlapping of cohesive elements. The penalized equation is given by

$$T = A \cdot T_0 \cdot \exp(1)\left(\frac{\delta}{\delta_0}\right), \quad \delta < 0. \quad (5.9)$$

c. Envelop curve

As specified previously, proposed suggestion of the constitutive relation for CCZM is through deteriorating the peak traction due to the evolution of cyclic damage variable. The cohesive law in monotonic case provides an envelop line when cyclic loading occurs. With evolutions of both damage variables, D_m and D_c , the interaction of rupture and fatigue can be considered in the cohesive law, which is effectively the current degraded cohesive envelope, which can be expressed as

$$C_D = \begin{cases} T_{0_cyc} \exp\left(1 - \frac{\delta}{\delta_0}\right) \left(\frac{\delta}{\delta_0}\right) & \delta \leq \delta_0 \\ T_{0_cyc} & \delta_0 < \delta \leq \delta_c, \\ T_0 \left(1 - \frac{\delta - \delta_0}{\delta_u - \delta_0}\right) & \delta_c < \delta \leq \delta_u \end{cases} \quad (5.10)$$

with $\delta_c = \delta_0 + D(\delta_u - \delta_0)$ and the current cohesive strength of the material $T_{0_cyc} = T_0(1 - D)$.

For the application of Eq. (5.8), the inequality must be satisfied that,

$$T \leq C_D. \quad (5.11)$$

5.2.3 Operating mechanism of the cyclic cohesive zone model

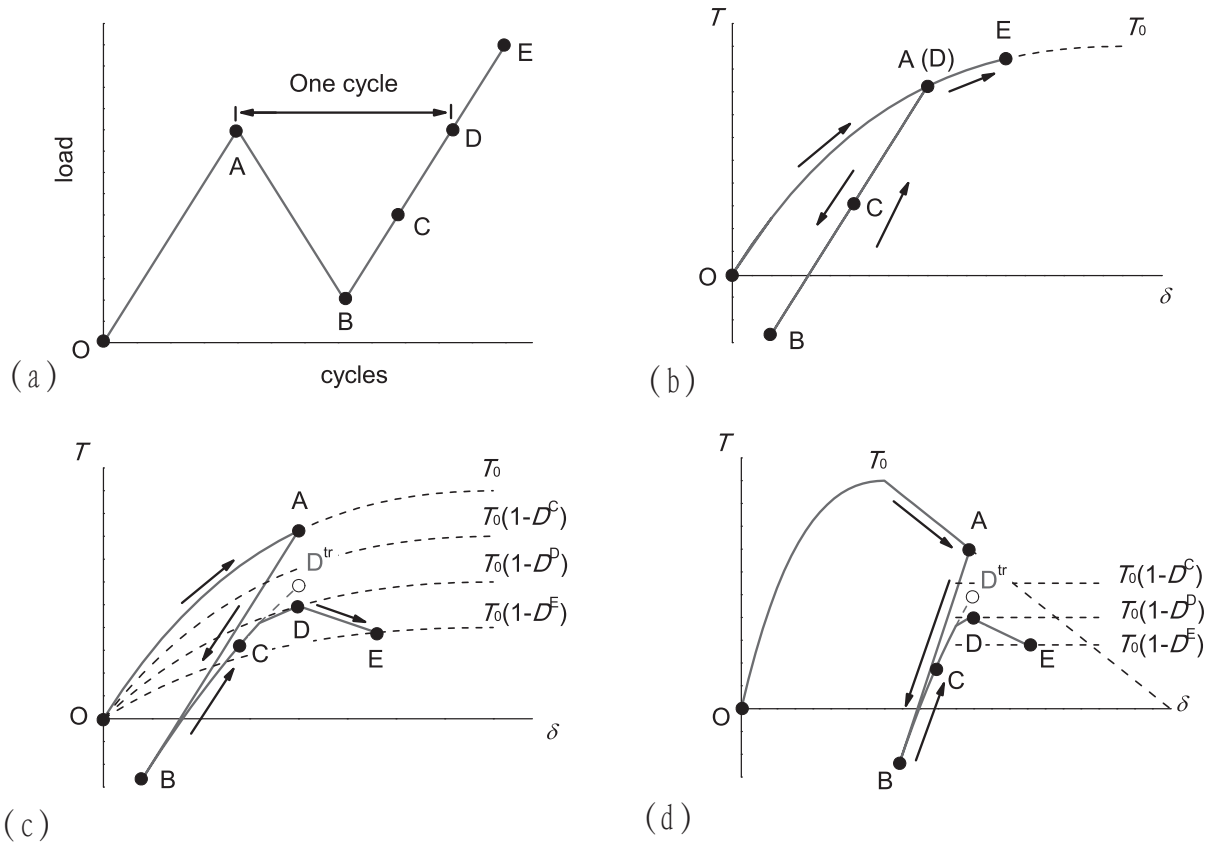


Figure 5.2: Illustration of cyclic process of CCZM. (a) Load spectrum. (b) No damage accumulation. (c) Damage accumulation with unloading point before δ_0 . (d) Damage accumulation with unloading point after δ_0 .

The damage process of the present model should be noted. Generally, it is assumed that the reloading path should not exceed the monotonic cohesive envelop. Once the reloading

curve intersects the envelop, loading is bounded to remain on the envelop and no damage is accounted [105, 106, 112]. Present model suggests a continuous damage accumulation within the whole loading process. Once the reloading path intersects the envelop line, with a further loading, damage accumulates successively according to Eq. (5.6) based on the separation increment $\dot{\delta}$. In this step, Eq. (5.8) will provide a trial traction response firstly. Then, the equality condition of Eq. (5.11) should be fulfilled and the trial traction response will be mapping to the current maximum load bearing capacity C_D . A detailed illustration of the correlation between the un/reloading path and the cyclic process of CCZM is shown in Fig. 5.2. Detailed numerical comparison of those two models will be presented in the following section.

Figure 5.2(a) denotes a load spectrum. The loading path $O \rightarrow A$ is assumed as the first loading step. Obviously, the response of the cohesive zone in the first loading step should comply with the monotonic cohesive law which is defined in Eq. (5.4).

Following by a loading path $A \rightarrow B \rightarrow C \rightarrow D$, which denotes one cyclic loading cycle. Fig. 5.2(b) illustrates the case that no damage accumulates after a completed load cycle. If $D^D = 0$, which means no cyclic damage accumulation contributes to the maximum load bearing capacity of the cohesive zone. Eq. (5.10) goes back to Eq. (5.4). Therefore, the cohesive response for a further loading ($D \rightarrow E$) follows the initial monotonic cohesive law.

Figure 5.2(c) and (d) denote the case that cyclic damage accumulation exists after a completed load cycle. Within the unloading and reloading process, to update the traction at current time step, a trial traction increment is chosen which is given according to Eq. (5.8). Should the condition of Eq. (5.11) be fulfilled, current traction is then updated based on the trial traction increment. Otherwise, the trial current traction should be mapping to the cohesion C_D and the equality of Eq. (5.11) is true. The point D denotes the condition that the equality holds in Eq. (5.11). The next loading path $D \rightarrow E$ represents a further loading case. If $D^D > 0$, as shown in Fig. 5.2(c) and (d), the damage evolution for next time increment is accounted continuously and the evolution equation is following Eq. (5.6).

The FE software package ABAQUS [71] offers a library of cohesive elements for 2D and 3D modeling. The separation behaviors of the cohesive elements can be defined within the constitutive relations for the cohesive zone. The aforementioned CCZM has been implemented via the user definite subroutine UMAT.

5.3 Validation of the cyclic cohesive zone model

To verify the proposed model, numerical experiments are performed. The material properties are taken to be in accordance with high strength steel alloy with Youngs' modulus $E = 208$ GPa, Poisson's ratio $\nu = 0.3$. The initial yield strength $\sigma_y = 1200$ MPa and the plastic behavior can be described in Eq. (4.3) with the bulk modulus $K = 1500$ MPa and the strain hardening exponent $n = 0.015$. The bulk material for the continuum elements is described by the classical J_2 theory.

For the current investigation, the cohesive properties are assumed as: the cohesive strength $T_0 = 3900$ MPa, the critical separation $\delta_0 = 0.0032$ mm and the ultimate separation $\delta_u = 0.016$ mm. Under the cyclic loading case, the two additional parameters are determined as $d_\Sigma = 10\delta_0$ and $n = 0.2$ respectively.

The simulation is carried out by using C(T) specimen through the 2D FE model as shown in Fig 5.3. Under mode I loading conditions, the crack tip field is symmetric to

the crack plane and only a half of the specimen has to be discretized. The width and height of the model is 50 mm and 30 mm, respectively. The thickness of the model is 12.5 mm. The initial crack length a_0 is 25 mm, as is the ligament length. The distance between the loading point and the top surface of the specimen is 10 mm. The type of continuum element is a CPE4 plane strain element. The cohesive elements are located along the ligament, and the size of the single element is 0.1 mm.

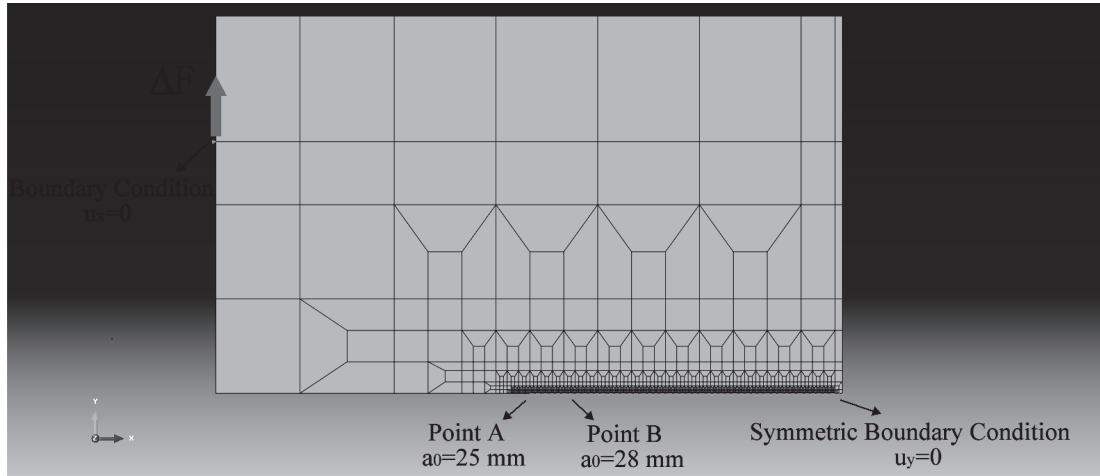


Figure 5.3: Finite element model of simulated compact tension specimen. The point A denotes the initial crack tip with a crack length $a_0=25$ mm. The point B has a distance with point A of 3 mm. The cohesive degradation and traction-separation response of those two points are compared.

In order to trace the local response of the material point along the crack growth path, the constant force-controlled loading condition is applied to ensure that the fatigue crack growth rates always increase. With the same loading ratio $R = 0.1$, two different force amplitudes are performed with $F_{\max} = 26$ kN and $F_{\max} = 17.5$ kN respectively. These two loading levels are corresponding to the initial stress intensity factor ranges $\Delta K_{\text{ini}} = 80.86$ $\text{MPa}\sqrt{\text{m}}$ and $\Delta K_{\text{ini}} = 54.42$ $\text{MPa}\sqrt{\text{m}}$ separately.

5.3.1 Traction response of high loading level

Figure 5.4 shows the traction-separation responses and the damage process of point A and point B with the loading level $F_{\max} = 26$ kN. Fig. 5.4(a) shows the relations between the traction and separation and Fig. 5.4(b) shows variation of local damage growth. The variation of the traction with the rising applied cycles are plotted in Fig. 5.4(c) and (d) for both points. Both axes are nondimensionalized.

Initially damage accumulates only at the initial crack tip (point A) where the combination of accumulated separation as well as the traction level is the largest. For the first loading segment, the traction-separation response follows the envelope curve as shown in Fig. 5.4(a). Due to a high applied load, the separation at the initial crack tip (point A) exceeds the critical separation δ_0 . Consequently, the monotonic damage starts to accumulate at the first loading segment, which is according to Eq. (5.3). As shown in Fig. 5.4(a) and (b), for the point A, the damage accumulation is $D = 0.23$ at the first loading segment

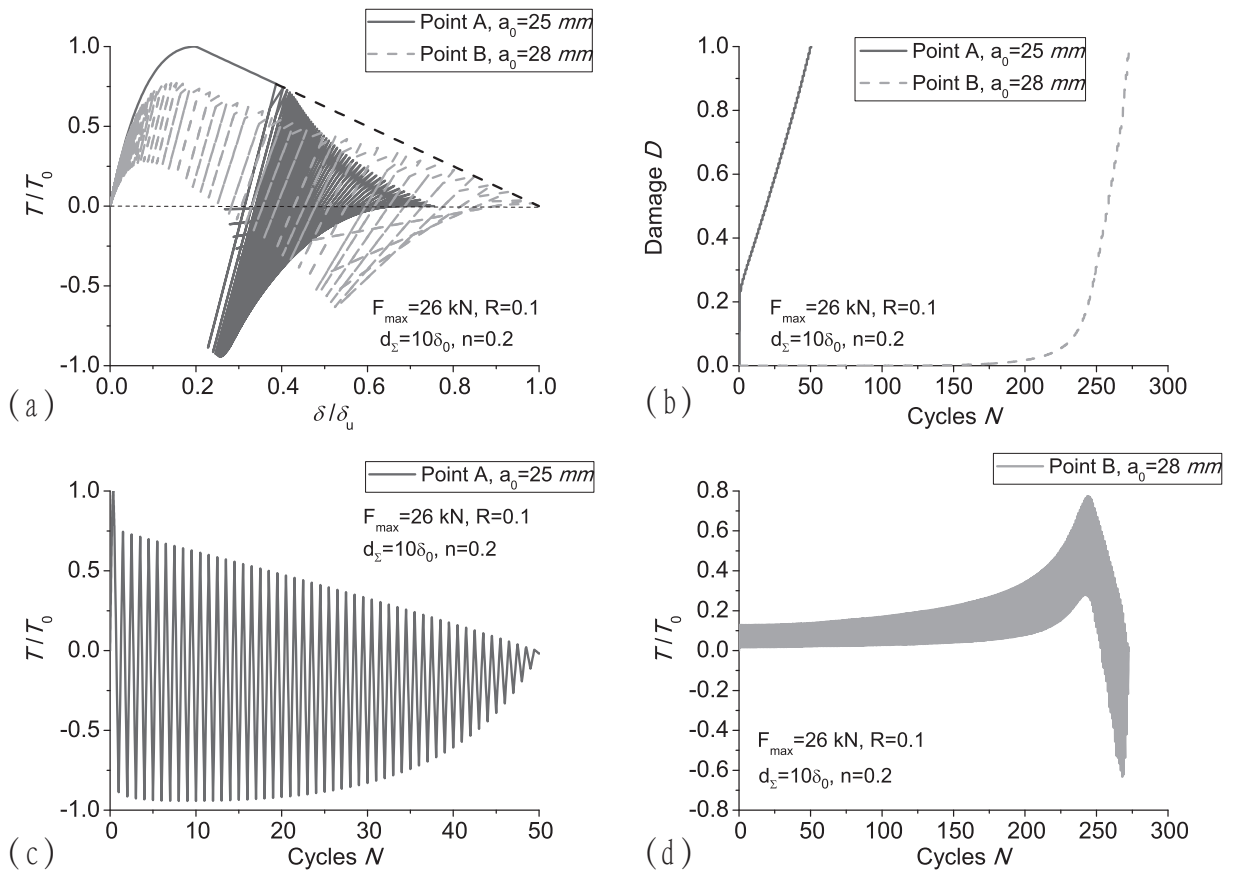


Figure 5.4: With the loading level $F_{\max} = 26 \text{ kN}$: (a) the traction-separation responses for both points; (b) the local damage evolution as functions of the loading cycles for both points; (c) the traction evolution as function of the loading cycles for point A; (d) the traction evolution as function of the loading cycles for point B.

and the cohesive traction is $T = 0.77T_0$. Comparing with Fig. 5.4(c) and (d), point A experiences the highest peak traction at the first loading segment while the traction of point B is still small, e.g. the traction of point B is only $12.8\%T_0$ at the first loading segment. Since the damage accumulation already sets in the first cycle, all subsequent cycles result in lower T values at point A, as shown in Fig. 5.4(c). For present cohesive parameters, point A loses its stress carrying ability completely after 50 cycles.

Point B experiences both lower accumulated separation and traction level which below the endurance limit, thus no damage accumulates at first 75 cycles. After total failure happens at the initial crack tip, a redistribution of traction occurs at the successive points as cycling progresses. Point B thus experiences increased traction. Finally, the traction surpasses the endurance limit and allows damage to initiate. The damage initiation of point B starts from the 76th loading cycle after which the maximal value of the achieved traction firstly increases up to $77\%T_0$ and then decreases with the increasing of the loading cycles until rupture. The final failure occurs at point B after 273 cycles. With increasing the loading cycle, the material separation increases. The final separation of point A is approximately $0.7\delta_u$ while the value of final separation of point B is very close to δ_u .

5.3.2 Traction response of low loading level

Figure 5.5 shows the traction-separation responses and the damage process of point A and point B with the loading level $F_{\max} = 17.5$ kN. The material separation processes are similar to the one occurring with the high loading level, only that damage accumulation sets in at a higher number of loading cycles. The traction of point A in all subsequent cycles is lower than the traction achieved at the first loading segment while the traction of point B increases firstly, after a maximal value achieved then decreases, as shown in Fig. 5.5(c) and (d). The separation of the final failure at point B is $0.53\delta_u$ which is greater than the value at point A, $0.27\delta_u$, as shown in Fig. 5.5(a).

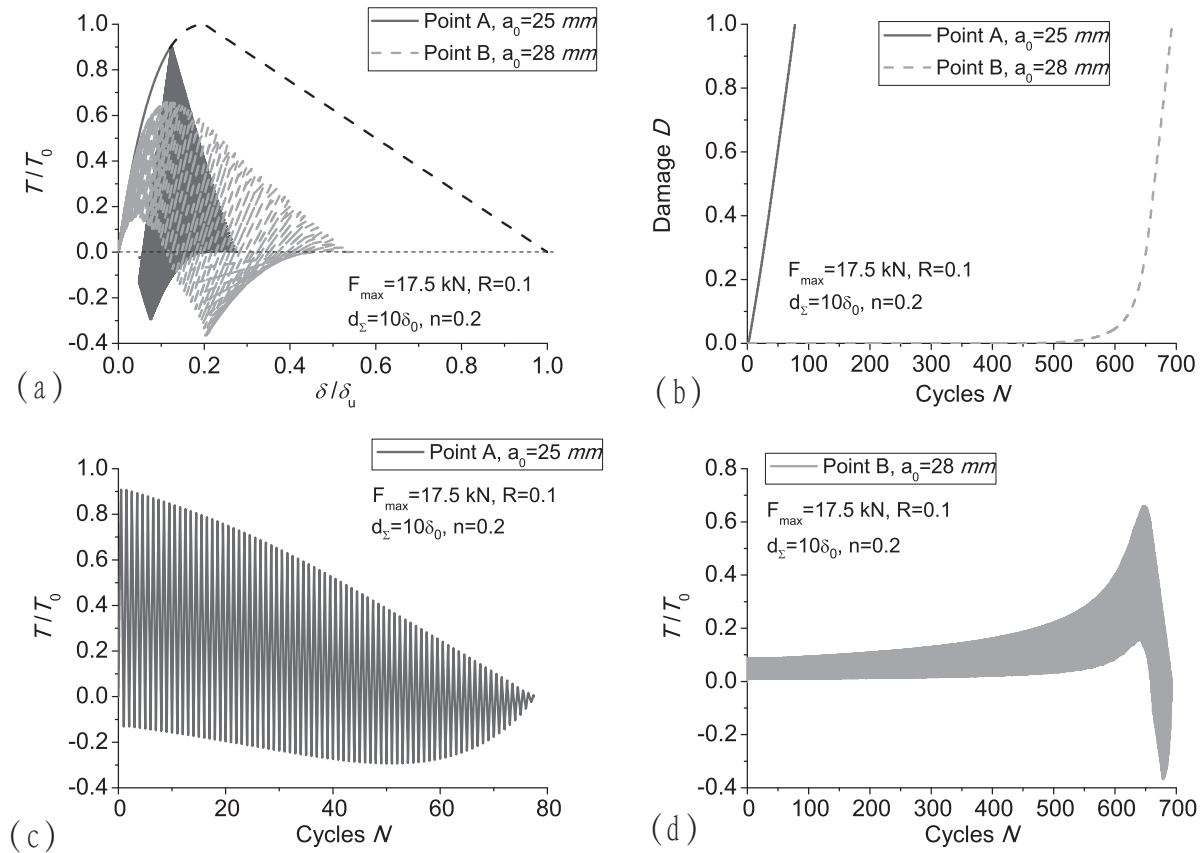


Figure 5.5: With the loading level $F_{\max} = 17.5$ kN: (a) the traction-separation responses for both points; (b) the local damage evolution as functions of the loading cycles for both points; (c) the traction evolution as function of the loading cycles for point A; (d) the traction evolution as function of the loading cycles for point B.

For both loading levels, the cyclic traction-separation responses is always restricted within the envelope curve. The reason has been explained in section 4.3. A significant different of the traction-separation responses is that due to a lower loading level, the separation at the initial crack tip (point A) is smaller than δ_0 , thus no monotonic damage accumulation occurs at the first loading segment. The damage initiates always at the initial crack tip (point A). For the low loading level, the damage accumulation starts from

the 4th cycle. The similarity in the separation processes for both loading levels clearly indicates that material separation processes are distinctly different during crack initiation and crack propagation for which a steady state is reached.

With the high loading level, the final failure of the two points are at the 50th cycle and at the 273th cycle. With the low loading level, the final failure of the two points are at the 79th cycle and at the 696th cycle. The interval between the final failure of the two points is shorter with the high loading level than with the low loading level, as shown in Fig. 5.4(b) and 5.5(b). This implies that the crack grows at a faster rate with the high loading. The Δa vs. N curves for the two loading cases are depicted in Fig. 5.6(a). The da/dN vs. ΔK are presented in Fig. 5.6(b).

5.3.3 Fatigue crack growth rate (da/dN vs. ΔK) prediction

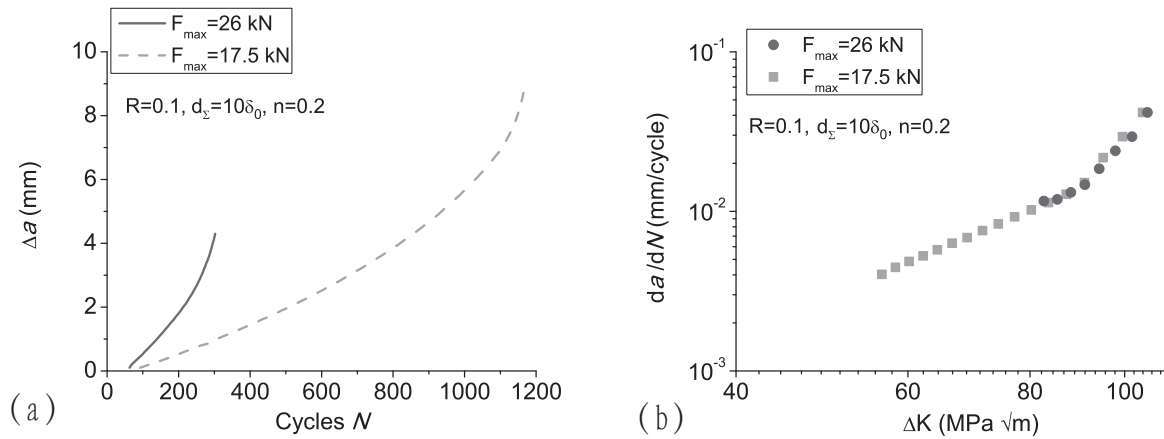


Figure 5.6: With two loading levels, (a) the fatigue crack extension curves (Δa vs. N); (b) the fatigue crack growth rate curves (da/dN vs. ΔK).

In Fig. 5.6(a), the crack extension Δa is plotted as a function of number of applied load cycles, N . The larger the applied load requires the smaller number of cycles for crack initiation. The corresponding da/dN vs. ΔK curves are presented in Fig. 5.6(b) in which the complete crack growth rate curve is assembled through high and low loading levels. The stress intensity factor can be calculated according to Eq. (3.1). The fatigue crack growth rate da/dN is approximately by the slope of Δa vs. N curves. To avoid "numerical noise", crack growth rate da/dN is obtained by the interval of every four points on the crack extension curves (Δa vs. N), in terms of $(\Delta a_{i+5} - \Delta a_i)/(N_{i+5} - N_i)$ with $(N_i, \Delta a_i)$ is the coordinate of the point on the crack extension curve. The minimal difference of $(\Delta a_{i+5} - \Delta a_i)$ is limited by the cohesive element length. Several convergence studies [98, 112, 124] have been performed to investigate the dependence of the predicted CCZM on the size of cohesive elements. The results convince that the influence of the element size is negligible. With increment of the crack length, the fatigue crack growth rate is accelerated and enters into Regime III progressively.

5.3.4 Parametric study

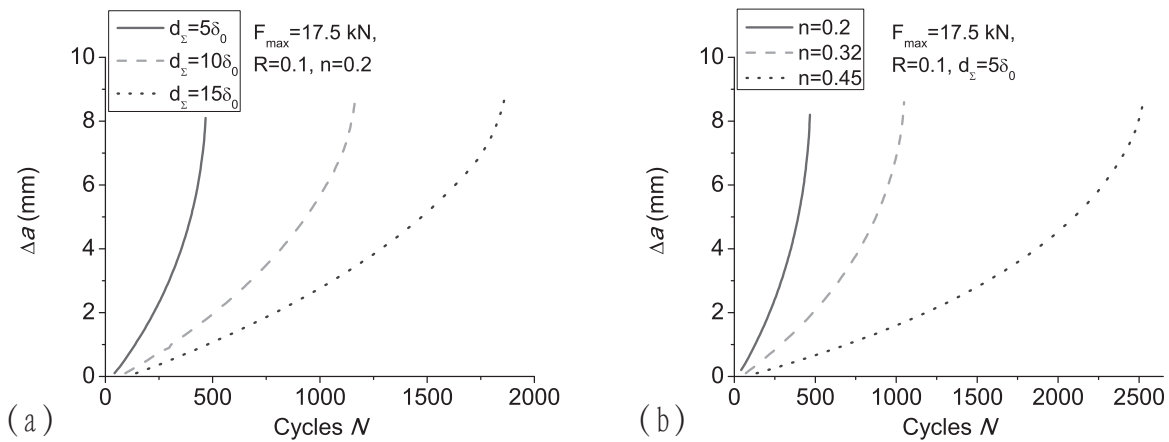


Figure 5.7: With the loading level $F_{\max} = 17.5$ kN, the effect of (a) the accumulative length d_{Σ} with $n = 0.2$ and (b) n with $d_{\Sigma} = 5\delta_0$ on the fatigue crack extension curves (Δa vs. N).

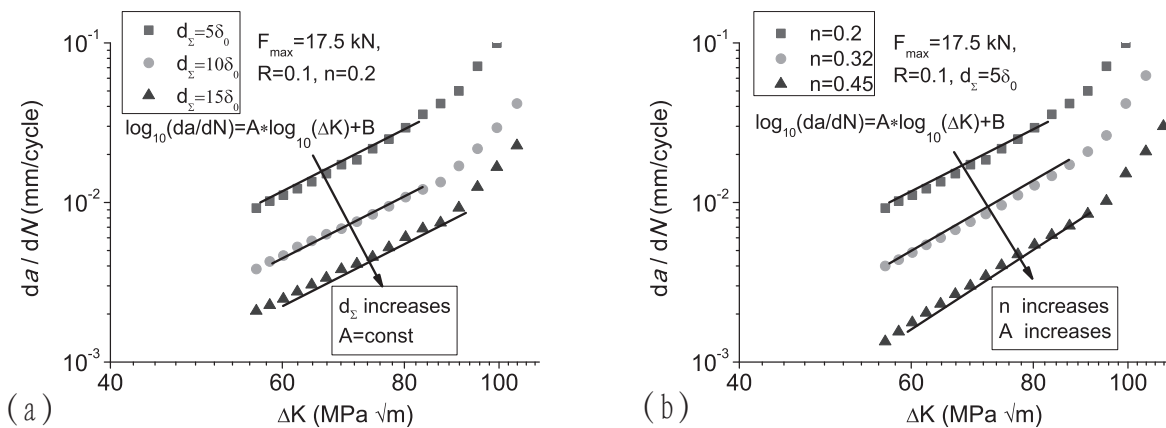


Figure 5.8: With the loading level $F_{\max} = 17.5$ kN, the effect of (a) the accumulative length d_{Σ} with $n = 0.2$ and (b) n with $d_{\Sigma} = 5\delta_0$ on the fatigue crack growth rate curves (da/dN vs. ΔK).

The identification of the effects of the model parameters are also performed under the constant force amplitude at the loading ratio $R = 0.1$ with the loading level $F_{\max} = 17.5$ kN. Fig. 5.7(a) shows the effect of the accumulative length d_{Σ} for the crack extension curves and Fig. 5.8(a) presents the corresponding fatigue crack growth rate curves. In Fig. 5.7(a), under a given crack growth length Δa , the fatigue growth life increases with rising the value of d_{Σ} . The larger value of d_{Σ} slows down the crack growth rate da/dN at a given ΔK with the same value of n . As shown in Fig. 5.8(a), the general trend appears that d_{Σ} -based curves are parallel to each other when other parameters remain unchanged. The accumulative length d_{Σ} acts like the intercept coefficient C operates in Paris' equation

of Eq. (1.1). Fig. 5.7(b) shows the effect of n for the crack extension curves and Fig. 5.8(b) are the corresponding fatigue crack growth rate curves. The higher value of n correlates with the lower crack growth rate da/dN under the same loading condition. In contrast, the slope of the da/dN vs. ΔK curves becomes steeper while increasing the value of n , as shown in Fig. 5.8(b). The effect of n acts like the power value m in Paris' equation. The crack growth rate are accelerated inevitable as the loading level approaches the critical value at failure.

5.3.5 Excluding the monotonic damage variable

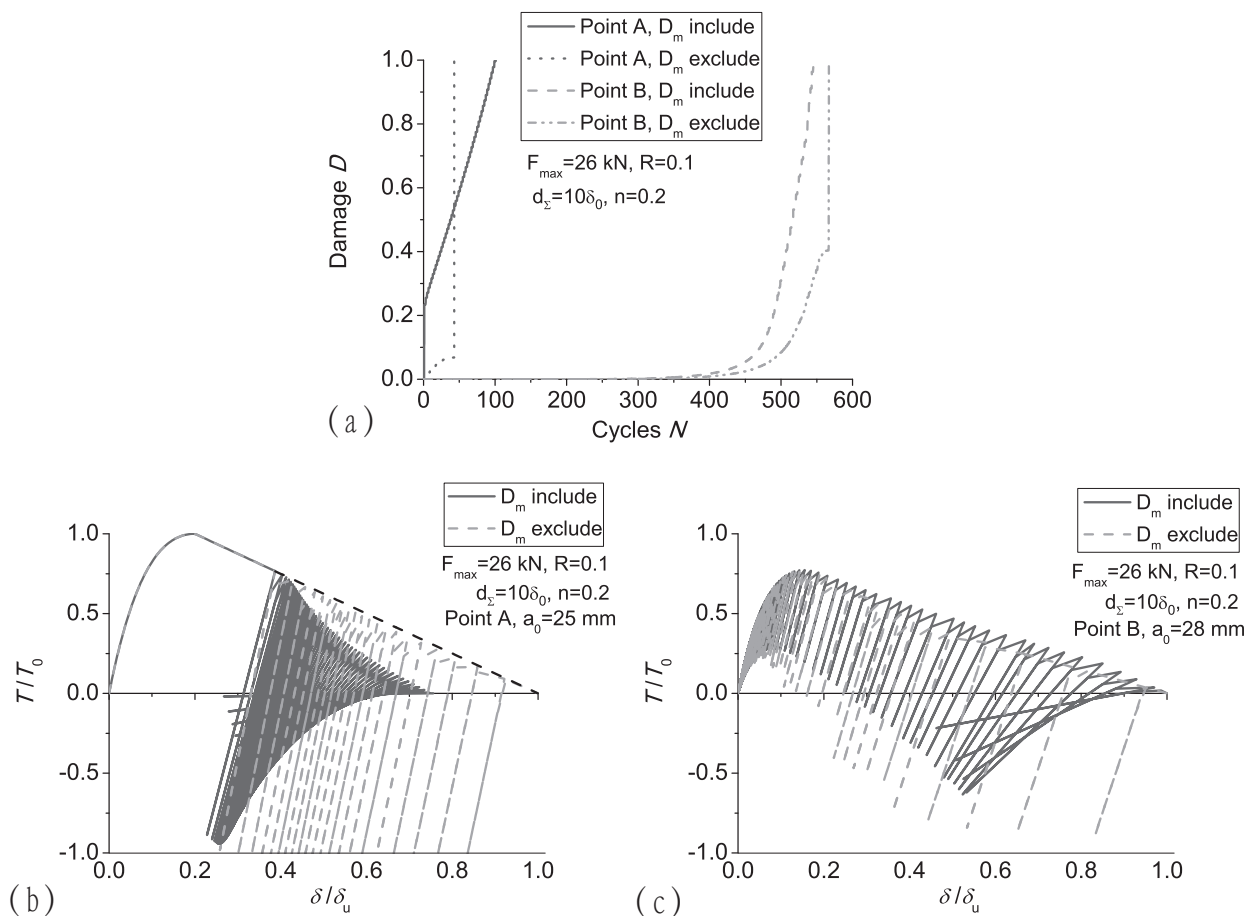


Figure 5.9: Include and exclude the monotonic damage, (a) the local damage evolution as functions of the loading cycles for both points; (b) the traction-separation responses for point A; (c) the traction-separation responses for point B;

Figure. 5.9 shows the differences of damage accumulation process including and excluding the monotonic damage. For the point A, due to the high applied load, the traction has exceeded the maximum traction at the first loading segment. Should the monotonic damage is not considered, final failure happens when the damage accumulation is even smaller than 0.1. The reason would be mainly due to the high initial stiffness and no damage accumulation on the envelop curve. Since the monotonic damage is excluded, the unloading

stiffness at the first loading segment is the same as the initial stiffness. In this case, due to the endurance limit, the damage accumulation at initial loading cycles is very small. However, at the first loading segment, the separation at point A already exceeds the critical separation δ_0 . Consequently, the separation of point A reaches the ultimate separation δ_u in very few loading cycles. In this case, the final rupture occurs suddenly even with very low damage accumulation. Should the monotonic damage is not considered, the damage accumulation process at point B also shows discontinuity. Since no damage accumulates on the envelop curve, the separation of point B increases with cyclic loading but the damage increment is small. Finally, when the separation of point B reaches δ_u , the damage is still smaller than 1.0 and a sudden failure happens. Numerical results shown in Fig. 5.9 denote that including the monotonic damage variable in CCZM is essential especially for low cycle fatigue predictions.

5.4 Verification based on fatigue experiments

After the model validation have been examined, the crack propagation analyses are performed based on the experimental data. Both fracture tests and fatigue tests are used for determination of cohesive model parameters under monotonic and cyclic loading. Two materials, S460 and AISI304 are applied for the tests. The stress-strain curves for both materials are according to Fig. 5.10(a) and 5.12(a) respectively. The material properties of S460 have been introduced in section 4. The material properties of AISI304 are as follows: Young's modulus $E = 200$ GPa, Poisson ratio $\nu = 0.3$, the initial yield strength $\sigma_y = 230$ MPa and the ultimate strength $\sigma_u = 650$ MPa, according to Eq. (4.3) the bulk modulus $K = 1558$ MPa and the strain hardening exponent $n = 0.87$.

The monotonic cohesive law can be constructed through the cohesive strength T_0 , the critical separation δ_0 and the cohesive energy Γ_0 . To obtain cohesive energy Γ_0 , the value of J -integral at crack initiation J_i has to be determined. According to the experimental results, the corresponding J_i values under plane strain conditions of those two materials are $J_i = 270.1$ N/mm for S460 and $J_i = 728.9$ N/mm for AISI304 [98]. For those two metallic materials which are with high ductility, severe plastic deformation occurs at crack initiation.

The cohesive strength T_0 and the critical separation δ_0 are determined according to the load-line displacement curves of notched tensile specimens or cracked specimens. The relation between the cohesive strength T_0 and the critical separation δ_0 can be attributed to the effect of the initial cohesive stiffness k , which is defined in Eq. (6.3). The choice related to k should guarantee that the cohesive zone does not influence the overall compliance before the damage initiation, normally a higher k is recommended [54].

Fracture simulations are performed in C(T) specimens to determine the cohesive strength. Due to symmetry, only one half of the specimen is modeled. The cohesive zone is predefined along the crack growth path through the specimen ligament with the cohesive element length of 0.1 mm. The CPE4 elements are used for the continuum elements. For both materials, several C(T) specimens with different initial crack lengths around 25 mm are tested. After a series numerical experiments, the cohesive parameters for both materials are determined as following: for S460, the cohesive strength $T_0 = 1585$ MPa, the critical separation $\delta_0 = 0.014$ mm, the ultimate separation $\delta_u = 0.164$ mm of Eq. (5.5) for half FE model and the corresponding cohesive stiffness $k \cong 3.0 \times 10^5$ N/mm³; for

AISI304, the cohesive strength $T_0 = 1330$ MPa, the critical separation $\delta_0 = 0.018$ mm, the ultimate separation $\delta_u = 0.468$ mm of Eq. (5.5) for half FE model and the corresponding cohesive stiffness $k \cong 2 \times 10^5$ N/mm³. The computations from the cohesive model give reasonable predictions with the experiments.

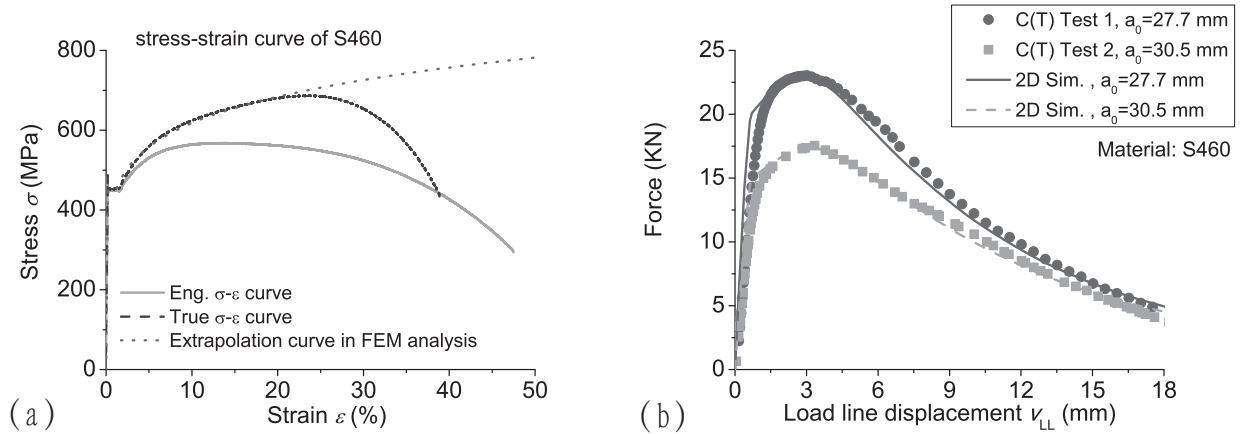


Figure 5.10: Material S460, (a) stress-strain curve; (b) experimental and simulated load-line displacement curves of side-grooved C(T) specimens for determination the monotonic cohesive parameters.

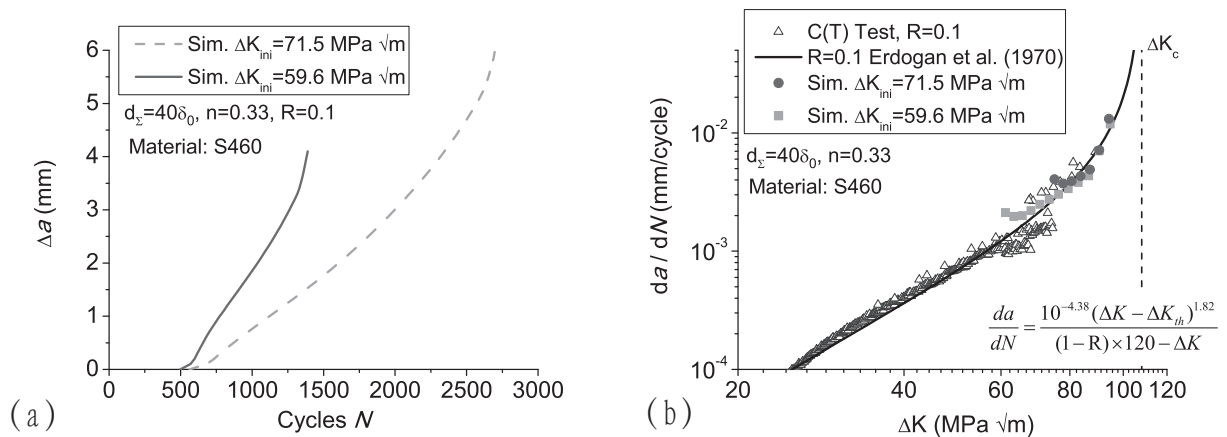


Figure 5.11: Material S460, (a) the fatigue crack extension curves (Δa vs. N) with two different initial stress intensity factor under $R = 0.1$; (b) comparison between the experimental and simulated fatigue crack growth rate curves (da/dN vs. ΔK) relating to two different initial stress intensity factor under $R = 0.1$.

With the monotonic cohesive parameters, the cyclic cohesive model parameters can be identified according to the fatigue crack growth rate test results. Erdogan model [27] as defined in Eq. (3.4) is presented additionally to compare with the experimental results for both materials. The material constants for S460 have been determined in Chapter 3, see Fig. 3.4. The material constants for AISI304 are $C = 10^{-5.763}$, $m = 2.72$, with the fracture

toughness $K_c = 110 \text{ MPa}\sqrt{\text{m}}$ and the threshold value $\Delta K_{\text{th}} = 7.0 \text{ MPa}\sqrt{\text{m}}$ [98]. For S460, two constant force amplitude with the initial stress intensity $\Delta K_{\text{ini}} = 59.6 \text{ MPa}\sqrt{\text{m}}$ and $\Delta K_{\text{ini}} = 71.5 \text{ MPa}\sqrt{\text{m}}$ are performed respectively. For AISI304, three constant force amplitude with the initial stress intensity $\Delta K_{\text{ini}} = 52.48 \text{ MPa}\sqrt{\text{m}}$, $\Delta K_{\text{ini}} = 66 \text{ MPa}\sqrt{\text{m}}$ and $\Delta K_{\text{ini}} = 75.81 \text{ MPa}\sqrt{\text{m}}$ are performed. For both materials, the loading ratio is $R = 0.1$ and the constitutive relation governing the deformation behavior of the bulk material is based on the J_2 Mises plasticity. Numerical trials show that for S460, the cyclic parameters are $d_\Sigma = 40\delta_0$ and $n = 0.33$; for AISI304, the cyclic parameters are $d_\Sigma = 36\delta_0$ and $n = 0.35$. Fig. 5.11(b) and 5.13(b) denote that the simulated fatigue crack growth rate curves give good predictions with the experimental data.

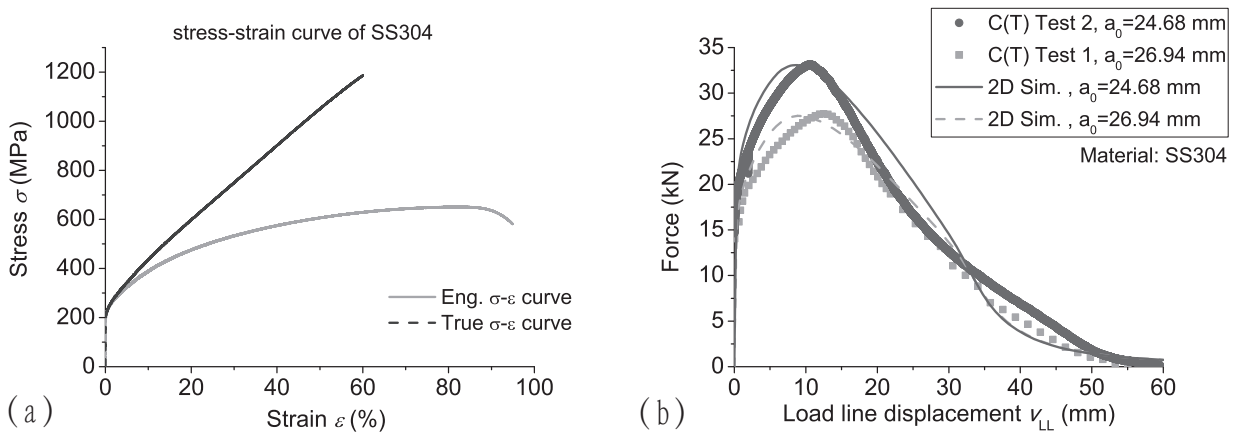


Figure 5.12: Material AISI304, (a) stress-strain curve; (b) experimental and simulated load-line displacement curves of C(T) specimens for determination the monotonic cohesive parameters.

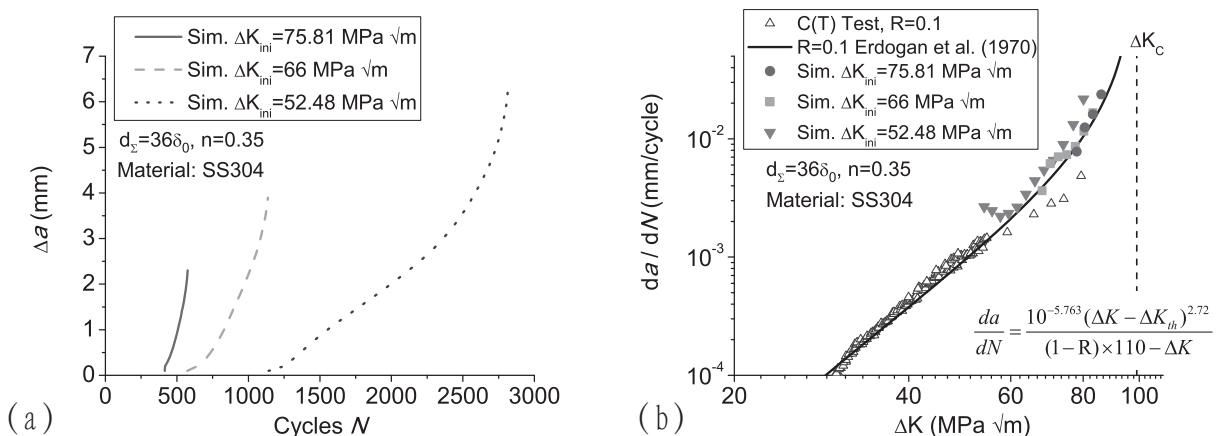


Figure 5.13: Material AISI304, (a) the fatigue crack extension curves (Δa vs. N) with three different initial stress intensity factor under $R = 0.1$; (b) comparison between the experimental and simulated fatigue crack growth rate curves (da/dN vs. ΔK) relating to three different initial stress intensity factor under $R = 0.1$.

For both materials, the simulated fatigue crack growth rate curves under different loading ranges have an overlapping part. This is reasonable based on the Paris' law. Although the simulated fatigue crack growth rate curve shows a good accordance with the experimental results, varying crack growth rate occurs during the lower loading case for both materials. In Fig. 5.11(b) and 5.13(b), for the lower loading case, the simulated crack growth rate is initially fast, after which it shows down to a normal level. No direct evidence shows the exact reason. One possibility is that the crack driving force is not stable initially. After this, the fatigue crack growth becomes increasingly fast until the fracture toughness range of the material is approached. The fatigue crack growth rate is accelerated before approaching the critical $\Delta K_c = (1 - R)K_c$. The simulation results are assembled with the lower loading level and the higher loading level. The computational results agree with experimental data in Regime III. The new cyclic cohesive zone model provides reliable computational prediction very near to K_c , so that the present cyclic cohesive zone model builds a uniform model for both fatigue and fracture crack simulation.

5.5 Summary

In the present work, a new CCZM for monotonic and cyclic crack growth is introduced. The major concern of the present work is attempting to establish a cohesive model to describe fatigue crack growth with both low and high growth rates, especially fatigue cracks in Regime III. For characterizing material degradation, a scalar damage variable is defined based on both monotonic damage as well as cyclic damage. Interactions of the monotonic damage and cyclic accumulative damage are considered in the damage evolution.

The material degradation under monotonic loading is represented by softening in the cohesive law, whereas the cyclic damage is described by an additional damage evolution equation. Both damage evolutions have been verified by experiments and can characterize material damage around the crack-tip properly. The monotonic model parameters include the cohesive energy Γ_0 and the cohesive strength T_0 , which are determined from the monotonic fracture tests. The experimental data obtained from fatigue tests are used to identify the cyclic model parameters.

Detailed finite element computations confirm that the proposed CCZM is able to describe both rupture and fatigue crack growth properly. The model gives a uniform characterization of Regime II and Regime III in the fatigue crack diagram.

6 Stress-triaxiality-dependent cyclic cohesive zone model

6.1 Introduction

Monotonic ductile fracture mechanism involves micro-cracks or micro-voids nucleation, leading to failure by cleavage, inter-granular cracking or coalescence. It has been discussed in Chapter 4 that the resistance against initiation of ductile crack growth and crack propagation depends on the geometrical constraint. The stress-state is characterized by a triaxiality parameter, η , which is defined as the ratio between the hydrostatic stress and the effective stress. The stress-state plays a key role in the damage growth till failure. In the low cycle fatigue regime, the material damage process also behaves similar to those of ductile fracture. Corresponding mechanisms under cyclic loads involve the repetitive blunting and resharping of crack tip driven by localized plastic deformation and therefore must depend on the stress-state as well.

Extensive discussions of the geometrical effect on fatigue crack propagation have been proposed in Chapter 3. The experiments were performed on C(T) specimens with different thicknesses. Experimental results show obvious geometrical dependence during elastoplastic fatigue crack growth. According to the beach marking, larger curvature of the crack profiles is obtained from the thin specimen (i.e. $B/W = 0.08$) than that from the thick specimen (i.e. $B/W = 0.25$). Furthermore, severe plastification occurs with the high rate of fatigue crack growth approaching Regime III. In that case, the thin specimen would be fully-yielded so that the crack growth rate at the middle plane shows obviously retardation. The deviation of da/dN curves of different thickness specimens emerges at high stress intensity level, as shown in Fig. 3.24. Experimental evidence which showed that the stress-state has a significant effect on fatigue crack propagation also reported in [134].

The application of cyclic cohesive zone model (CCZM) in predicting fatigue crack growth in ductile materials has been introduced in Chapter 5. Since the low cycle fatigue crack growth depends on the geometrical constraint, it would be essential to account for the effect of stress-state on the CCZM.

6.1.1 State of art of constraint dependent CCZM

so far, very few literatures have been reported concerning the constraint effect on cyclic cohesive zone modeling. Jha and Banerjee [135] introduced the triaxiality dependent behavior of cohesive parameters, which was proposed in [61], combining with Roe-Siegmund model for fatigue life analysis. In the model, the influence of triaxiality was only on the cohesive envelop but not involved in the damage evolution law. Two-dimensional simulations were performed under two kinds of stress-state conditions. Numerical results revealed that initiation and growth of damage is more rapid with increasing constraint. It should

be noted that in the work of [135], the numerical results only provided some fatigue failure trends, and no experimental comparison was included.

Cao and Vormwald [136] proposed a triaxiality dependent CCZM. The correlations between the cohesive parameters and the stress triaxiality were obtained from GTN model, as presented in [93]. The model was used to reproduce the fatigue crack initiation and fatigue crack growth in two-dimensional case. The predictive simulations of the model were implemented to investigate C(T) and M(T) specimens, which represent different triaxiality conditions. However, by using an unique set of parameters, the predictive results of M(T) specimen show obvious deviation from the experimental data. In addition, the triaxiality dependent cohesive parameters were obtained based on the numerical results from the GTN model. It is not legal to identify material model parameters from another models.

6.1.2 Motivation

As discussed in Chapter 4, for a three-dimensional cracked specimen, the ratio of the plastic zone size to the specimen thickness plays an important role, which can be interpreted as the effect of the specimen thickness to the crack front field, i.e. the out-of-plane constraint. It has been confirmed that the out-of-plane constraint is mainly a manifest of the loading configuration to the crack tip field. To study the details of these in-plane and out-of-plane constraint effects, it is required to conduct detailed three-dimensional FE analysis of fracture specimen. Moreover, numerical results obtained in three-dimensional computations would give a detailed understanding of the local failure process.

In the present work, by considering the influence of the stress-state effect on the cohesive law and the damage evolution equation, a stress-triaxiality-dependent cyclic cohesive zone model (TCCZM) is proposed. The TCCZM is an extended work following the proposed CCZM for both fatigue and fracture in Chapter 5. The stress triaxiality dependent cohesive parameters involved in the model are obtained based on the experimental results which have been presented in Chapter 4. Furthermore, the new TCCZM is applied to reproduce the fatigue crack growth of different specimens in three-dimensional FE computations.

6.2 Stress-triaxiality-dependent cyclic cohesive zone model

The overall mechanical behavior and the corresponding cohesive properties for monotonic stress-state dependence of the cohesive law have been discussed. As presented in Chapter 4, the correlations of the stress triaxiality and the cohesive parameters, $\Gamma(\eta)$ and $T_{\max}(\eta)$, are suggested in Eq. (4.7) and Eq. (4.8) respectively.

The cohesive law in monotonic case provides an envelop line when cyclic loading occurs. In the fatigue process, the material load carrying capacity will degrade gradually with damage accumulation. In the CCZM, this feature is related to the cohesive strength and the normal stiffness. The constitutive behavior of the CCZM has been proposed in Chapter 5. The extension of the CCZM is including the stress triaxiality effect, therefore, the influence of the stress triaxiality on the damage evolution needs to be considered.

6.2.1 Monotonic damage evolution

As specified in Chapter 5, the total damage is contributed by two parts, the monotonic damage and the cyclic damage. The expression of the monotonic damage variable, D_m , is related to δ_0 and δ_u . Note that by integrating the stress triaxiality effect, the ultimate separation in the cohesive zone can be expressed in terms of $\Gamma(\eta)$ and $T_{\max}(\eta)$, as defined in Eq. (4.2). Should δ_0 be independent of η , following Eq. (5.3), the stress triaxiality dependent monotonic damage variable can be thus defined as

$$D_m(\eta) = \frac{\delta - \delta_0}{\delta_u(\eta) - \delta_0}. \quad (6.1)$$

6.2.2 Cyclic damage evolution

The cyclic damage variable is included in the CCZM to describe the local deterioration of the material. As defined in Eq. (5.6), the current cohesive strength decreases with the damage indicator which represents the material degradation. Eq. (4.8) has denoted that the cohesive strength is stress triaxiality dependent. Therefore, one can formulate the stress triaxiality dependent cyclic damage variable directly by substituting the constant cohesive strength, T_0 , with $T_{\max}(\eta)$, as

$$\dot{D}_c(\eta) = \frac{\dot{\delta}}{d_\Sigma} \left(\frac{T}{T_{\max}(\eta)(1-D)} - n \right) H(\delta_{acc} - \delta_0), \quad \dot{D}_c(\eta) \geq 0. \quad (6.2)$$

The two cyclic cohesive parameters, the accumulative length d_Σ and the damage controlling parameter n , have been discussed in Chapter 5. In the present investigation, those two parameters are assumed to be stress triaxiality independent.

Furthermore, under cyclic loading process, the un/reloading stiffness can be defined as

$$k(\eta) = \frac{T_{\max}(\eta)(1-D)e}{\delta_0}. \quad (6.3)$$

The loading path for a ductile material follows a linear correlation as defined in Eq. (5.8), by substituting k with $k(\eta)$.

6.2.3 Operating mechanism of the TCCZM

a. Stress triaxiality influence in the un/reloading process

An important point should be noted that the application of the stress triaxiality dependent behavior in the CCZM is a crucial aspect. The stress triaxiality dependent correlations obtained in Chapter 4 are appropriate only for the monotonic loading condition. If the correlations are applied for the cyclic loading, the first problem is how to consider the stress triaxiality influence in the un/reloading process. In fact, in the un/reloading process, it is still an open topic how the stress triaxiality influences the cohesive parameters.

According to Eq. (4.2), the ultimate separation $\delta_u(\eta)$ changes with the stress triaxiality. In the un/reloading process, the absolute separation δ and the ultimate separation $\delta_u(\eta)$ will vary simultaneously, which may induce severe numerical problems. Therefore, in the present work, a simple method is suggested. The stress triaxiality will affect the envelop curve only. This assumption should be reasonable since the envelop curve in the CCZM

describes the monotonic failure process, whereas the un/reloading path in the CCZM characterizes the cyclic failure process. It is believable that the ductile failure of the whole damage process should be mainly contributed by the monotonic failure. In this case, the stress triaxiality effect also should be mainly on the monotonic failure, which is represented by the envelop curve in the CCZM. The stress triaxiality value is assumed to keep constant in the un/reloading process.

b. Stress triaxiality effect zone

However, another problem has to be considered in predicting fatigue crack growth. The response of the cohesive zone in the first loading step will comply with the monotonic cohesive law. Then, the stress triaxiality value is assumed to keep constant in the following un/reloading process. How to include the stress triaxiality variation during fatigue crack propagation is unclear. Here, to consider the stress triaxiality variation, one has to define a stress triaxiality effect zone before applying the TCCZM, as shown in Fig. 6.1.

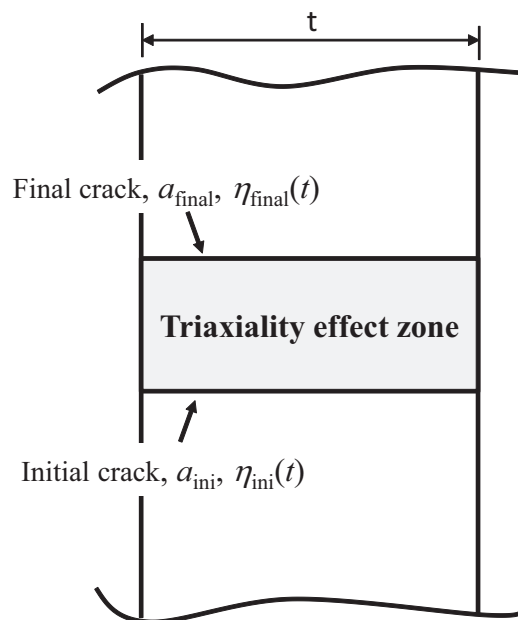


Figure 6.1: Illustration of the stress triaxiality effect zone.

Generally, for a pre-cracked specimen, the initial crack position is known. Then, the length of the stress triaxiality effect zone can be considered as the expected crack propagation length in the prediction. In this case, the expected final crack position can be determined. By applying the maximum load (i.e. maximum force/displacement) of the cyclic loading amplitude, the stress-state of the initial crack and the final crack can be evaluated respectively through FE computations, as specified in Chapter 4. It would be simple for two-dimensional computations since the crack positions can be identified easily in a planar FE model. For the three-dimensional FE model, it is necessary to firstly presume the final crack front in the thickness direction. Note that the FE models adopted in calculating the stress-state should not consider the crack propagation, which means the cohesive elements are not included. Since the stress triaxiality values of the initial crack and the final crack are known, if the fatigue crack propagation is controlled by constant

force/displacement loading amplitude, one can evaluate the corresponding stress triaxiality value of an arbitrary position within the effect zone through interpolating. Therefore, it is important that the size of the effect zone should be adequate to ensure a constant cyclic loading amplitude within the zone. Otherwise, it would be inaccurate to obtain the stress triaxiality value of an arbitrary position through interpolating.

According to the aforementioned method, for each position within the effect zone, a unique stress triaxiality value can be calculated under the condition of applying the maximum load. Obviously, it is reasonable to use this unique stress triaxiality value to identify the stress triaxiality dependent cohesive parameters for each position.

In sum, the stress triaxiality effect zone is considered as the expected fatigue crack propagation area in the prediction; the stress triaxiality variation during fatigue crack propagation is carried out through calculating the corresponding stress triaxiality dependent cohesive parameters for each position within the effect zone. Following this suggestion, for each position, the corresponding stress triaxiality dependent cohesive parameters are applied in the TCCZM.

6.3 Model verification

The TCCZM has been implemented in the commercial finite element code ABAQUS [71] by using of the cohesive element coupled with UMAT subroutine. The fatigue damage is calculated for every time increment. To verify the proposed model, three-dimensional fatigue crack propagation analysis will be performed. The predicted local crack growth rates and the crack profiles will be verified with the experimental data. As presented in Chapter 3, the beach markings and the curvatures of the crack profiles during fatigue crack propagation have been obtained from the fatigue tests.

Considering the computational cost of three-dimensional cyclic loading analysis, present investigation will only focus two adjacent crack profiles. One beach marking from the experiment is taken as the initial crack profile. The expected crack propagation is until the subsequent beach marking which is referred as the final crack profile. The region between the two beach markings can be considered as the stress triaxiality effect zone. Numerical predictions of the fatigue crack propagation will be terminated when the predicted middle crack extension reaches the final crack position.

Material S460 was used in the experiments and the stress-strain response has been described in Eq. (4.3). In all computations, 8-nodal isoparametric elements with full integration are used for the continuum elements. Due to symmetry in mode I loading conditions, only one-quarter of each specimen is modeled. The cohesive elements are arranged on the ligament plane to simulate the crack extension. The bulk material for the continuum elements is described by the classical J_2 theory. The correlations between the stress triaxiality and the cohesive parameters of S460 has been identified in Eq. (4.7) and Eq. (4.8) respectively. The two cyclic parameters in Eq. (6.2) have been determined in 2D plane strain case in chapter 5, with $d_\Sigma = 40\delta_0$ and $n = 0.33$ respectively.

6.3.1 Verification based on C(T) fatigue crack propagation

The model will be verified based on the fatigue experiments of C(T) specimens. For a stable crack propagation, experimental results (i.e. Fig. 3.23) showed similar crack growth

rate at the free surface and the middle plane for C(T) specimen with $B/W = 0.25$. The average stress intensity value, which is defined as $\Delta K_{\text{avg}} = (\Delta K_{\text{ini}} + \Delta K_{\text{final}})/2$, is used to represent the stress intensity range between the two adjacent cracks. The stress intensity factor is calculated according to Eq. (3.1) with the length of the middle crack.

a. The loading configuration and the FE model

The dimensions of the C(T) specimen have been illustrated in Fig. 3.2(a). The specimen thickness is $B = 12.5$ mm with a width of $W = 50$ mm. With the same loading ratio $R = 0.1$, two constant force amplitudes are performed with $F_{\text{max}} = 10$ kN and $F_{\text{max}} = 18.75$ kN respectively.

Requirements of applying TCCZM include to obtain the corresponding stress triaxiality values within the effect zone. With the maximum force applied, the distributions of the stress triaxiality along the initial crack and the final crack are calculated firstly. Three-dimensional FE models without cohesive elements are carried out for the computations. The element meshes are in compliance with the beach markings. At the crack front, the smallest element length in the crack extension direction and the height direction is 0.01 mm. It has been confirmed in Chapter 3 that the SSY conditions are valid for the most fatigue crack growth stages. Accordingly, the J -integral is evaluated according to $J = (1 - \nu^2)K^2/E$. The stress triaxiality values along the crack front are taken at a distance of $r = J/\sigma_y$. Then, the corresponding stress triaxiality value of an arbitrary position within the effect zone is evaluated through interpolating.

Three-dimensional FE configurations for predicting fatigue crack propagation of C(T) specimens are generated in compliance with the initial crack front. The size of the regular small elements in crack extension direction is 0.04 mm. Fifteen layers of elements with a bias ratio of 20.0 are used through the half section thickness.

b. Predictions at low loading level

For the loading level $F_{\text{max}} = 10$ kN, the beach markings of the initial crack and the final crack are shown in Fig. 6.2(a). The middle crack extension is $\Delta a = 1$ mm and the surface crack extension is $\Delta s = 1.06$ mm. The corresponding average stress intensity range is $\Delta K_{\text{avg}} = 47.4 \text{ MPa}\sqrt{\text{m}}$ and the interval cycles obtained from the experiment between the two cracks are $\Delta N^{\text{exp}} = 1339$.

• Numerical results

Figure 6.2(b) shows the detailed final crack profile comparisons between the numerical predictions with the experiments. The numerical result from CCZM shows agreement with the experiment only in 50% of the thickness from center to surface. Then the predicted crack profile decreases significantly towards the surface. However, with the consideration of stress triaxiality effect, the numerical result from TCCZM shows much better agreement with the experiment of the whole crack profile.

According to the predicted crack profiles, the local crack growth rates can be calculated, as shown in Fig. 6.3(a). At the middle plane, due to the dominance of the plane strain conditions, the predicted crack growth rates from both models agree with the experimental result. At the free surface, the predicted crack profile from TCCZM is coincident with the

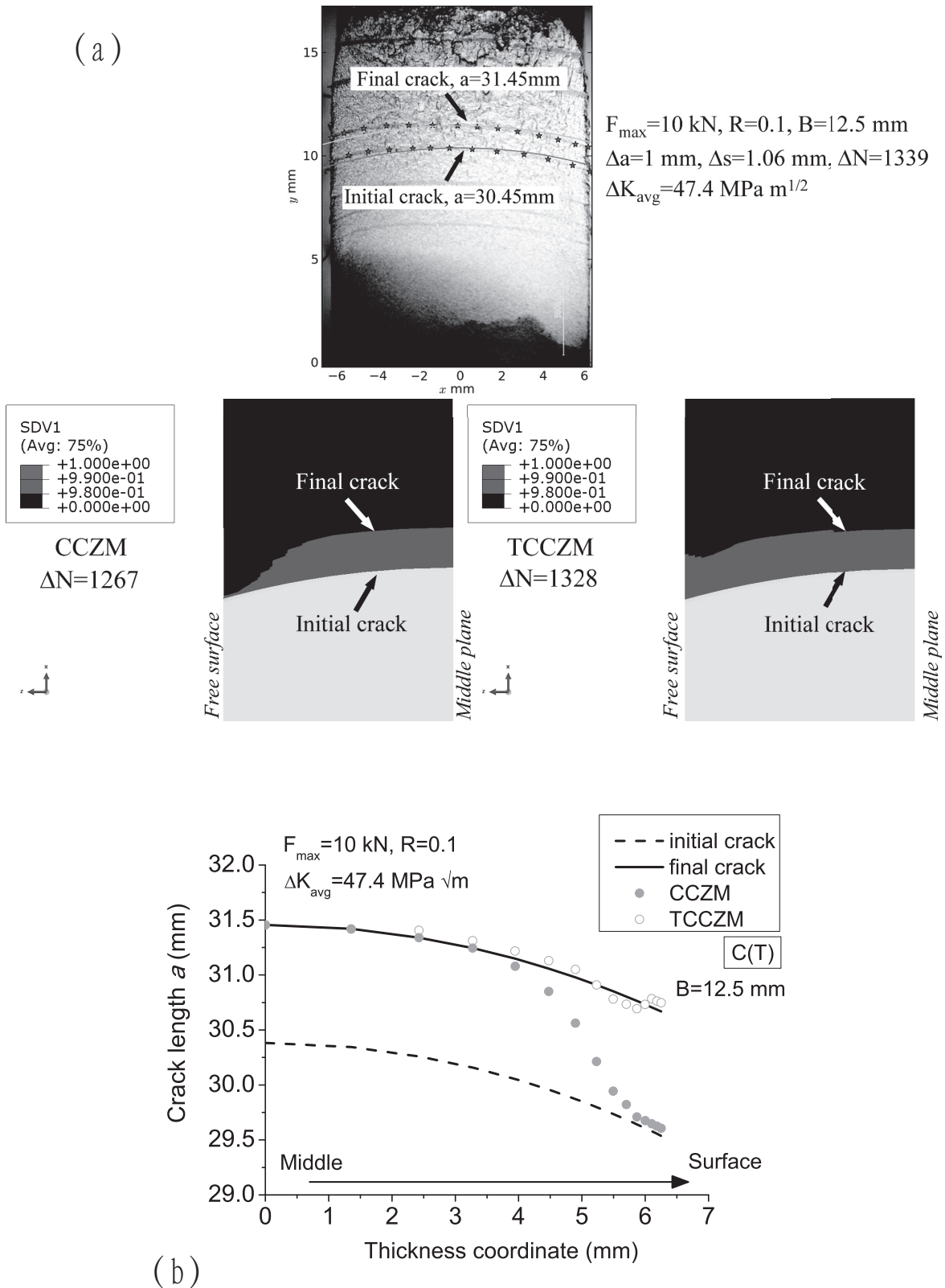


Figure 6.2: Crack profile comparisons of the predictions from both models with the experiment of C(T), with the loading $\Delta K_{\text{avg}} = 47.4\text{ MPa}\sqrt{\text{m}}$.

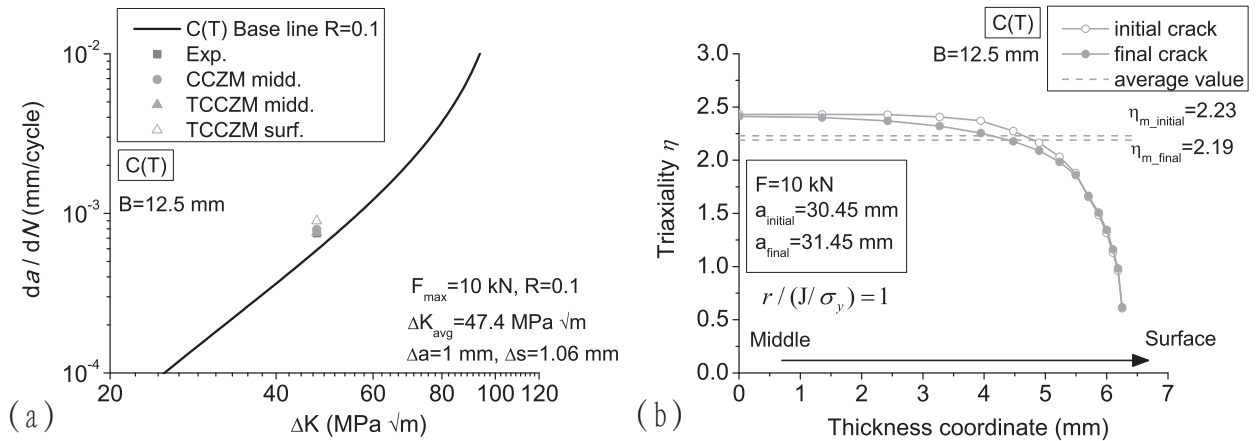


Figure 6.3: (a) Comparisons between the predicted and the experimental fatigue crack growth rate of C(T), with the loading $\Delta K_{avg} = 47.4$ MPa \sqrt{m} . (b) Distributions of η along the initial crack and the final crack from center to surface of C(T) with the loading $F=10$ kN, the middle crack lengths are $a_{ini} = 30.45$ mm and $a_{final} = 31.45$ mm.

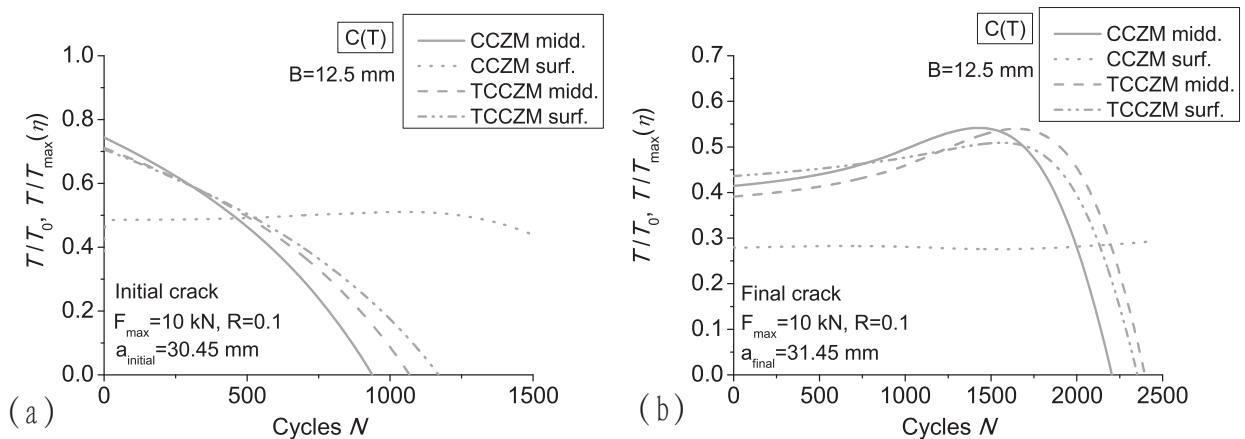


Figure 6.4: With the loading $\Delta K_{avg} = 47.4$ MPa \sqrt{m} , comparisons of the traction evolution of both models. (a) Initial crack; (b) Final crack.

beach marking, therefore the predicted crack growth rate also agrees well with the experimental result, which is identical with the crack growth rate at the middle plane. No crack growth is simulated from CCZM.

The distributions of the stress triaxiality along the initial crack and the final crack with the loading level $F_{\max} = 10$ kN are shown in Fig. 6.3(b). Note that the distributions along both cracks show only slightly differences. For both cracks, the stress triaxiality values keep nearly constant in 55% of the thickness from center to surface. Then the values decrease towards the surface.

• *Traction response*

The numerical results can be further specified by tracing the local response of the material points along the crack growth path. As specified in Chapter 5, the value of $T/T_{\max}(\eta)$ in the damage evolution equation may dominant the cyclic damage accumulation process. For both cracks, the comparisons of the traction evolution at the free surface and the middle plane from both numerical models are illustrated in Fig. 6.4. The local responses of the material points at the initial crack (Fig. 6.4(a)) and the final crack (Fig. 6.4(b)) show similar feature. Significant differences of the computational results from both models are mainly at the free surface.

Due to the dominance of plane stress conditions near the free surface, the local tensile stress near the free surface is lower. For the CCZM, an identical high cohesive strength T_0 are applied at the free surface as well as at the middle plane. Accordingly, at the first loading segment, the value of T/T_0 at the free surface is lower. According to Eq. (6.2), lower T/T_0 would lead to significant small damage increment. Therefore, the damage accumulation at the free surface is much slower in comparing with that at the middle plane. At the final crack, the value of T/T_0 at the free surface is too small to surpass the endurance limit which leads to no damage initiation.

For the TCCZM, due to the lower stress triaxiality at the free surface, the cohesive strength $T_{\max}(\eta)$ applied at the free surface should be also lower according to Eq. (4.8). Consequently, at the first loading segment, the value of $T/T_{\max}(\eta)$ increases which is nearly identical with the value at the middle plane. Then, the material points at the free surface and the middle plane experience similar damage accumulation process. Note that with the different cohesive strengths applied at the free surface and the middle plane, the corresponding failure cycles obtained at the final crack are also close. Therefore, homogeneous crack growth rate is predicted, which shows very close agreement with the experiments.

c. Predictions at high loading level

For the loading level $F_{\max} = 18.75$ kN, the beach markings of the initial crack and the final crack are shown in Fig. 6.5(a). The middle crack extension is $\Delta a = 0.742$ mm and the surface crack extension is $\Delta s = 0.786$ mm. The corresponding average stress intensity range is $\Delta K_{\text{avg}} = 72.36$ MPa $\sqrt{\text{m}}$. The interval cycles obtained from the experiment between the two cracks are $\Delta N^{\text{exp}} = 235$.

• *Numerical results*

Figure 6.5(b) shows detailed final crack profile comparisons of the numerical predictions with the experiment. Numerical results from both models show obvious deviation with

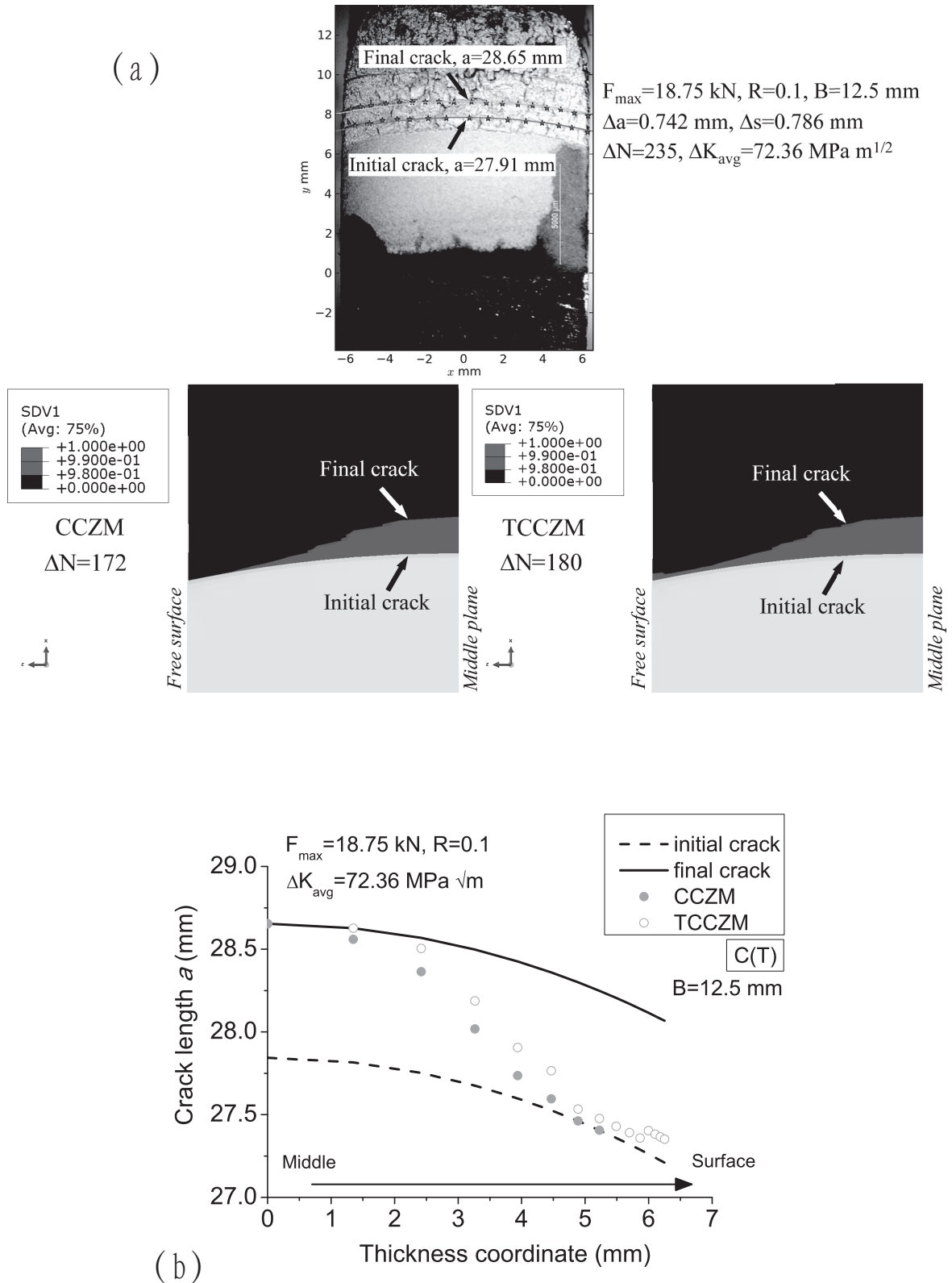


Figure 6.5: Crack profile comparisons of the predictions from both models with the experiment of C(T), with the loading $\Delta K_{\text{avg}} = 72.36$ MPa \sqrt{m} .

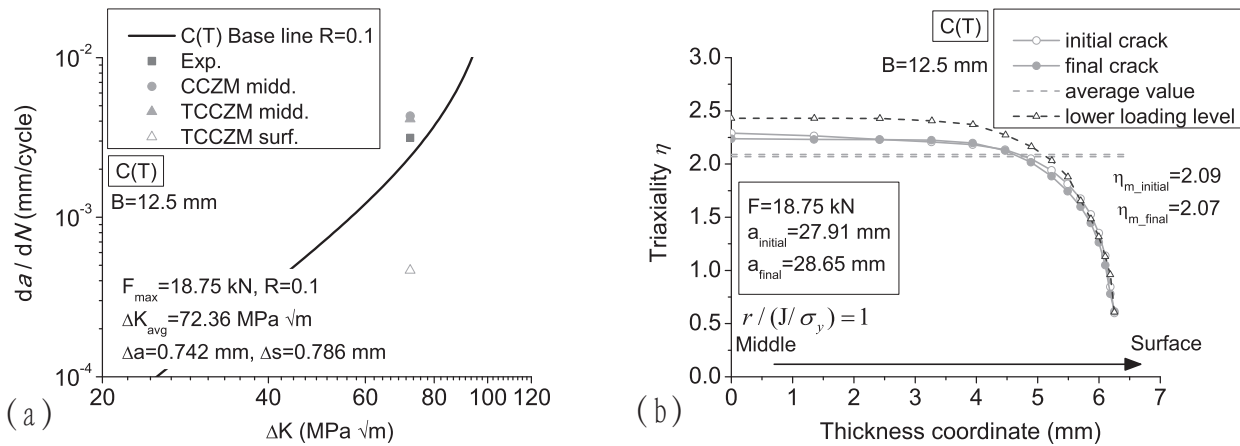


Figure 6.6: (a) Comparisons between the predicted and the experimental fatigue crack growth rate of C(T), with the loading $\Delta K_{avg} = 72.36$ MPa \sqrt{m} . (b) Distributions of η along the initial crack and the final crack from center to surface of C(T) with the loading $F=18.75$ kN, the middle crack lengths are $a_{ini} = 27.91$ mm and $a_{final} = 28.65$ mm.

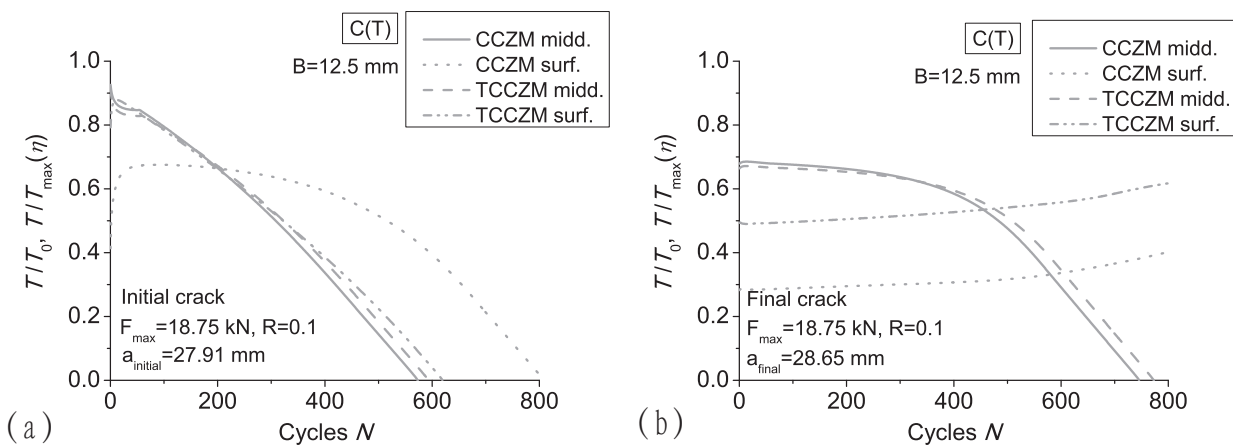


Figure 6.7: With the loading $\Delta K_{avg} = 72.36$ MPa \sqrt{m} , comparisons of the traction evolution of both models. (a) Initial crack; (b) Final crack.

the experiment. Numerical result from CCZM shows agreement with the experiment only in 21% of the thickness from center to surface. No crack extension is predicted in 25% of the thickness near the free surface. Numerical result from TCCZM shows improvable prediction. The agreement of the predicted crack profile with the experiment in 30% of the thickness from center to surface. Although crack extension is predicted from TCCZM at the free surface, the predicted crack length is only $\Delta s^{\text{TCCZM}} = 0.07$ mm. In comparing with the experimental result, the deviation is significant.

Figure. 6.6(a) shows the comparisons of the predicted crack growth rates with the experimental result. Note that at the middle plane, the numerical results from both models agree well with the experiments. However, in contrast to the numerical results of the low loading level, due to a much smaller predicted crack extension from TCCZM at the free surface, the deviation between the prediction and the experimental result is over 7 times.

Figure 6.6(b) shows the distributions of the stress triaxiality along the initial crack and the final crack with the loading level $F_{\text{max}} = 18.75$ kN. Note that due to higher loading level, the plastic deformation is more obvious during fatigue crack propagation. Accordingly, the stress triaxiality value is smaller in comparing with the value obtained at the low loading level. Aside from the average value, the distributions do not show significant differences with different loading levels. The stress triaxiality values keep nearly constant in 55% of the thickness from center to surface, then the values decrease towards the surface. The distributions are reasonable according to the experimental observation in Chapter 3. For the C(T) specimen with $B/W = 0.25$, the curvature of the crack profile is nearly constant during the stable fatigue crack propagation, which denotes that the areas of plane strain conditions are nearly unchanged.

• *Traction response*

The local traction responses of both cracks are shown in Fig. 6.7. For the initial crack, as shown in Fig. 6.7(a), the feature of the traction evolution is the same as that at the low loading level. Numerical results from CCZM show a much slower damage accumulation process at the free surface than that at the middle plane, whereas a homogeneous damage accumulation process of the whole crack is obtained from TCCZM.

For the final crack, however, the damage accumulation process from TCCZM is no more similar at the free surface and the middle plane, as shown in Fig. 6.7(b). At the free surface, although the value of $T/T_{\text{max}}(\eta)$ from TCCZM is higher in comparing with the value of T/T_0 from CCZM, it is still lower than the value at the middle plane. As a result, the damage accumulation process at the free surface is excessive slower, which leads to a significant deviation between the prediction and the experimental data.

It should be noted that due to the high loading level, the effect of plastic deformation is more severe. As discussed in Chapter 3, in this case, the drive force of K_{III} would be the major effect in the area of the dominance of plane stress conditions. Therefore, to describe the damage evolution more precisely, some other aspects, i.e. the damage contributed from the mode III effect, should be also taken into account in the damage evolution equation.

6.3.2 Verification based on surface fatigue crack propagation

The TCCZM will be further verified based on the experiments of surface fatigue crack propagation. The experimental procedures and results have been specified in Chapter 3. In contrast to the fatigue crack propagation of the C(T) specimen, the stress field in a 3D surface crack differs from the conventional plane strain tip field. The stress intensity factor depends additionally on the crack front curvature and may vary non-proportionally with crack growth. Numerical results confirm that the maximum stress intensity is attained at the deepest point for the initial straight-front crack, therefore, the straight-fronted crack tends to become curved. With the crack developed, the maximum stress intensity appears at the surface point so that the crack front curvature becomes smaller.

a. The loading configuration and the FE model

The geometrical dimensions of the rod bar specimen have been shown in Fig. 3.5 and the specimen diameter is $D=12$ mm. With the loading ratio $R = 0.1$, constant force amplitude $F_{\max} = 24$ kN is performed. Present study will only focus on two adjacent crack profiles for each three-dimensional FE model, therefore, the corresponding FE models should be adopted according to different initial crack lengths. The region between the two adjacent cracks is defined as the stress triaxiality effect zone. The method to obtain the corresponding stress triaxiality values within the effect zone has been explained in detail. It has been known that the stress intensity factor along the surface crack front is non-uniform, therefore, the average stress intensity ranges are evaluated at the free surface and the middle plane respectively, defined as $\Delta K_{\text{avg}}^{\text{S}}$ and $\Delta K_{\text{avg}}^{\text{M}}$. The stress intensity factor along the surface crack front is evaluated by the virtual crack closure technique.

The FE configurations for predicting fatigue crack propagation of the rod bar specimen are generated in compliance with the initial crack front. The region near the free surface is partitioned with a thickness of 1.0 mm. Ten layers of elements are used through this region with a bias ratio of 5.0. Ten layers of elements are used through the rest region of the cross section till the middle plane with a same bias ratio. The regular small element length in crack extension direction is 0.01 mm.

b. Predictions at low stress intensity

Figure 6.8(a) shows the beach markings with the middle crack length $a_{\text{ini}} = 5.53$ mm of the initial crack and $a_{\text{final}} = 5.86$ mm of the final crack. Accordingly, the middle crack extension is $\Delta a = 0.33$ mm and the surface crack extension is $\Delta s = 0.48$ mm. The corresponding average stress intensity ranges are $\Delta K_{\text{avg}}^{\text{M}} = 40.6 \text{ MPa}\sqrt{\text{m}}$ and $\Delta K_{\text{avg}}^{\text{S}} = 53.98 \text{ MPa}\sqrt{\text{m}}$. Note that the stress intensity at the free surface is higher. The interval cycles obtained from the experiment between the two cracks are $\Delta N^{\text{exp}} = 750$.

• Numerical results

Figure 6.8(b) shows detailed final crack profile comparisons of the numerical predictions with the experiment. Numerical result from CCZM shows agreement with the experiment in 60% of the thickness from center to surface. Then the predicted crack extension decreases towards the surface. Numerical result from TCCZM shows better agreement, only the crack

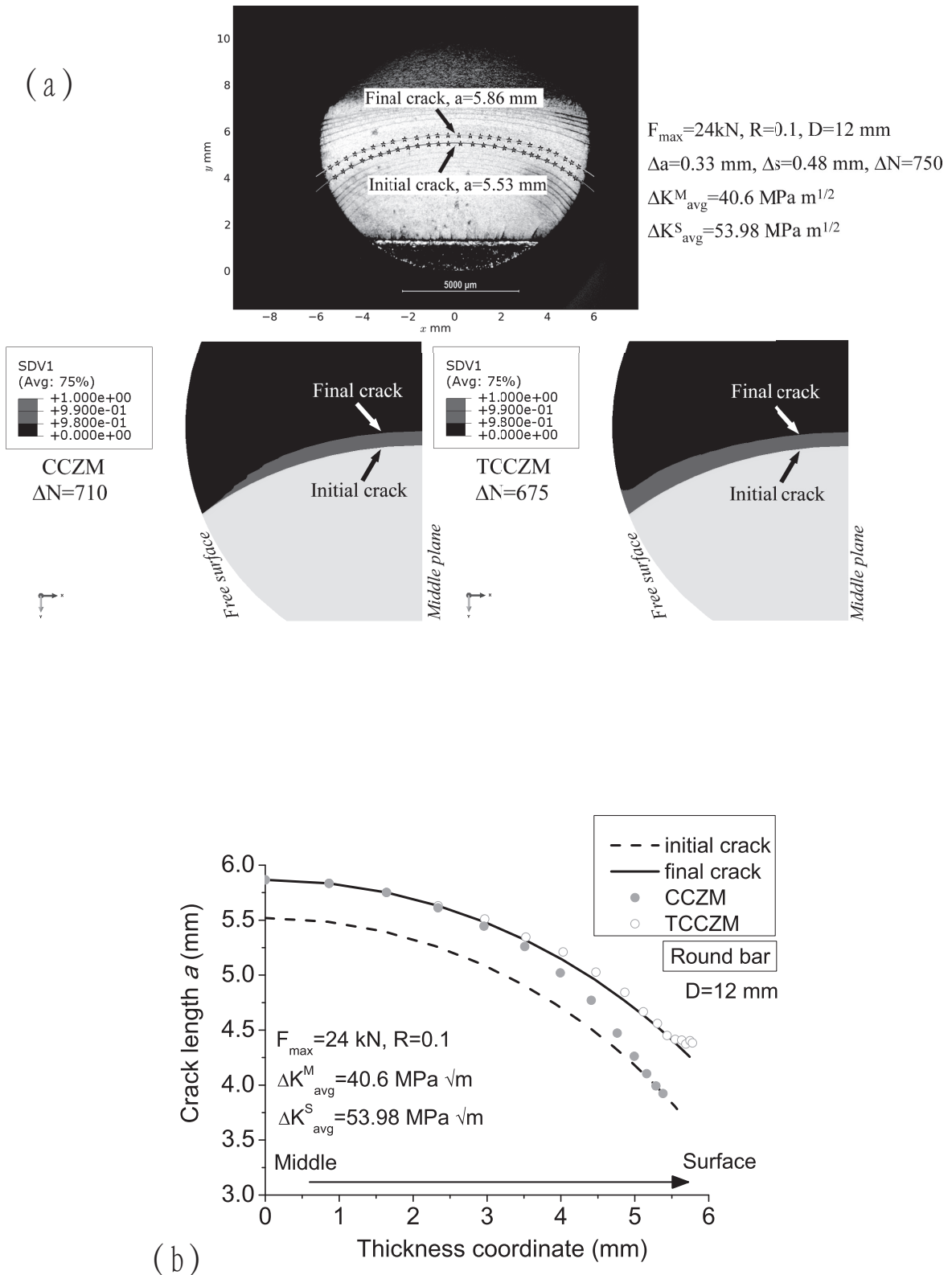


Figure 6.8: Crack profile comparisons of the predictions from both models with the experiment of rod bar, with the loading $\Delta K_{\text{avg}}^M = 40.6 \text{ MPa}\sqrt{\text{m}}$ and $\Delta K_{\text{avg}}^S = 53.98 \text{ MPa}\sqrt{\text{m}}$.

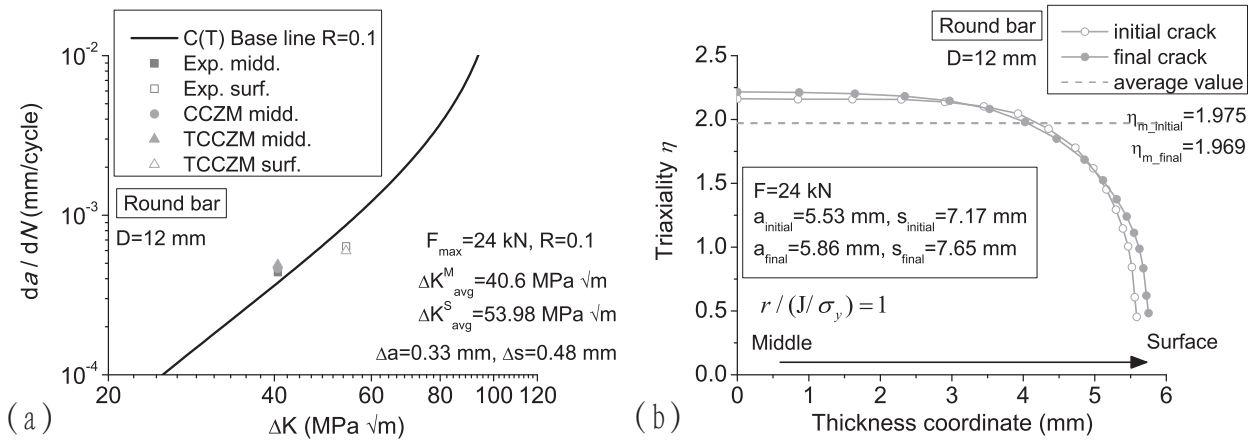


Figure 6.9: (a) Comparisons between the predicted and the experimental fatigue crack growth rate of rod bar, with the loading $\Delta K_{avg}^M = 40.6$ MPa \sqrt{m} . (b) Distributions of η along the initial crack and the final crack from center to surface of rod bar with the loading $F=24$ kN, the middle crack lengths are $a_{ini} = 5.53$ mm and $a_{final} = 5.86$ mm.

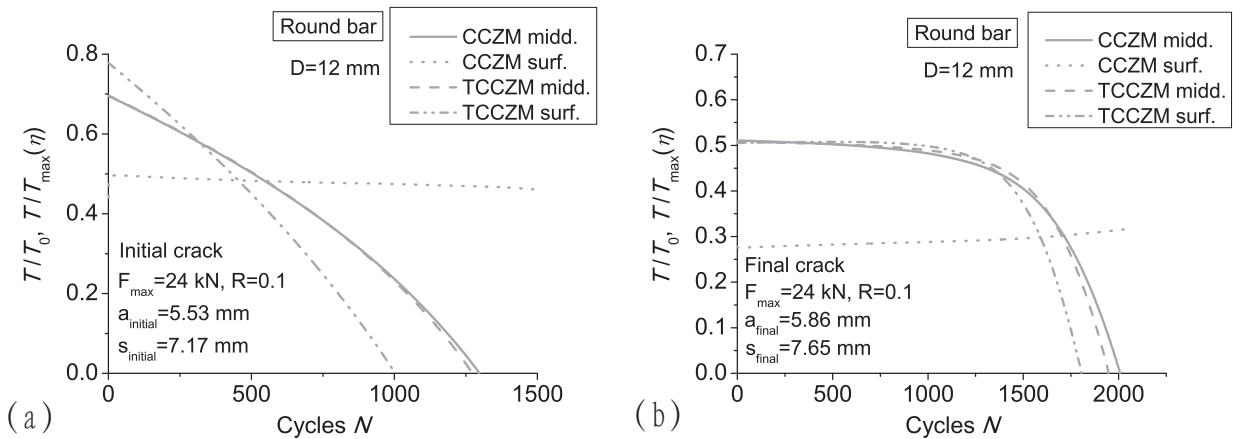


Figure 6.10: With the loading $\Delta K_{avg}^M = 40.6$ MPa \sqrt{m} and $\Delta K_{avg}^S = 53.98$ MPa \sqrt{m} , comparisons of the traction evolution of both models. (a) Initial crack; (b) Final crack.

extension at the free surface is predicted slightly longer. Note that this result should be reasonable due to higher stress intensity at the free surface. More detailed comparisons would be presented by tracing the local traction responses.

The comparisons of the predicted crack growth rates from both numerical models with the experimental results are shown in Fig. 6.9(a). Similar to the results of the low loading level of C(T) specimen, at the middle plane, the predictions from both models show acceptable agreement with the experimental result. At the free surface, no crack extension is predicted from CCZM, whereas the result from TCCZM agrees well with the experiments.

Figure 6.9(b) shows the distributions of the stress triaxiality along both cracks. The stress triaxiality values keep nearly constant in 60% of the thickness from center to surface. Considering the distributions of the C(T) specimen with $B/W = 0.25$, numerical results (Fig. 6.3(b) and Fig. 6.6(b)) confirm a constant stress triaxiality distribution in approximately 55% of the thickness. This implies that with the conditions of the respective geometrical dimensions, at current stress intensity level, the areas of the dominance of plane strain conditions of the rod bar are more or less the same with the areas of the C(T) specimen. Therefore, at current stress intensity level, the crack growth rate at the middle plane of the rod bar can be identified by the conventional C(T) crack growth behavior. Nevertheless, due to the geometrical effect, the crack growth rate at the free surface of the rod bar is below the C(T) crack growth base line.

• *Traction response*

The differences of the local traction responses from both numerical models have been explained in detail in the computations of the C(T) specimen. Note that for the rod bar, higher stress intensity is obtained at the free surface, which leads to a higher $T/T_{\max}(\eta)$ value from TCCZM at the first loading segment of the initial crack. Accordingly, the total failure occurs earlier at the free surface, as shown in Fig. 6.10(a).

For the final crack, as shown in Fig. 6.10(b), due to a redistribution of traction at the subsequent material points, an identical value of $T/T_{\max}(\eta)$ from TCCZM is obtained at the free surface and the middle plane. With the load bearing capacity decreasing, due to higher stress intensity at the free surface, the damage accumulation process is also faster. Note that present computations are terminated when the predicted middle crack extension reaches the final crack position, therefore, the predicted crack extension at the free surface would be slightly longer.

c. Predictions at high stress intensity

With the crack extension, Fig. 6.11(a) shows the beach markings with the middle crack lengths $a_{\text{ini}} = 6.77$ mm of the initial crack and $a_{\text{final}} = 6.94$ mm of the final crack. Between the two cracks, the middle crack extension is $\Delta a = 0.17$ mm and the surface crack extension is $\Delta s = 0.27$ mm. The corresponding average stress intensity ranges are $\Delta K_{\text{avg}}^{\text{M}} = 67.18$ MPa $\sqrt{\text{m}}$ and $\Delta K_{\text{avg}}^{\text{S}} = 80.55$ MPa $\sqrt{\text{m}}$. The interval cycles obtained from the experiment between the two cracks are $\Delta N^{\text{exp}} = 131$.

• *Numerical results*

Similar to the computations of the C(T) specimen with high loading level, due to more obvious effect of the plane stress conditions near the free surface, numerical prediction from

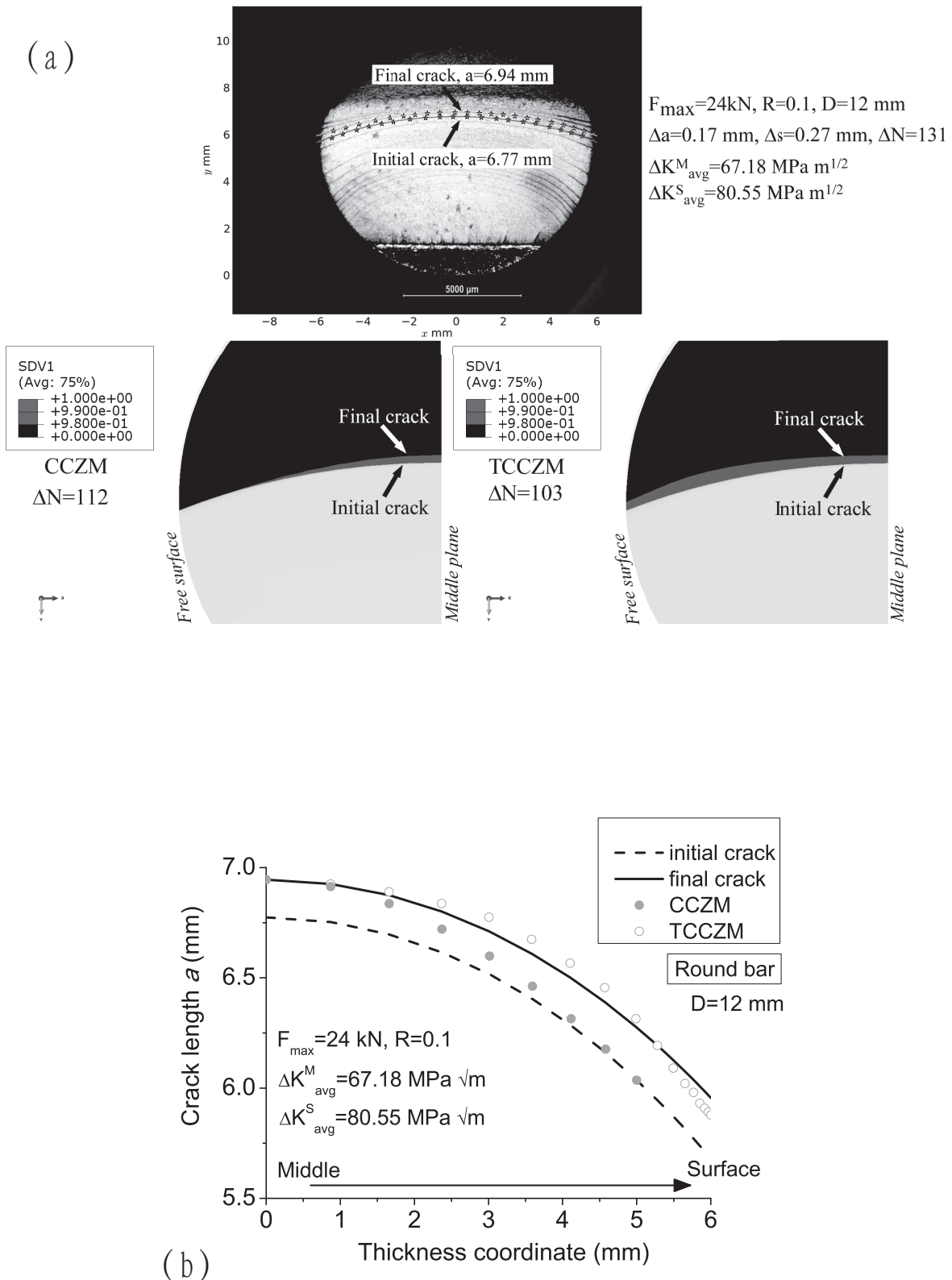


Figure 6.11: Crack profile comparisons of the predictions from both models with the experiment of rod bar, with the loading $\Delta K_{\text{avg}}^M = 67.18 \text{ MPa}\sqrt{\text{m}}$ and $\Delta K_{\text{avg}}^S = 80.55 \text{ MPa}\sqrt{\text{m}}$.

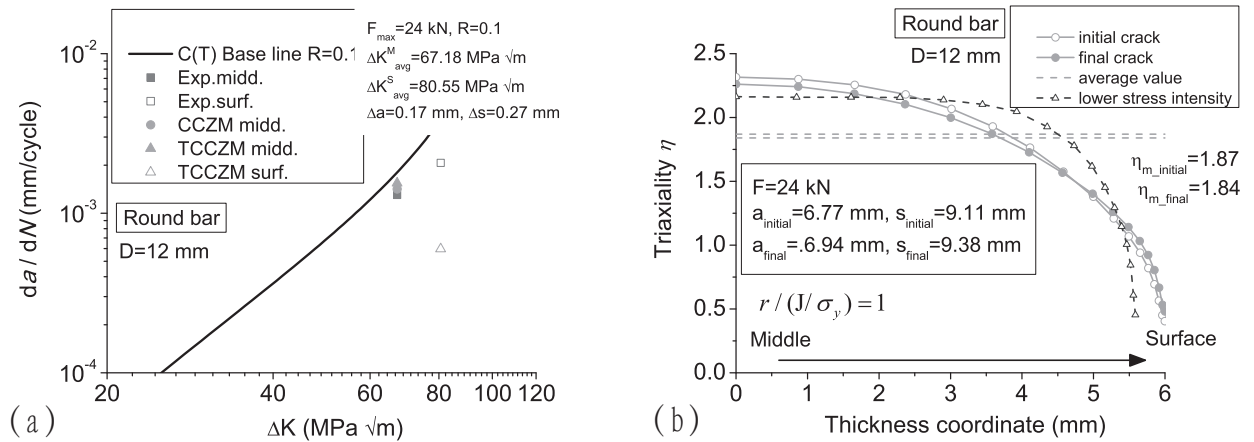


Figure 6.12: (a) Comparisons between the predicted and the experimental fatigue crack growth rate of rod bar, with the loading $\Delta K_{avg}^M = 67.18$ MPa \sqrt{m} . (b) Distributions of η along the initial crack and the final crack from center to surface of rod bar with the loading $F = 24$ kN, the middle crack lengths are $a_{ini} = 6.77$ mm and $a_{final} = 6.94$ mm.

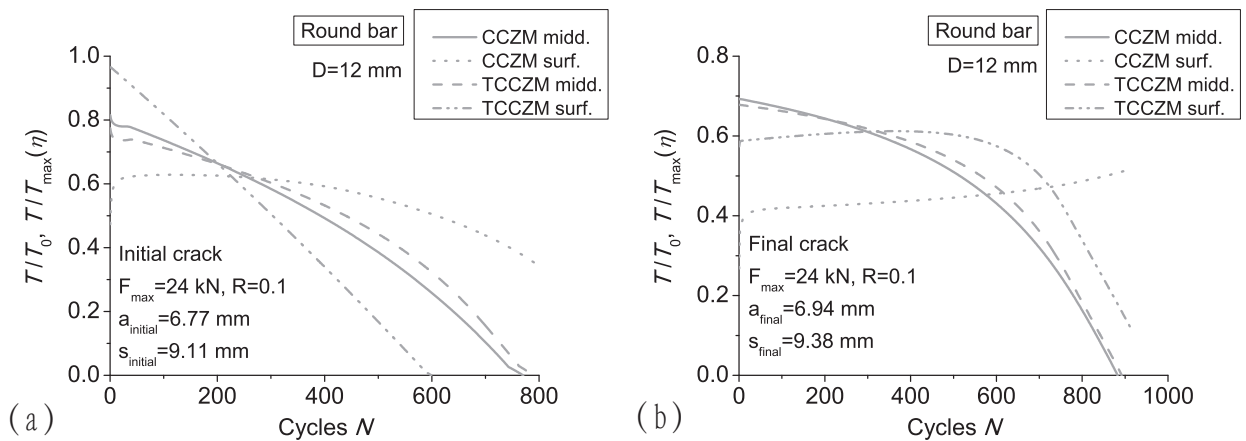


Figure 6.13: With the loading $\Delta K_{avg}^M = 67.18$ MPa \sqrt{m} and $\Delta K_{avg}^S = 80.55$ MPa \sqrt{m} , comparisons of the traction evolution of both models. (a) Initial crack; (b) Final crack.

CCZM shows agreement with the experiment only in 25% of the thickness from center to surface. Furthermore, the predicted crack profile from TCCZM also shows obvious deviation at the free surface, as shown in Fig. 6.11(b). The predicted crack extension is much shorter in comparing with the experimental data. Note that for the initial crack, total failure happens earlier at the free surface due to higher stress intensity, therefore, the predicted crack growth rate would show significant retardation. As shown in Fig. 6.12(a), at the free surface, the deviation between the predicted crack growth rate from TCCZM with the experimental result is over 3.5 times.

Figure 6.12(b) illustrates the distributions of the stress triaxiality along both cracks. Note that with a reduction of the areas of plane strain conditions, the constant stress triaxiality values are only in 27% of the thickness from center to surface. As a result, at current stress intensity level, the fatigue crack growth rates at the free surface and the middle plane of the rod bar are slower in comparing with the conventional C(T) crack growth behavior.

• *Traction response*

The traction responses of the initial crack are shown in Fig. 6.13(a), the feature of the damage accumulation process is the same as that at low stress intensity. However, for the final crack, as shown in Fig. 6.13(b), the value of $T/T_{\max}(\eta)$ from TCCZM of the first loading segment is smaller at the free surface in comparing with the value at the middle plane. As a result, although with higher stress intensity at the free surface, the damage accumulation process is excessive slow.

The main reasons have been discussed in the computations of the C(T) specimen with high loading level. Due to severe influence of the dominance of plane stress conditions, the cyclic damage accumulation contributed by tearing failure is not considered in present damage evolution equation, which retards the damage accumulation.

6.4 Summary

By including the stress-state effect in the proposed cyclic cohesive zone model, a new stress-triaxiality-dependent cyclic cohesive zone model is developed. The cyclic damage evolution accounts for the stress triaxiality explicitly by adopting the stress triaxiality dependent cohesive parameters, $T_{\max}(\eta)$ and $\Gamma_{\max}(\eta)$, which have been identified experimentally. Three-dimensional fatigue crack predictions are performed by applying TCCZM and CCZM in the C(T) specimen and the cracked rod bar. Numerical results including the crack growth rate and the crack profiles are verified with the experimental data.

Numerical predictions substantiate the validation of the stress triaxiality effect on the cyclic loading process. Present model adopts the stress triaxiality dependent cohesive parameters within the effect zone. With the unique set of the cyclic parameters in the damage evolution equation, which have been determined under 2D plane strain condition, three-dimensional computations from both models (CCZM & TCCZM) perform coincident results of the crack growth rate at the middle plane. Generally, no crack growth is predicted at the free surface from CCZM. The predictions of the crack profile from TCCZM at low stress intensity level show excellent agreement with the experiments.

At high stress intensity level, the predicted crack profiles from TCCZM show significant deviation with the experiments at the free surface. In the damage evolution equation, although the value of T/T_{\max} from TCCZM is higher in comparing with the value of T/T_0 from CCZM, it is still too low for the damage accumulation. It has been discussed that due to the obvious plastification, the drive force of K_{III} would be the major effect in the area of the dominance of plane stress conditions. Accordingly, the cyclic damage contributed from mode III effect should be taken into account in the cyclic damage evolution equation. The damage evolution equation requires a further extension to include the failure mechanism of the shear-dominated stress state.

7 Conclusions and outlook

7.1 Conclusions

Fatigue failure is one of the commonest failure modes in engineering. In LCF assessment, the material is locally plastic, especially around cracks. The material plasticity will change the fatigue performance and the fatigue crack growth can no longer be described by the Paris-like models. Cohesive zone modeling provides an alternative way to predict crack growth in ductile materials under elastoplastic loading conditions. Investigations have confirmed that the stress-state plays a crucial role in ductile failure. Integration of the stress triaxiality into the cohesive zone model becomes a necessary step, especially for quantifying the three-dimensional crack. The major goal of the present dissertation is to formulate the stress-triaxiality-dependent cohesive zone model and to predict the three-dimensional fatigue crack propagation.

To quantify the influence of the cohesive law on crack simulation, a special cohesive element has been developed. Numerical results under plane strain condition show that one has to increase the specific cohesive stiffness to diminish the artificial influence of the cohesive law. Additionally, the difference between the cohesive energy and the critical energy release rate vanishes only in an elastic specimen and exceeds 40% for ductile materials.

Experiments reveal that the cohesive parameters are stress triaxiality dependent. Generally, the cohesive strength increases with the stress triaxiality is higher, whereas the cohesive energy decreases. The correlation of $T_{\max}(\eta)$ can be determined by calculating a critical stress-state at the onset of stable crack growth over the whole crack profile. The correlation of $\Gamma(\eta)$ can be estimated according to the tendency of J_i under different stress triaxiality conditions. However, due to the dominance contribution of J_i from plastic dissipation energy at low stress triaxiality condition, the precisely determination of $\Gamma(\eta)$ has to verify the predictions with the experimental results. The stress-triaxiality-dependent cohesive zone model is developed by applying $T_{\max}(\eta)$ and $\Gamma(\eta)$. Numerical results from TCCZM significantly improve the three-dimensional crack growth prediction.

By introducing an overall damage variable which is decomposed into monotonic part and cyclic part, a new CCZM for monotonic and cyclic crack growth is proposed. The material degradation under monotonic loading is represented by softening in the traction-separation law, whereas the cyclic damage is described by an additional damage evolution equation. Detailed finite element computations confirm that the new CCZM is able to describe both rupture and fatigue crack growth properly. The model gives a uniform characterization of Regime II and Regime III in the fatigue crack diagram.

The proposed cyclic cohesive zone model is extended to include the stress-state effect by adopting the correlations of $T_{\max}(\eta)$ and $\Gamma(\eta)$. Numerical predictions substantiate the validation of the stress triaxiality effect on the cyclic loading process. Generally, numerical results of the three-dimensional crack from CCZM do not agree with the experiments. The predictions from TCCZM at low stress intensity level show very well agreement with

the experiments. At high stress intensity level, however, the predictions at the free surface show significant deviation with the experimental results. Experiments have confirmed that due to severe plastification at the high rate of fatigue crack growth, mode III failure would dominate in the area of plane stress conditions. Accordingly, to describe the damage evolution more precisely, extension of the present models should include the shear-dominated stress state, which remains a motivation for the future work.

7.2 Outlook

Throughout the present investigation, the further studies are suggested as following:

- With the consideration of the stress triaxiality effect on CZM, three-dimensional predictions show close agreement with the experiments. However, deviations occur at the free surface when tearing failure is observed, i.e. under monotonic loading condition or cyclic loading with high stress intensity. Several studies of void growth reveal that triaxiality alone is insufficient to characterize important growth and coalescence features. A second measure of stress state, such as the Lode parameter, is required to discriminate between axisymmetric and shear-dominated stress states [101–103]. Extension of the present models and prediction of the crack growth for different cracks in different ductile metals are suggested for the further investigation.
- The assessment of component life includes two aspects: fatigue crack initiation and fatigue crack growth. Present study only focused on the predictions of fatigue crack growth. To verify the application of CCZM in life assessment, further work should be carried out to simulate the fatigue crack initiation and the crack growth with an unique set of damage parameters. Additionally, the life prediction at different stress triaxiality conditions should validate the predictability of TCCZM.
- Present study only considered constant loading ratio with $R = 0.1$. It would be interesting to perform the simulations in different loading ratios. Li and Yuan [124] have discussed a cyclic cohesive model combined with XFEM in 2D plane strain case. The loading ratio effect is included into the damage evolution equation. The further work are recommended to examine the loading ratios effect on three-dimensional computations with TCCZM and to verify the effect with more experimental results.
- The application of CCZM to high cycle fatigue simulation should be developed. In the degradation process of the cohesive zone, the calculation of the damage evolution should use a cycle jump technique to improve the computational cost.
- Present studies have been carried out at room temperature. The fatigue crack growth would be totally different with different temperature conditions. The temperature effect on the fatigue crack growth behavior is an important topic for the further work. Numerical models should be modified by integrating the temperature influence. Additionally, for the case of fatigue crack propagation at high temperature, to predict the crack growth more precisely, i.e. the creep damage, should be also taken into account in the numerical models.

Bibliography

- [1] A.A. Griffith. The phenomena of rupture and flow in solids. *Philosophical Transactions of the Royal Society of London*, 221:163–198, 1921.
- [2] G.R. Irwin. Onset of fast crack propagation in high strength steel and aluminum alloys. *Sagamore Research Conference Proceedings*, 2:289–305, 1956.
- [3] G.R. Irwin. Analysis of stresses and strains near the end of a crack traversing a plate. *Journal of Applied Mechanics*, 24:361–364, 1957.
- [4] G.R. Irwin. Plastic zone near a crack tip and fracture toughness. *Sagamore Research Conference Proceedings*, 4, 1960.
- [5] A.A. Wells. Unstable crack propagation in metals: Cleavage and fast fracture. *Proceedings of the Crack Propagation Symposium*, 1:84, 1961.
- [6] K.H. Schwalbe. Introduction of δ_5 as an operational definition of the CTOD and its practical use. In: Fracture Mechanics: 26th Volume, ASTM STP 1256, pp. 763–778. American Society for Testing and Materials, West Conshohocken, 1995.
- [7] J.R. Rice. A path independent integral and the approximate analysis of strain concentration by notches and cracks. *Journal of Applied Mechanics*, 35:371–386, 1968.
- [8] J.A. Begley and J.D. Landes. *The J integral as a fracture criterion*. In: Fracture Toughness, Proceedings of the 1971 National Symposium on Fracture Mechanics, Part II, ASTM STP 514, pp. 1–20. American Society for Testing and Materials, West Conshohocken, 1972.
- [9] J.W. Hutchinson. Singular behavior at the end of a tensile crack tip in a hardening material. *Journal of the Mechanics and Physics of Solids*, 16:13–31, 1968.
- [10] J.R. Rice and G.F. Rosengren. Plane strain deformation near a crack tip in a power-law hardening material. *Journal of the Mechanics and Physics of Solids*, 16:1–12, 1968.
- [11] C.F. Shih. Relationships between the j-integral and the crack opening displacement for stationary and extending cracks. *Journal of the Mechanics and Physics of Solids*, 29:305–326, 1981.
- [12] H. Kordisch, E. Sommer, and W. Schmitt. The influence of triaxiality on stable crack growth. *Nuclear Engineering and Design*, 112:27–35, 1989.
- [13] V. Tvergaard and J.W. Hutchinson. The relation between crack growth resistance and fracture process parameters in elastic-plastic solids. *Journal of the Mechanics and Physics of Solids*, 40:1377–1397, 1992.

- [14] W. Brocks, D.Z. Sun, and A. Hömig. Verification of the transferability of micromechanical parameters by cell model calculations for viscoplastic materials. *International Journal of Plasticity*, 11:971–989, 1995.
- [15] H. Yuan, G.Y. Lin, and A. Cornec. Quantifications of crack constraint effects in an austenitic steel. *International Journal of Fracture*, 71:273–291, 1995.
- [16] L. Xia and S.F. Shih. Ductile crack growth I: A numerical study using computational cells with microstructurally based length scales. *Journal of Mechanics and Physics Solids*, 43:233–259, 1995.
- [17] L. Xia and S.F. Shih. Ductile crack growth II: Void nucleation and geometry effects on macroscopic fracture behavior. *Journal of Mechanics and Physics Solids*, 43:1953–1981, 1995.
- [18] H. Yuan and W. Brocks. Quantification of constraint effects in elastic-plastic crack front fields. *Journal of Mechanics and Physics Solids*, 46:219–241, 1998.
- [19] C.R. Chen and O. Kolednik. Comparison of cohesive zone parameters and crack tip stress states between two different specimen types. *International Journal of Fracture*, 132:135–152, 2005.
- [20] R. Kiran and K. Khandelwal. A triaxiality and lode parameter dependent ductile fracture criterion. *Engineering Fracture Mechanics*, 128:121–138, 2014.
- [21] K.B. Broberg. Critical review of some methods in nonlinear fracture mechanics. *Engineering Fracture Mechanics*, 50:157–164, 1995.
- [22] N.P. O’Dowd and C.F. Shih. Family of crack-tip fields characterized by a triaxiality parameter-i. structure of fields. *Journal of the Mechanics and Physics of Solids*, 39:898–1015, 1991.
- [23] N.P. O’Dowd and C.F. Shih. Family of crack-tip fields characterized by a triaxiality parameter-ii. fracture applications. *Journal of the Mechanics and Physics of Solids*, 40:939–963, 1992.
- [24] W. Brocks and G. Künecke. Elastic-plastic fracture mechanics analysis of a pressure vessel with an axial outer surface flaw. *Nuclear Engineering and Design*, 119:307–315, 1990.
- [25] P.C. Paris and F. Erdogan. A critical analysis of crack propagation laws. *Journal of Basic Engineering*, 85:528–534, 1963.
- [26] R.G. Forman, V.E. Kearney, and R.M. Engle. Numerical analysis of crack propagation in cyclic-loaded structures. *Journal of Basic Engineering*, 89:459–463, 1967.
- [27] F. Erdogan and M. Ratwani. Fatigue and fracture of cylindrical shells containing a circumferential crack. *International Journal of Fracture Mechanics*, 6:379–392, 1970.
- [28] W. Elber. Fatigue crack closure under cyclic tension. *Engineering Fracture Mechanics*, 2:37–45, 1970.



- [29] W. Elber. *The significant of fatigue crack closure*. In: *Damage tolerance in aircraft structures*. ASTM STP 486. Philadelphia, PA: American Society for Testing and Materials, 1971.
- [30] Jr. Newman. *A crack closure model for predicting fatigue crack growth under aircraft spectrum loading*. ASTM STP 748 American Society for Testing and Materials, Philadelphia, PA, 1981.
- [31] Jr. Newman. *Prediction of fatigue crack growth under variable amplitude and spectrum loading using a crack closure model*. ASTM STP 761. American Society for Testing and Materials, Philadelphia, PA, 1982.
- [32] K.H. Schwable, I. Scheider, and A. Cornec. The SIAM method for applying cohesive models to damage behavior of engineering materials and structures. Technical report, GKSS Technical Report, ISSN 0344-9629, 2009.
- [33] T. Siegmund and W. Brocks. A numerical study on the correlation between the work of separation and the dissipation rate in ductile fracture. *Engineering Fracture Mechanics*, 67:139–154, 2000.
- [34] M. Anvari, I. Scheider, and C. Thaulow. Simulation of dynamic ductile crack growth using strain-rate and triaxiality-dependent cohesive elements. *Engineering Fracture Mechanics*, 73:2210–2228, 2006.
- [35] A.L. Gurson. Continuum theories of ductile rupture by void nucleation and growth: Part I - Yield criteria and flow rules for porous ductile media. *Journal of Engineering Materials and Technology*, 99:2–15, 1977.
- [36] V. Tvergaard and A. Needleman. Analysis of the cup-cone fracture in a round tensile bar. *Acta Metall*, 32:157–169, 1984.
- [37] H.D. Jiang. *Cohesive Zone Model For Carbon Nanotube Adhesive Simulation and Fracture/Fatigue Crack Growth*. PhD thesis, University of Akron, 2010.
- [38] R. de Borst. Numerical aspects of cohesive-zone models. *Engineering Fracture Mechanics*, 70:1743–1757, 2003.
- [39] Y. Xu and H. Yuan. Computational modeling of mixed-mode fatigue crack growth using extended finite element methods. *International Journal of Fracture*, 159:151–165, 2009.
- [40] Y. Xu and H. Yuan. On damage accumulations in the cyclic cohesive zone model for xfem analysis of mixed-mode fatigue crack growth. *Computational Materials Science*, 46:579–585, 2009.
- [41] Y. Xu and H. Yuan. Computational analysis of mixed-mode fatigue crack growth in quasi-brittle materials using extended finite element methods. *Engineering Fracture Mechanics*, 76:165–181, 2009.
- [42] Y. Xu and H. Yuan. Applications of normal stress dominated cohesive zone models for mixed-mode crack simulation based on extended finite element methods. *Engineering Fracture Mechanics*, 78:544–558, 2011.

- [43] D.S. Dugdale. Yielding of steel sheets containing slits. *Journal of the Mechanics and Physics of Solids*, 8:100–104, 1960.
- [44] G.I. Barenblatt. The mathematical theory of equilibrium cracks in brittle fracture. *Advances in Applied Mechanics*, 7:55–129, 1962.
- [45] A. Hillerborg, M. Modeer, and P.E. Petersson. Analysis of crack formation and crack growth in concrete by means of fracture mechanics and finite elements. *Cement and Concrete Research*, 6:773–782, 1976.
- [46] A. Needleman. A continuum model for void nucleation by inclusion debonding. *Journal of Applied Mechanics*, 54:525–531, 1987.
- [47] A. Needleman. An analysis of decohesion along an imperfect interface. *International Journal of Fracture*, 42:21–40, 1990.
- [48] H. Yuan and A. Cornec. *Application of cohesive zone model in investigation of elastic-plastic crack growth*. In: J. Zarka et al., editors. STRUCENG and 288 FEMCAD: structural engineering and optimization. Gournay: IITT International, 1990.
- [49] I. Scheider and W. Brocks. Simulation of cup-cone fracture using the cohesive model. *Engineering Fracture Mechanics*, 70:1943–1962, 2003.
- [50] V.K. Goyal, E.R. Johnson, and C.G. Dávila. Irreversible constitutive law for modeling the delamination process using interfacial surface discontinuities. *Composite Structures*, 65:289–305, 2004.
- [51] H. Krull and H. Yuan. Suggestions to the cohesive traction-separation law from atomistic simulations. *Engineering Fracture Mechanics*, 78:525–533, 2011.
- [52] I. Scheider and W. Brocks. The effect of the traction separation law on the results of cohesive zone crack propagation analyses. *Key Engineering Materials*, 251:313–318, 2003.
- [53] B.G. Vossen, P.J.G. Schreurs, O. van der Sluis, and M.G.D. Geers. On the lack of rotational equilibrium in cohesive zone elements. *Computer Methods in Applied Mechanics and Engineering*, 254:146–153, 2013.
- [54] H. Yuan and X. Li. Effects of the cohesive law on ductile crack propagation simulation by using cohesive zone models. *Engineering Fracture Mechanics*, 126:1–11, 2014.
- [55] J.W. Hutchinson and A.G. Evans. Mechanics of materials: top-down approaches to fracture. *Acta Material*, 48:125–135, 2000.
- [56] M. Elices, G.V. Guinea, J. Gómez, and J. Planas. The cohesive zone model: advantages, limitations and challenges. *Engineering Fracture Mechanics*, 69:137–163, 2002.
- [57] W. Brocks, A. Cornec, and I. Scheider. Computational aspects of nonlinear fracture mechanics. *Comprehensive Structural Integrity: Fracture from Nano to Macro*, pages 127–209, 2003.



- [58] K. Park and G.H. Paulino. Cohesive zone models a critical review of traction-separation relationships across fracture surfaces. *Applied Mechanics Reviews*, 64:060802–1–060802–20, 2011.
- [59] K.H. Schwalbe, I. Scheider, and A. Cornec. *Guidelines for Applying Cohesive Models to the Damage Behaviour of Engineering Materials and Structures*. Springer, Berlin, 2013.
- [60] A. Needleman. Some issues in cohesive surface modeling. *Procedia IUTAM*, 10:221–246, 2014.
- [61] A. Banerjee and R. Manivasagam. Triaxiality dependent cohesive zone model. *Engineering Fracture Mechanics*, 76:1761–1770, 2009.
- [62] H. Yuan, G. Lin, and A. Cornec. Verification of a cohesive zone model for ductile fracture. *Journal of Engineering Materials and Technology*, 118:192–200, 1996.
- [63] A. Ivankovic, K.C. Pandya, and J.G. Williams. Crack growth predictions in polyethylene using measured traction-separation curves. *Engineering Fracture Mechanics*, 71:657–668, 2004.
- [64] G.T. Camacho and M. Ortiz. Computational modelling of impact damage in brittle materials. *International Journal of Solids and Structures*, 33:2899–2938, 1996.
- [65] J.L. Chaboche, R. Girard, and A. Schaff. Numerical analysis of composite systems by using interphase/interface models. *Computational Mechanics*, 20:3–11, 1997.
- [66] G.V. Guinea, M. Elices, and J. Planas. On the initial shape of the softening function of cohesive materials. *International Journal of Fracture*, 87:139–149, 1997.
- [67] X.P. Xu and A. Needleman. Numerical simulation of fast crack growth in brittle solids. *Journal of the Mechanics and Physics of Solids*, 42:1397–1434, 1994.
- [68] G. Lin, A. Cornec, and K.H. Schwable. Three-dimensional finite element simulation of crack extension in aluminium alloy 2024FC. *Fatigue and Fracture of Engineering Materials and Structures*, 21:1159–1173, 1998.
- [69] C.R. Chen, O. Kolednik, I. Scheider, T. Siegmund, A. Tatschl, and F.D. Fischer. On the determination of the cohesive zone parameters for the modeling of micro-ductile crack growth in thick specimens. *International Journal of Fracture*, 120:517–536, 2003.
- [70] D. Gross and T. Seelig. *Fracture Mechanics: With an Introduction to Micromechanics*. SpringerVerlag, Berlin, 2nd edition edition, 2010.
- [71] ABAQUS Version 6.11, Dassault Systemes. *Simulia*, 2011.
- [72] T.R. Chandrupatla and A.D. Belegundu. *Introduction to Finite Elements in Engineering*. Prentice-Hall, 3rd edition edition, 2002.
- [73] W. Brocks and H. Yuan. Numerical investigations on the significance of J for large stable crack growth. *Engineering Fracture Mechanics*, 32:459–468, 1989.

- [74] H. Yuan and W. Brocks. On the J-integral concept for elastic-plastic crack growth. *Nuclear Engineering and Design*, 131:157–173, 1991.
- [75] ASTM Standard. *Standard Test Method for Measurement of Fatigue Crack Growth Rates*, E647-00 edition, 2000.
- [76] R.I. Stephens, A. Fatemi, R.R. Stephens, and H.O. Fuchs. *Metal Fatigue in Engineering*. Wiley-Interscience, 2000.
- [77] ASTM Standard. *Standard Test Method for Linear-Elastic Plane-Strain Fracture Toughness K_{IC} of Metallic Materials*, E399-06 edition, 2006.
- [78] ASTM Standard. *Standard Test Method for Measurement of Fracture Toughness*, E1820-13 edition, 2013.
- [79] J.A. Henkener and R.G. Forman. *Derivation of Crack Growth Properties of Materials for NASA/FLAGRO 2.0*. NASA-Johnson Space Center, 1994.
- [80] H. Li. *Computational and Experimental Investigation of Elastoplastic Cracks under Monotonic and Cyclic loading Conditions*. PhD thesis, Bergische Universität Wuppertal, 2014.
- [81] M. Vormwald. Ermüdungslebensdauer von baustahl unter komplexen beanspruchungsabläufen am beispiel des stahles s460. *Materials Testing*, 53:98–108, 2011.
- [82] A. Carpinteri. Elliptical-arc surface cracks in round bars. *Fatigue of Engineering Materials*, 15:1141–1153, 1992.
- [83] A. Carpinteri and R. Brighenti. Fatigue propagation of surface flaws in round bars: a three-parameter theoretical model. *Fatigue and Fracture of Engineering Materials and Structures*, 19:1471–1480, 1996.
- [84] N. Couroneau and J. Royer. Simplified model for the fatigue growth analysis of surface crack in round bars under mode I. *International Journal of Fatigue*, 20:711–718, 1998.
- [85] C.S. Shin and C.Q. Cai. Experimental and finite element analyses on stress intensity factors of an elliptical surface crack in a circular shaft under tension and bending. *International Journal of Fracture*, 129:239–246, 2004.
- [86] F.P. Yang and Z.B. Kuang. Stress intensity factor for surface fatigue crack in a round bar under cyclic axial loading. *Fatigue and Fracture of Engineering Materials and Structures*, 30:621–628, 2007.
- [87] T.L. Mackay and B.J. Alperin. Stress intensity factor for fatigue cracking in high strength bolts. *Engineering Fracture Mechanics*, 21:391–397, 1985.
- [88] E.F. Rybicki and M.F. Kanninen. A finite element calculation of stress intensity factors by a modified crack closure integral. *Engineering Fracture Mechanics*, 9:931–938, 1977.

- [89] R. Krueger. Virtual crack closure technique: History, approach, and applications. *Applied Mechanics Reviews*, 57:109–143, 2004.
- [90] M. Schöllmann, M. Fulland, and H.A. Richard. Development of a new software for adaptive crack growth simulation in 3D structures. *Engineering Fracture Mechanics*, 70:249–268, 2003.
- [91] J.A. Lemaitre. *A Course on Damage Mechanics*. Springer-Verlag, Berlin, 1996.
- [92] H.A. Richard and K. Benitz. A loading device for the creation of mixed mode in fracture mechanics. *International Journal of Fracture*, 22:55–58, 1983.
- [93] I. Scheider. Derivation of separation laws for cohesive models in the course of ductile fracture. *Engineering Fracture Mechanics*, 76:1450–1459, 2009.
- [94] F.Md. Rashid and A. Banerjee. Implementation and validation of a triaxiality dependent cohesive model: experiments and simulations. *International Journal of Fracture*, 181:227–239, 2013.
- [95] F.Md. Rashid and A. Banerjee. Simulation of fracture in a low ductility aluminum alloy using a triaxiality dependent cohesive model. *Engineering Fracture Mechanics*, 179:1–12, 2017.
- [96] T. Pardoen and J.W. Hutchinson. An extended model for void growth and coalescence. *Journal of the Mechanics and Physics of Solids*, 48:2467–2512, 2000.
- [97] M. Mahler and J. Aktaa. Approach for J-R curve determination based on sub-size specimens using a triaxiality dependent cohesive zone model on a (ferritic-martensitic) steel. *Engineering Fracture Mechanics*, 144:222–237, 2015.
- [98] H. Li, H. Yuan, and X. Li. Assessment of low cycle fatigue crack growth under mixed-mode loading conditions by using a cohesive zone model. *International Journal of Fatigue*, 75:39–50, 2015.
- [99] W. Brocks and J. Olschewski. On J-dominance of crack-tip fields in largely yielded 3D structures. *International Journal of Solids and Structures*, 22:693–708, 1986.
- [100] I. Scheider, M. Rajendran, and A. Banerjee. Comparison of different stress state dependent cohesive zone models applied to thin walled structures. *Engineering Fracture Mechanics*, 78:534–543, 2011.
- [101] Y. Bao and T. Wierzbicki. On fracture locus in the equivalent strain and stress triaxiality space. *International Journal of Mechanical Sciences*, 46:81–98, 2004.
- [102] I. Barsoum and J. Faleskog. Rupture mechanisms in combined tension and shear-experiments. *International Journal of Solids and Structures*, 44:1768–1786, 2007.
- [103] K. Nahshon and J.W. Hutchinson. Modification of the gurson model for shear failure. *European Journal of Mechanics A/Solids*, 27:1–17, 2008.

- [104] A. de Andrés, J.L. Pérez, and M. Ortiz. Elastoplastic finite element analysis of three-dimensional fatigue crack growth in aluminum shafts subjected to axial loading. *International Journal of Solids and Structures*, 36:2231–2258, 1999.
- [105] O. Nguyen, E.A. Repetto, M. Ortiz, and R.A. Radovitzky. A cohesive model of fatigue crack growth. *International Journal of Fracture*, 110:351–369, 2001.
- [106] B. Yang, S. Mall, and K. Ravi-Chandar. A cohesive zone model for fatigue crack growth in quasibrittle materials. *International Journal of Solids and Structures*, 38:3927–3944, 2001.
- [107] S. Maiti and P.H. Geubelle. A cohesive model for fatigue failure of polymers. *Engineering Fracture Mechanics*, 72:691–708, 2005.
- [108] S. Maiti and P.H. Geubelle. Cohesive modeling of fatigue crack retardation in polymers: Crack closure effect. *Engineering Fracture Mechanics*, 73:22–41, 2006.
- [109] J. Eliáš and J.L. Le. Modeling of mode-i fatigue crack growth in quasibrittle structures under cyclic compression. *Engineering Fracture Mechanics*, 96:26–36, 2012.
- [110] S. Serebrinsky and M. Ortiz. A hysteretic cohesive-law model of fatigue-crack nucleation. *Scripta Materialia*, 53:1193–1196, 2005.
- [111] I. Arias, S. Serebrinsky, and M. Ortiz. A phenomenological cohesive model of ferroelectric fatigue. *Acta Materialia*, 54:975–984, 2006.
- [112] K.L. Roe and T. Siegmund. An irreversible cohesive zone model for interface fatigue crack growth simulation. *Engineering Fracture Mechanics*, 70:209–232, 2003.
- [113] T. Siegmund. A numerical study of transient fatigue crack growth by use of an irreversible cohesive zone model. *International Journal of Fatigue*, 26:929–939, 2004.
- [114] B. Wang and T. Siegmund. A numerical analysis of constraint effects in fatigue crack growth by use of an irreversible cohesive zone model. *International Journal of Fracture*, 132:175–196, 2005.
- [115] B. Wang and T. Siegmund. Numerical simulation of constraint effects in fatigue crack growth. *International Journal of Fatigue*, 27:1328–1334, 2005.
- [116] B. Wang and T. Siegmund. Simulation of fatigue crack growth at plastically mismatched bi-material interfaces. *International Journal of Plasticity*, 22:1586–1609, 2006.
- [117] S. Brinckmann and T. Siegmund. Computations of fatigue crack growth with strain gradient plasticity and an irreversible cohesive zone model. *Engineering Fracture Mechanics*, 75:2276–2294, 2008.
- [118] A. Abdul-Baqi, P.J.G. Schreurs, and M.G.D. Geers. Fatigue damage modeling in solder interconnects using a cohesive zone approach. *International Journal of Solids and Structures*, 42:927–942, 2005.



- [119] H. Jiang, X. Gao, and T.S. Srivatsan. Predicting the influence of overload and loading mode on fatigue crack growth: a numerical approach using irreversible cohesive elements. *Finite Elements in Analysis and Design*, 45:675–685, 2006.
- [120] J. Liu, C. Xia, and H. Yuan. Prediction of 3d small fatigue crack propagation in shot-peened specimens. *Computational Materials Science*, 46:566–571, 2009.
- [121] J. Liu, H. Yuan, and R. Liao. Prediction of fatigue crack growth and residual stress relaxations in shot-peened material. *Materials Science and Engineering A*, 527:5962–5968, 2010.
- [122] J. Liu. Numerical analysis for effects of shot peening on fatigue crack growth. *International Journal of Fatigue*, 50:101–108, 2013.
- [123] M. Sander and H.A. Richard. Experimental and numerical investigations on the influence of the loading direction on the fatigue crack growth. *International Journal of Fatigue*, 28:583–591, 2006.
- [124] H. Li and H. Yuan. Cohesive zone modelling of low cycle fatigue cracks in cracked and notched specimens. *Fatigue and Fracture of Engineering Material and Structures*, 00:1–12, 2013.
- [125] J.L. Bouvard, J.L. Chaboche, F. Feyel, and F. Gallerneau. A cohesive zone model for fatigue and creep-fatigue crack growth in single crystal superalloys. *International Journal of Fatigue*, 31:868–879, 2009.
- [126] C. Moriconi, G. Hénaff, and D. Halm. Cohesive zone modeling of fatigue crack propagation assisted by gaseous hydrogen in metals. *International Journal of Fatigue*, 68:56–66, 2014.
- [127] Y. Sun, K. Maciejewski, and H. Ghonem. A damage-based cohesive zone model of intergranular crack growth in a nickel-based superalloy. *International Journal of Damage Mechanics*, 0:1–19, 2012.
- [128] A. Ural, V.R. Krishnan, and K.D. Papoulia. A cohesive zone model for fatigue crack growth allowing for crack retardation. *International Journal of Solids and Structures*, 46:2453–2462, 2009.
- [129] B. Gong, M. Paggi, and A. Carpinteri. A cohesive crack model coupled with damage for interface fatigue problems. *International Journal of Fracture*, 173:91–104, 2012.
- [130] A. Turon, J. Costa, P.P. Camanho, and C.G. Dávila. Simulation of delamination in composites under high-cycle fatigue. *Composites Part A: Applied Science and Manufacturing*, 38:2270–2282, 2007.
- [131] H. Khoramishad, A.D. Crocombe, K.B. Katnam, and I.A. Ashcroft. Predicting fatigue damage in adhesively bonded joints using a cohesive zone model. *International Journal of Fatigue*, 32:1146–1158, 2010.
- [132] H. Khoramishad, A.D. Crocombe, K.B. Katnam, and I.A. Ashcroft. A generalised damage model for constant amplitude fatigue loading of adhesively bonded joints. *International Journal of Adhesion & Adhesives*, 30:513–521, 2010.

- [133] H. Khoramishad, A.D. Crocombe, K.B. Katnam, and I.A. Ashcroft. Fatigue damage modelling of adhesively bonded joints under variable amplitude loading using a cohesive zone model. *Engineering Fracture Mechanics*, 78:3212–3225, 2011.
- [134] D. Morrow. *Biaxial-tension fatigue of Inconel 718*. PhD thesis, University of Illinois at Urbana-Champaign, 1988.
- [135] D. Jha and A. Banerjee. A cohesive model for fatigue failure in complex stress-states. *International Journal of Fatigue*, 36:155–162, 2012.
- [136] X. Cao. *Applying a Cohesive Zone Model in Low Cycle Fatigue*. PhD thesis, Technischen Universität Darmstadt, 2014.



Curriculum Vitae

- 15 Nov. 1985 Born in Jiangsu, P.R. China
- 09/2000 - 07/2003 Senior high school in Xuzhou No.1 middle school, Xuzhou, P.R. China
- 09/2003 - 07/2007 Bachelor of Science in Thermal Energy and Power Engineering, China University of Mining and Technology, Xuzhou, P.R.China
- 10/2007 - 04/2010 Master of Science in Computational Mechanical Engineering, Bergische Universität Wuppertal, Wuppertal, Germany
- 02/2011 - 03/2011 Internship at AVIC Commercial Aircraft Engine Co.,Ltd. (ACAEC), Shanghai, P.R.China
- 06/2010 - 10/2016 PhD, Faculty of Mechanical Engineering, Bergische Universität Wuppertal, Wuppertal, Germany



